



HAL
open science

Measurement of jet spectra reconstructed with charged particles in Pb-Pb collisions at 5.02 TeV with the ALICE detector at the LHC

Hiroki Yokoyama

► **To cite this version:**

Hiroki Yokoyama. Measurement of jet spectra reconstructed with charged particles in Pb-Pb collisions at 5.02 TeV with the ALICE detector at the LHC. High Energy Physics - Experiment [hep-ex]. Université Grenoble Alpes; Université de Tsukuba, 2018. English. NNT : 2018GREAY010 . tel-01835842

HAL Id: tel-01835842

<https://theses.hal.science/tel-01835842>

Submitted on 11 Jul 2018

HAL is a multi-disciplinary open access archive for the deposit and dissemination of scientific research documents, whether they are published or not. The documents may come from teaching and research institutions in France or abroad, or from public or private research centers.

L'archive ouverte pluridisciplinaire **HAL**, est destinée au dépôt et à la diffusion de documents scientifiques de niveau recherche, publiés ou non, émanant des établissements d'enseignement et de recherche français ou étrangers, des laboratoires publics ou privés.



THÈSE

Pour obtenir le grade de

DOCTEUR DE LA COMMUNAUTÉ UNIVERSITÉ GRENOBLE ALPES

**préparée dans le cadre d'une cotutelle entre la
Communauté Université Grenoble Alpes et
l'Université de Tsukuba**

Spécialité : **Physique Subatomique et Astroparticules**

Arrêté ministériel : le 6 janvier 2005 – 25 mai 2016

Présentée par

Hiroki Yokoyama

Thèse dirigée par **Christophe Furget** et **Rachid Guernane**
codirigée par **Tatsuya Chujo** et **Shinichi Esumi**

préparée au sein des **Laboratoire de Physique Subatomique et
de Cosmologie** et **Tomonaga Center for the History of the
Universe**

dans les **École Doctorale de Physique** et **Graduate School of
Pure and Applied Sciences**

Mesure de la production inclusive de jets chargés dans les collisions Pb-Pb à 5.02 TeV avec l'expérience ALICE auprès du LHC

Thèse soutenue publiquement le **29 Mars 2018**,
devant le jury composé de :

Monsieur Tatsuya CHUJO

Maître de conférences, Université de Tsukuba, Membre

Monsieur Shinichi ESUMI

Professeur, Université de Tsukuba, Membre

Monsieur Christophe FURGET

Professeur, Université Grenoble Alpes, Membre

Monsieur Rachid GUERNANE

Chargé de recherche, LPSC, Membre

Monsieur Kazuhiko HARA

Professeur, Université de Tsukuba, Membre

Monsieur Yasuo MIAKE

Professeur, Université de Tsukuba, Président

Monsieur Yves SCHUTZ

Directeur de Recherche, IPHC, Rapporteur

Monsieur Toru SUGITATE

Professeur, Université de Hiroshima, Rapporteur



Measurement of jet spectra reconstructed with charged
particles in Pb-Pb collisions at $\sqrt{s_{\text{NN}}} = 5.02 \text{ TeV}$
with the ALICE detector at the LHC

Hiroki Yokoyama

March, 2018

Measurement of jet spectra reconstructed with charged
particles in Pb-Pb collisions at $\sqrt{s_{\text{NN}}} = 5.02 \text{ TeV}$
with the ALICE detector at the LHC

Hiroki Yokoyama
(Doctoral Program in Physics)

SUBMITTED TO
THE GRADUATE SCHOOL OF PURE AND APPLIED SCIENCES
AT THE UNIVERSITY OF TSUKUBA
AND DOCTORAL SCHOOL OF PHYSICS
AT UNIVERSITÉ DE GRENOBLE
IN PARTIAL FULFILLMENT OF THE REQUIREMENTS
FOR THE DEGREE OF DOCTOR OF PHILOSOPHY IN SCIENCE

Abstract

High-energy nuclear physics aims at revealing the properties of Quark-Gluon Plasma (QGP), a new state of matter consisting of asymptotically free strong-interacting quarks and gluons. According to lattice QCD calculation, a transition from normal nuclear matter to a QGP is expected for energy densities exceeding the critical threshold of $\varepsilon_c \sim 0.18\text{-}0.5 \text{ GeV}/\text{fm}^3$ ($T_c = 154 \pm 9 \text{ MeV}$). Such extreme conditions of temperature and energy density are met in laboratory by smashing heavy nuclei at ultra relativistic energies.

The QGP thus created is however so short lived that it can only be resolved by self-generated hard probes, namely produced together with the medium but on a much shorter time scale. By subsequently interacting with the expanding QGP, these well calibrated probes carry valuable information about its transport properties.

The purpose of this thesis is the measurement of jets as hard probes of the QGP along two complementary directions: by developing a new ALICE jet calorimeter trigger algorithm for LHC Run 2 to efficiently select events containing high energy electromagnetic showers and measuring charged jet production cross sections in Pb-Pb collisions at highest-ever centre of mass energy of 5.02 TeV provided by the LHC.

One of the basic challenges facing jet measurement in heavy-ion collisions consists in separating jets from the soft underlying event. The magnitude of the underlying event is quantified on an event-by-event basis and subtracted from the reconstructed jets. The remaining background fluctuations and detector effects are corrected at the event-ensemble level by an unfolding method. Furthermore, in order to minimise the fake jet contamination, a leading track jet transverse momentum cut-off of $5 \text{ GeV}/c$ is applied.

A strong suppression of jet production in the most central heavy-ion collisions is observed and quantified by the measurement of the nuclear modification factor, R_{AA} . Such a suppression is interpreted as the result of parton energy loss in the QGP, the so-called jet quenching phenomenon. In this thesis, a phenomenological study with an original experimental observable of jet quenching, the parton path length dependence and centre-of-mass

energy dependence of jet energy loss which is extracted from spectrum energy shift, are presented utilising simplified energy loss model.

Contents

Abstract	iii
1 Introduction	3
1.1 The Quark Gluon Plasma	4
1.2 Relativistic Heavy Ion Collisions	5
1.2.1 History of Heavy-Ion Experiments	5
1.2.2 Space-time Evolution in Heavy-Ion Collisions	6
1.2.3 Geometry of Heavy-Ion Collisions	8
1.3 Hard Probes of the QGP	9
1.3.1 Mechanism of Parton Energy Loss in QCD Matter	11
1.3.2 Experimental Results of Jet Quenching	15
1.4 Thesis Motivation	18
2 Experimental Setup	21
2.1 A Large Hadron Collider	21
2.2 The ALICE Experiment	24
2.2.1 V0 detector	25
2.2.2 Inner Tracking System (ITS)	27
2.2.3 Time Projection Chamber (TPC)	28
2.2.4 Electromagnetic Calorimeters (EMCAL, DCAL and PHOS)	30
3 ALICE Calorimeter Trigger Development	35
3.1 Overview of Trigger Generation	35
3.2 L1 Trigger Algorithm	39
3.3 Trigger Performance	42

4	Analysis	47
4.1	Data Samples	47
4.2	Event Selection	48
4.3	Track Selection	49
4.3.1	Tracking Resolution	51
4.3.2	Tracking Efficiency	51
4.4	Jet Reconstruction	52
4.5	Underlying Event	55
4.6	Jet Finding Efficiency	57
4.7	Unfolding	59
4.7.1	Test of Unfolding Performance	62
4.7.2	Unfolded Spectrum	64
5	Systematic Uncertainties	65
5.1	Unfolding	65
5.1.1	p_T Range of the Unfolded Jet Spectrum	65
5.1.2	p_T Range of the Measured Jet Spectrum	65
5.1.3	Unfolding Method	66
5.1.4	Unfolding Regularisation Parameter	66
5.1.5	MC Generator and Prior Selection	67
5.2	Background Fluctuation δp_T Estimation	68
5.3	Correction for the Elliptic Flow Bias	68
5.4	Tracking Efficiency and Resolution	70
5.5	Summary of Systematic Uncertainties	71
6	Results and Discussion	75
6.1	Jet Suppression	75
6.2	Comparison to Charged Hadrons	78
6.3	Comparison to the Jet R_{AA} in Pb-Pb Collisions at $\sqrt{s_{NN}} = 2.76$ TeV	79
6.4	Jet Energy Loss Toy Models	80
6.4.1	Path Length Dependence	84
6.4.2	Centre-of-Mass Energy Dependence	85
7	Summary	87

List of Tables

1.1	Heavy ion facilities. [12]	6
2.1	Summary of LHC runs operated until 2017 [31]. The peak luminosities are measured at ATLAS.	22
2.2	Specification of ALICE electromagnetic calorimeters	32
4.1	Dataset used for the analysis.	47
4.2	The average underlying event density.	56
5.1	Systematic uncertainties for 0-10%	73
5.2	Systematic uncertainties for 30-50%	73
6.1	Geometrical parameters obtained from Glauber model.	77
6.2	Estimated value of spectrum fitting from three jet energy loss models.	82

List of Figures

1.1	Elementary particles of the Standard Model. [3]	4
1.2	The energy density divided by the T^4 , computed on the lattice with different number of flavours. The arrows show the limit for a perfect Bose gas. [2] . .	5
1.3	QCD Phase diagram. Chemical freezeout points are displayed (see section 1.2.2 for definition of chemical freezeout). [13]	7
1.4	Light-cone diagram of longitudinal evolution of the relativistic heavy-ion collisions for with(right) and without(left) QGP cases. [14]	8
1.5	Schematic view of the participant-Spectator model. [15]	9
1.6	Example of hard probes traversing the medium found in high-energy heavy-ion collisions and the corresponding typical properties they can reveal about it. [18]	10
1.7	Jet quenching in central nucleus-nucleus collision. Partons which produced in the initial hard scattering lost energy inside the matter according to its properties (e.g. transport coefficient \hat{q} or gluon density dN^g /dy). [18] . . .	11
1.8	Diagrams for collisional (left) and radiative (right) energy loss of quark with energy E . [18]	12
1.9	Light quark radiative and collisional energy loss for $\sqrt{s_{NN}} = 5.5$ TeV conditions for $L=5$ fm. The thick curves correspond to the running α_s and thin curves to $\alpha_s = 0.5$, utilise the T-dependent Debye mass from the lattice calculations. [26]	14
1.10	Single particle nuclear modification factor R_{AA} for different collision energies up to 2.76 TeV. [27]	15
1.11	(left) Single particle nuclear modification factor R_{AA} (for Pb-Pb collisions at $\sqrt{s_{NN}} = 2.76$ TeV) and R_{pA} (for p-Pb collisions at $\sqrt{s_{NN}} = 5.02$ TeV) of particles at LHC energies. (right) for four particle species. [27]	16

1.12	Nuclear modification factor R_{AA} of $R = 0.2$ jets in 0-10%(left) and 10-30%(right) most central Pb-Pb collisions at $\sqrt{s_{NN}} = 2.76$ TeV, comparing to the calculations from two kind of model (YaJEM and JEWEL). [28]	17
1.13	Nuclear modification factor R_{pA} of charged jets for $R = 0.2$ (left) and $R = 0.4$ (right) in $\sqrt{s_{NN}} = 5.02$ TeV p-Pb collisions. [29]	18
2.1	Schematic of the CERN accelerator complex. [30]	21
2.2	Nucleon-nucleon integrated luminosity delivered to each experiment for all LHC heavy-ion runs to date. [32]	23
2.3	Cut-away view of the ALICE detector. [33]	24
2.4	Position of the two VZERO detectors in the ALICE layout. [44]	26
2.5	The segmentation of V0A and V0C. The two scintillator segments divided by dashed line are read out by the same PMT. [44]	26
2.6	Centrality percentile resolution versus centrality in Pb-Pb collisions at $\sqrt{s_{NN}} = 2.76$ TeV for various ALICE detectors. [44]	26
2.7	Distribution of the sum of amplitudes in V0A and V0C in Pb-Pb collisions at $\sqrt{s_{NN}} = 2.76$ TeV. The red line shows the fit with a Glauber model. [44]	27
2.8	Layout of the ITS which constituted in SPD, SDD and SPD. [45]	28
2.9	Charged particle $1/p_T$ resolution ($= \sigma(p_T)/p_T^2$) as a function of $1/p_T$ for TPC and ITS in p-Pb collisions at $\sqrt{s_{NN}} = 5.02$ TeV. [33]	29
2.10	Schematic view of the TPC field cage. [37]	29
2.11	TPC dE/dx as a function of momentum with superimposed Bethe-Bloch lines for various particle species, measured in Pb-Pb collisions at $\sqrt{s_{NN}} = 5.02$ TeV. [33]	30
2.12	Three calorimeters installed in ALICE at Run2 period: EMCal (upper side), PHOS (bottom side, drawn in orange) and DCal (placed on both side of PHOS in z -direction).	31
2.13	ALICE event display taken in 2015 Pb-Pb run. [33]	33
2.14	Invariant mass spectrum of photon pairs with $p_T = 9-10$ GeV/ c measured in EMCAL in $\sqrt{s_{NN}} = 2.76$ TeV Pb-Pb collisions at centrality 0-20%. [33]	33
2.15	Invariant mass spectrum of photon pairs with $p_T = 4.0-4.2$ GeV/ c measured in PHOS in $\sqrt{s_{NN}} = 2.76$ TeV Pb-Pb collisions at centrality 0-10%. [33]	33
3.1	Summary Trigger Unit board (STU).	36

3.2	Data flow of L1 trigger production in ALICE calorimeters. In total 7 L1-photon triggers (3 for PHOS, 2 for DCAL and 2 for EMCAL) and 4 L1-Jet triggers (2 for DCAL and 2 for EMCAL) are generated.	37
3.3	EMCAL geometry in terms of trigger production. Each TRU charged area contains 96 FastORs.	38
3.4	DCAL+PHOS geometry in terms of trigger production. Each PHOS (DCAL) TRU contains 112 (96) FastORs respectively.	38
3.5	Example of L1-photon patch (= 2×2 FastORs). Amplitudes of these patches are calculated over TRU boundaries.	39
3.6	Example of L1-Jet patches (= 2×2 or 4×4 jet-primitives) in DCAL+PHOS side.	40
3.7	Schematic of event background calculation. Underlying event density estimated by median method are swapped between EMCAL STU and DCAL STU.	41
3.8	Correlation of underlying event densities estimated by DCAL and EMCAL STUs.	42
3.9	Rejection factor of L1-photon triggers given by DCAL and EMCAL in 2015 Pb-Pb run.	43
3.10	Rejection factor of L1-jet triggers given by DCAL and EMCAL in 2015 Pb-Pb run.	43
3.11	(top) p_T spectra of clusters reconstructed in PHOS with minimum bias and PHOS L1-photon triggers at 0-5% Pb-Pb collisions. (bottom) The ratio of them. [33]	44
3.12	(top) p_T spectra of clusters reconstructed in PHOS with minimum bias and PHOS L1-photon triggers at 60-80% Pb-Pb collisions. (bottom) The ratio of them. [33]	44
3.13	EMCAL and DCAL L1-photon trigger efficiency in 2015 Pb-Pb run.	45
3.14	EMCAL and DCAL L1-Jet trigger efficiency in 2015 Pb-Pb run.	45
4.1	Primary vertex position along beam direction. The events with $ v_z < 10\text{cm}$ are selected.	48
4.2	Event centrality distribution calculated with the V0M (= V0A + V0C) estimator.	48

4.3	Correlation between $v_z^{\text{SPD}} - v_z^{\text{PRI}}$ and track multiplicity for four centrality classes. The events with bad vertex reconstruction resolution are rejected.	49
4.4	Track ϕ distributions for two components of hybrid tracks.	50
4.5	Track η distributions for two components of hybrid tracks.	50
4.6	Hybrid track p_T distributions for four centrality classes.	50
4.7	Hybrid track ϕ distributions for three transverse momentum classes.	50
4.8	Transverse momentum resolution ($\sigma(p_T)/p_T$) for two components of hybrid tracks.	51
4.9	Transverse momentum resolution ($\sigma(p_T)/p_T$) for four centrality classes.	51
4.10	Tracking efficiency of hybrid tracks estimated by PYTHIA (pp) and HIJING (Pb-Pb) events, propagated through GEANT simulation.	52
4.11	Ratio of tracking efficiency in Pb-Pb collisions to pp collisions.	52
4.12	(top) Jet p_T distributions after average background subtraction for different p_T^{lead} requirements. (bottom) The ratio to inclusive jet spectrum which shows leading track p_T bias.	53
4.13	Reconstructed jet ϕ distribution with $p_{T,\text{chjet}}^{\text{rec}} > 40 \text{ GeV}/c$	54
4.14	Reconstructed jet η distribution with $p_{T,\text{chjet}}^{\text{rec}} > 40 \text{ GeV}/c$	54
4.15	Correlation between average background density and charged track multiplicity.	55
4.16	Correlation between average background density and event centrality.	55
4.17	δp_T distributions for two RC selections and RC in track randomised event.	57
4.18	The width of δp_T distributions for two RC selections and RC in track randomised event as a function of charged particle multiplicity.	58
4.19	Jet finding efficiency for different p_T^{lead} requirements.	59
4.20	Jet finding efficiency for different event samples; PYTHIA MB and PYTHIA jet-production.	59
4.21	Response Matrix on background fluctuation in 0-10% centrality class.	60
4.22	Response Matrix on detector effects in 0-10% centrality class.	60
4.23	Combined Response Matrix for 0-10% centrality class.	61
4.24	Kinematic efficiency, the jet yield fraction lays inside the selected window of combined response matrix.	61
4.25	Jet momentum resolution for 0-10% centrality class.	61
4.26	Jet momentum resolution for 30-50% centrality class.	61

4.27	p_T distributions used for unfolding performance check; (red) PYTHIA generator-level jets, (blue) PYTHIA reconstruction-level jets, (green) and reconstruction-level spectrum after δp_T smearing.	62
4.28	(top) Unfolded jet spectrum and generator-level jet spectrum. (bottom) The ratio of these spectra.	63
4.29	(top) Refolded jet spectrum and reconstruction-level spectrum after δp_T smearing. (bottom) The ratio of these spectra.	63
4.30	The cross section of charged jet with $R = 0.2$ in Pb-Pb and pp collisions at $\sqrt{s_{NN}} = 5.02$ TeV.	64
5.1	Unfolded spectra for different unfolded jet p_T range selections(top), and their deviations from nominal selection(bottom), in 0-10% centrality class. . . .	66
5.2	Unfolded spectra for different measured jet p_T range selections(top), and their deviations from nominal selection(bottom), in 0-10% centrality class. . . .	66
5.3	Unfolded spectra for different unfolding method selections(top), and their deviation from nominal selection(bottom), in 0-10% centrality class. . . .	67
5.4	Unfolded spectra for different s regularisation parameter selections(top), and their deviations from nominal selection(bottom), in 0-10% centrality class. . . .	67
5.5	Unfolded spectra for different event generator selections(top), and their deviations from nominal selection(bottom), in 0-10% centrality class.	68
5.6	Unfolded spectra for different δp_T definitions(top), and their deviations from nominal value(bottom), in 0-10% centrality class.	69
5.7	The azimuthal dependence with respect to the event leading track of average background density deviation from the nominal (full azimuth) value. . . .	70
5.8	Unfolded spectra for different average background densities due to flow bias(top), and their deviations from nominal value(bottom), in 0-10% centrality class. . . .	70
5.9	Unfolded spectra for different tracking efficiency estimation(top), and their deviations from nominal value(bottom), in 0-10% centrality class.	71
5.10	Unfolded spectra for different track momentum resolution(top), and their deviations from nominal value(bottom), in 0-10% centrality class.	71
6.1	Charged jet spectra in Pb-Pb collisions after the normalisation by the number of binary collisions. As a pp reference, the spectrum measured with $\sqrt{s} = 5.02$ TeV pp run and corresponding simulation result are shown.	76

6.2	Charged jet nuclear modification factors of $R = 0.2$ in Pb-Pb collisions at $\sqrt{s_{\text{NN}}} = 5.02$ TeV.	77
6.3	Comparison of nuclear modification factor between charged particles at $\sqrt{s_{\text{NN}}} = 2.76$ TeV and charged jets at $\sqrt{s_{\text{NN}}} = 5.02$ TeV.	78
6.4	Comparison of charged jet nuclear modification factor between $\sqrt{s_{\text{NN}}} = 2.76$ TeV and $\sqrt{s_{\text{NN}}} = 5.02$ TeV.	79
6.5	Comparison of nuclear modification factor of jets with $R = 0.4$ measured by ATLAS between $\sqrt{s_{\text{NN}}} = 2.76$ TeV and $\sqrt{s_{\text{NN}}} = 5.02$ TeV. [58]	80
6.6	(top) PYTHIA Charged jet spectrum given by PYTHIA. The black line is Tsallis fitting result. (bottom) The ratio of data to fitting function.	81
6.7	Comparison of spectrum fitting from three energy loss models, in 0-10% centrality class.	82
6.8	Comparison of charged jet nuclear modification with constant energy loss model (black line).	83
6.9	Comparison of charged jet nuclear modification with fractional energy loss model (black line).	83
6.10	Comparison of charged jet nuclear modification with jet disappearance model (black line).	84
6.11	The sketch of heavy-ion collision in transverse plane. The average parton path length and overlapped area are estimated by toy model calculation.	85
6.12	The estimated average parton path length as a function of collision impact parameter b	85
6.13	Average energy loss of charged jets as a function of estimated parton path length, with fitting result by linear function.	86
6.14	Average energy loss of charged jets as a function of estimated parton path length, with fitting result by quadratic function.	86
6.15	Average energy loss as a function of charged multiplicity per unit transverse area in 0-10% centrality class for three centre-of-mass energies.	86

Acknowledgments

First of all, I would like to express deepest gratitude to Tatsuya Chujo and Rachid Guernane, for their continuous supports not only on research but also daily life (e.g. proposing the opportunities of presentation, thinking about the funding, starting up and organising new helpful meeting for the study and so on). Ritsuya Hosokawa also has given a lot of honest opinions as co-worker through the whole studies. Without their help, no doubt that my research could not never been achieved at all.

I would like to thank Yasuo Miake, Christophe Furget, Yves Schutz, Shinichi Esumi. They give some ideas, comments and suggestions about the research with a clear perspective. Their comments sometimes brought out my motivation a lots.

On the calorimeter trigger development and commisioning, I'm grateful for the members of ALICE-EMCAL and ALICE-PHOS groups, in particular, Olivier Raymond Bourrion, Jiro Fujita, Yuri Kharlov, Jiri Kral, Martin Poghosyan, Daiki Sekihata, and Jussi Viinikainen. They kindly instructed the know-how on the detector operation and assisted my trigger commissioning work.

On the jet measurement, I express my gratitude to AAF (ALICE Asian France Collaboration) members, Oliver Busch, Tatsuya Chujo, Rachid Guernane, Yaxian Mao, Hua Pei, Hadi Hassan, Ritsuya Hosokawa and Byungchul Kim. Thanks to their steady advises and assistances on the analysis, the research was able to proceed smoothly.

Many thanks to the colleagues who spent times together during the stay at CERN, Hikari Murakami, Tsubasa Okubo, Yuko Sekiguchi, Daiki Sekihata, Kohei Terasaki, Satoshi Yano and Daisuke Watanabe, for their friendship and meaningful discussions. I also thank Shingo Sakai, Yosuke Watanabe and all members of Tsukuba and Grenoble groups for their encouraging, discussing and advices.

I could never restarted the academic life and continued the research without the understanding and encouragement to my way of life from my parents, sister and an old friend. Finally I wish to express sincere appreciation to them.

Chapter 1 Introduction

Particle physics aims at understanding the fundamental constituents of nature and their interactions. At the present time, the constituents are classified into three categories: hadrons, leptons and gauge bosons. Hadrons are objects which are subject to strong and weak interaction, while leptons interplay through weak interaction. When these particles carry electro-magnetic charge, they are also affected by the electro-magnetic interaction. The gauge bosons behave as a mediator of these forces.

There are in total twelve types of particles in the lepton family: electron, muon, tau, the respective neutrinos, and their anti-particles. Conversely, a large number of hadron species have been found, which can be classified into two types: mesons which are made up of quark and anti-quark pairs, and baryons which consist of three (anti-)quarks. There are twelve types of particles in the quark family: up, charm, top (with electric charge $2/3$), down, strange, bottom (with electric charge $-1/3$) and their anti-particles.

The Standard Model (SM) describes the interaction among these elementary particles, including strong, weak and electro-magnetic interactions [1, 2]. Each interaction has its own mediator, gluons for strong interactions, Z^0 and W^\pm bosons for weak interactions and the photon for electro-magnetic interactions. The main difference between electro-magnetic and weak interaction is the range of the interaction which is related to the mass of the its mediators: photon (mass-less), Z^0 and W^\pm bosons ($91 \text{ GeV}/c^2$ and $80 \text{ GeV}/c^2$ respectively). Due to the large masses of Z^0 and W^\pm , the range of the weak interaction is limited, while long-range electro-magnetic interaction is allowed. All elementary particles of the SM are summarised in Fig. 1.1.

Quantum Chromodynamics (QCD), the theory of strong interaction, deals with the interactions between quarks and gluons [4]. QCD has two particular features: the quark confinement inside hadrons ($\sim 1 \text{ fm}$) and the asymptotic freedom at large momentum transfer scale on short distance [5, 6, 7]. Due to asymptotic freedom, at high temperature, quarks and gluons become weakly coupled, freed from nucleons, forming a new state of matter called the Quark-Gluon Plasma (QGP) [8].

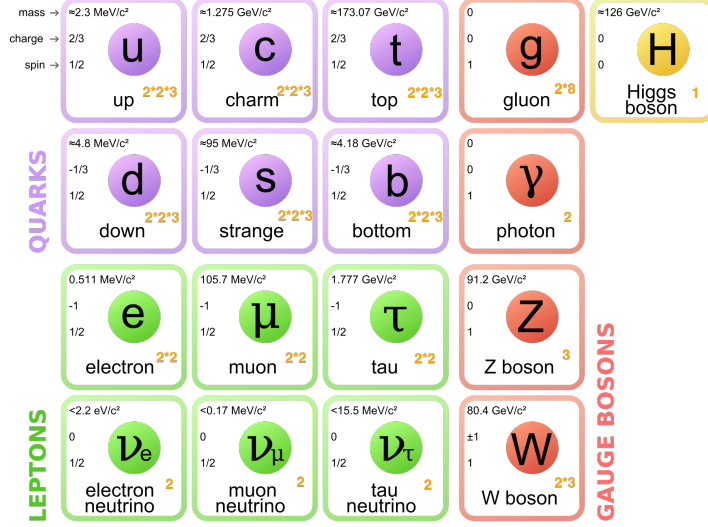


Fig 1.1: Elementary particles of the Standard Model. [3]

1.1 The Quark Gluon Plasma

High-energy heavy-ion physics intends to study the QGP phase of QCD at finite temperature. Lattice QCD calculations predict that a phase transition from normal nuclear matter to a QGP should occur when energy density exceeds the critical threshold of $\varepsilon_c \sim 0.18\text{--}0.5 \text{ GeV}/\text{fm}^3$ ($T_c = 154 \pm 9 \text{ MeV}$) [9, 10, 11]. Experimentally, by colliding two heavy nuclei at ultra-relativistic energies, one expects to form a hot and dense deconfined medium and study its collective (colour) dynamics.

According to QCD, the potential between a $q\bar{q}$ pair is phenomenologically given by,

$$V_{q\bar{q}} = -\frac{a(r)}{r} + Kr \quad (1.1)$$

where r is the distance between the two quarks, $a(r) \propto 1/\ln(1/r)$, and K is the string tension of the quark and anti-quark pair. The first term of Eq. 1.1 is the colour Coulomb potential and the second term is the linear confining potential which is a characteristic feature of QCD. The equation encodes quark confinement: the inter-quark potential increases linearly with the distance.

On the one hand, the energy needed to separate the two quarks grows with the distance between them. At large distance, the linear term dominates and when the potential energy

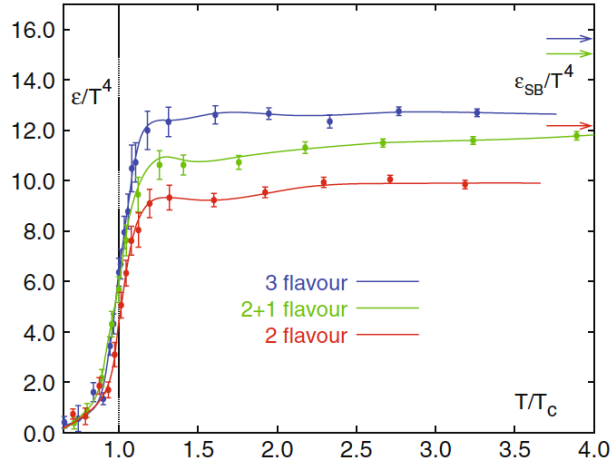


Fig 1.2: The energy density divided by the T^4 , computed on the lattice with different number of flavours. The arrows show the limit for a perfect Bose gas. [2]

is greater than twice the quarks, a new $q\bar{q}$ pair is created. Therefore, deconfined single quarks cannot be observed which is known as “quark confinement”. On the other hand, Lattice QCD calculations predict that quarks and gluons are deconfined at high energy density or temperature.

Based on Lattice QCD calculations, Fig. 1.2 shows that the energy density divided by T^4 undergo a rapid crossover around the critical temperature, T_c , accompanied by an increase of the effective number of active degrees of freedom, i.e. deconfinement, and reaches a plateau of only $\sim 70\%$ of the ideal limit of a Stefan-Boltzmann (SB) gas of light quarks and gluons. Not reaching the SB limit indicates that the QGP is weakly coupled with persisting non perturbative effects.

1.2 Relativistic Heavy Ion Collisions

1.2.1 History of Heavy-Ion Experiments

The QCD phase diagram can be explored in the laboratory with high-energy nuclear collisions. The pioneering advances in relativistic heavy-ion physics were achieved at fixed-target accelerators, starting in the early 1970’s at the Bevalac (Berkeley), followed by the AGS (BNL) and SPS (CERN). The highest centre-of-mass energy per nucleon achieved in these experiments was $\sqrt{s_{NN}} = 17 \text{ GeV}$.

Machine	Location	Ion beam	Maximum $\sqrt{s_{NN}}$	Start of experiment
Bevalac	LBNL, Berkeley	up to U	2 GeV	1974
AGS	BNL, Brookhaven	up to ^{197}Au	5 GeV	1986
SPS	CERN, Geneva	$^{16}\text{O}, ^{32}\text{S}, ^{208}\text{Pb}$	17 GeV	1986
RHIC	BNL, Brookhaven	$^{197}\text{Au}, ^{64}\text{Cu}$	200 GeV	2000-present
LHC	CERN, Geneva	^{208}Pb	5.02 TeV	2009-present

Tab 1.1: Heavy ion facilities. [12]

Later on, benefiting from the technological breakthrough of new colliding beam accelerators, far higher centre-of-mass energy per nucleon could be reached. At the turn of the century, the Relativistic Heavy Ion Collider (RHIC, BNL) starts to deliver Au+Au collisions up to $\sqrt{s_{NN}} = 200 \text{ GeV}$, and lately the Large Hadron Collider (LHC, CERN) is capable to accelerate Pb beams up to $\sqrt{s_{NN}} = 5.02 \text{ TeV}$. The main features of these accelerators are listed in Tab. 1.1. Fig. 1.3 summarises QCD phase diagram exploration at various accelerators.

The increase in the centre-of-mass energy of the colliding system enables to significantly enlarge the volume, lifetime and energy density of the formed medium, offering unprecedented conditions for precision measurements of the QGP parameters (i.e. viscosity, transport coefficients and so on).

1.2.2 Space-time Evolution in Heavy-Ion Collisions

A simplistic view of the system evolution could be described as a chronological sequence of events starting from the overlapping nuclei initial time τ : (see light-cone diagram of longitudinal evolution of the relativistic heavy-ion collisions in Fig. 1.4).

1. Until interaction ($\tau < 0$)

Before collision, the incoming nuclei are accelerated up to a velocity close to the speed of light. The Lorentz contracted nuclei thus have a pancake shape ($\sim 1 \text{ fm}$ thickness).

2. Nuclear overlap and Pre-equilibrium ($0 < \tau < \tau_0$)

After collision, the system undergoes a pre-equilibrium phase with multiple partonic

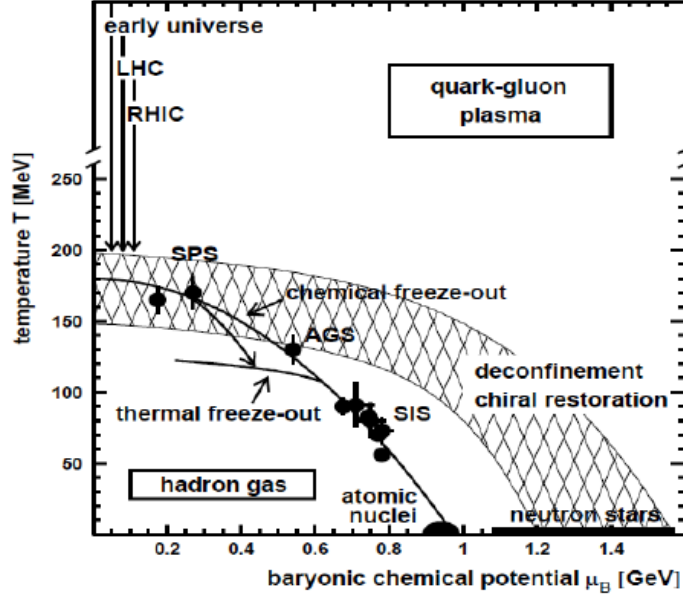


Fig 1.3: QCD Phase diagram. Chemical freezeout points are displayed (see section 1.2.2 for definition of chemical freezeout). [13]

scatterings driving towards the formation of a thermalised partonic medium. During the early pre-equilibrium phase, hard partons (jets and heavy flavours) are produced via large momentum transfer scatterings. The time until thermalisation, τ_0 is less than $1 \text{ fm}/c$.

3. Hydrodynamic evolution ($\tau_0 < \tau < \tau_f$)

When thermalisation is realised, the equilibrated partonic medium reaches a high temperature and energy density. The QGP is produced: the quarks and gluons inside the medium show collective behaviour, freed from confinement. Subsequently, the expanding system begins to cool down.

4. Freezeout ($\tau_f < \tau$)

The QGP keeps expanding and cooling down until hadronisation occurs at τ_f with subsequent “chemical freezeout”(particle species fixing) and “kinetic freezeout”(particle momentum fixing).

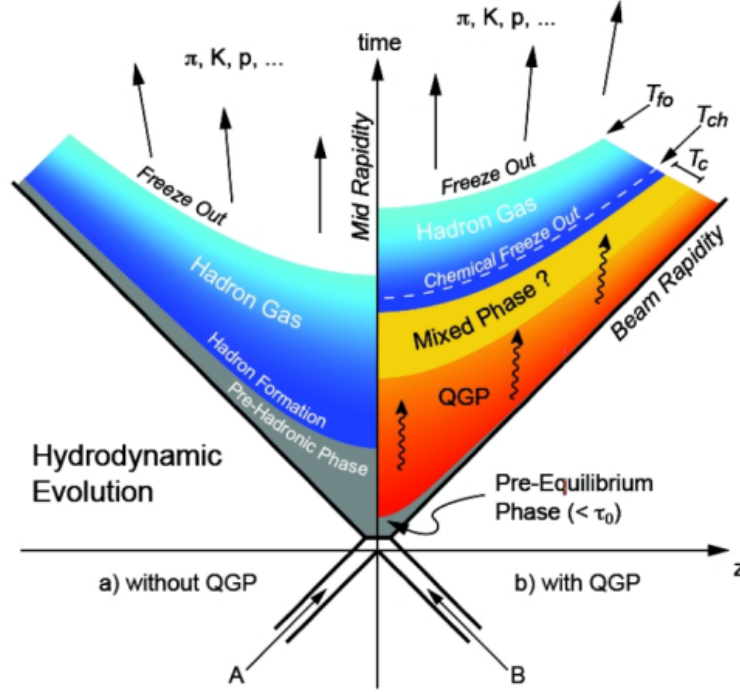


Fig 1.4: Light-cone diagram of longitudinal evolution of the relativistic heavy-ion collisions for with(right) and without(left) QGP cases. [14]

Different global observables convey information about these different stages. Jets, which measurement is the purpose of this work, are hard probes produced at very early stages of the collision and thus potentially carry information about the whole system evolution (see section 1.3).

1.2.3 Geometry of Heavy-Ion Collisions

In relativistic heavy-ion collisions, the collision geometry can be defined within the participant-spectator model [16, 17]. Fig. 1.5 shows a schematic view of a collision between nuclei. The impact parameter b , defined as the distance between the centre of nuclei, characterises the centrality of collision (for an experimental determination, see section 2.2.1). The nucleons taking part in the primary collisions are called “participants” while remainders are called “spectators”.

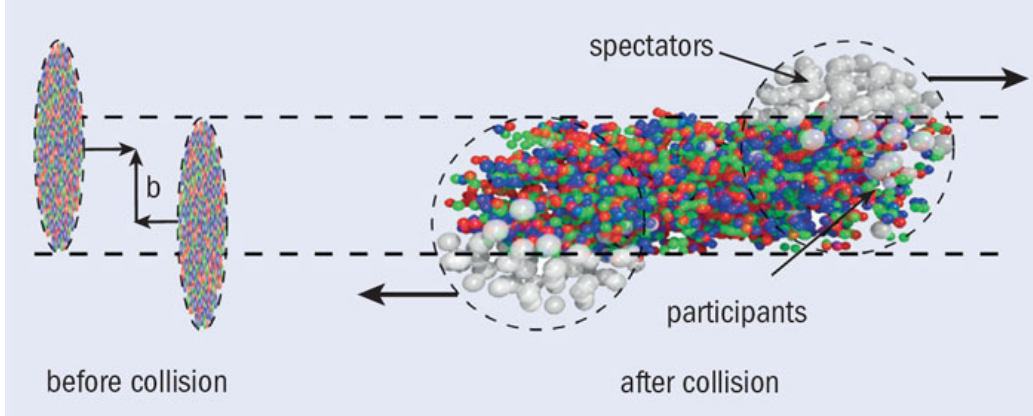


Fig 1.5: Schematic view of the participant-Spectator model. [15]

The spectators keep their longitudinal velocity and mostly travel along the beams direction, while the secondary particles emitted from participant interactions are mostly observed around mid-rapidity. Once the impact parameter of the collision is determined, the Glauber Model provides the number of participant nucleons (N_{part}) and number of nucleon-nucleon collisions (N_{coll}) for a given impact parameter. These quantities can be calculated (analytically or numerically) under the following assumptions:

- Collisions of two nuclei are expressed in terms of the individual interactions of the constituent nucleons.
- At high energies, nucleons travel on straight line trajectories and are essentially undeflected.

1.3 Hard Probes of the QGP

Anyone who intends to characterise the QCD matter in laboratory will inevitably confront the challenge of its short lifetime ($\sim 10 \text{ fm}/c$) and tiny size ($\lesssim 20 \text{ fm}$). One must then simply rule out the usage of external probes to fall back in “self-generated” probes. Among which high- p_{T} QCD processes, the so-called “hard probes”, have demonstrated excellent proficiency. Such hard probes, especially partons with large transverse momentum

1. are produced by parton scatterings with large momentum transfer (Q^2), hence, are linked with QCD degrees of freedom,

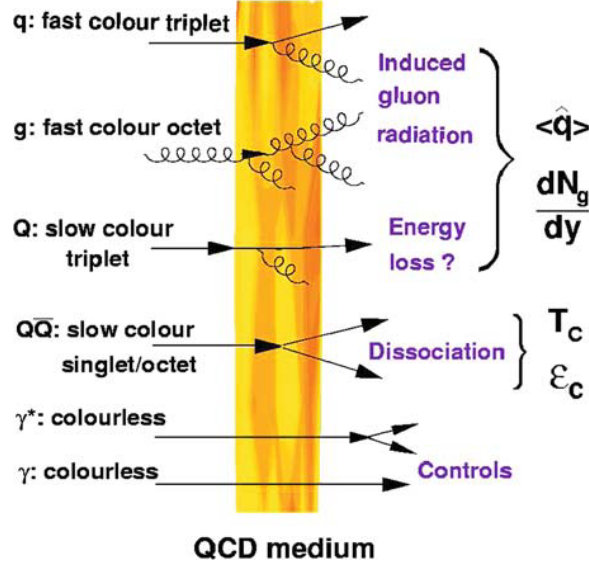


Fig 1.6: Example of hard probes traversing the medium found in high-energy heavy-ion collisions and the corresponding typical properties they can reveal about it. [18]

2. are generated at very early stage of the collision, $\tau \approx 1/p_T \leq 0.1\text{fm}/c$, and are therefore affected by entire medium evolution,
3. and have measured production cross sections and/or precise estimation within perturbative QCD (pQCD).

Jets are a flagship hard probe in nuclear collisions (c.f. Fig. 1.6). An elastic or inelastic scattering of two partons from incoming nucleus produces two or more partons in the final state. The two outgoing partons carry a large virtuality Q which decreases by subsequent gluon-radiations and/or splittings into quark-antiquark pairs. The QCD radiation probabilities given by the DGLAP equations [19] conduct parton branching growth. At this stage, the generated partons fragment into a lot of final-state hadrons non-perturbatively. In general these hadrons are observed as a collimated spray of hadrons directed close to initial parton, called as “jet”.

One of the most remarkable signatures of QGP formation observed both at RHIC [20] and LHC [21] is “jet quenching”: the attenuation of the jet yields in heavy-ion collisions compared to pp (corrected for geometry) or disappearance of back-to-back jets. Jet quenching

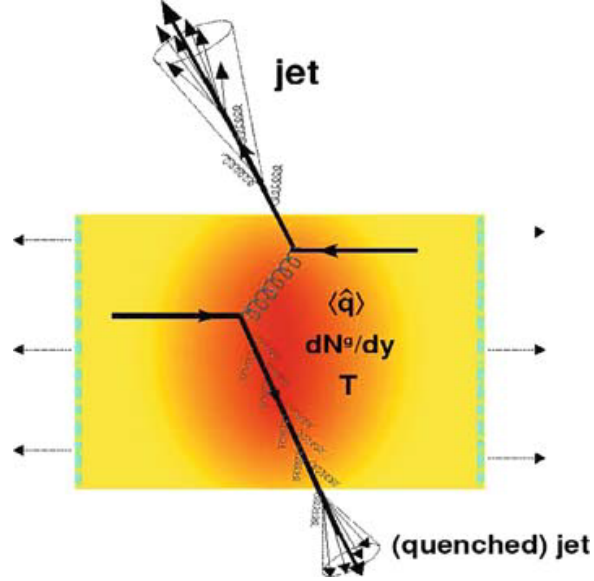


Fig 1.7: Jet quenching in central nucleus-nucleus collision. Partons which produced in the initial hard scattering lost energy inside the matter according to its properties (e.g. transport coefficient \hat{q} or gluon density dN^g/dy). [18]

can be interpreted as energy loss of high- p_T partons in the hot and dense matter produced in the reaction as illustrated in Fig. 1.7.

Some fundamental information about the medium properties are extracted from the energy loss, ΔE . In general, the lost energy is affected both by the particle characteristics (energy and mass) and by the properties of the matter (particle-medium coupling α , medium temperature T , particle path length in the medium L and so on).

1.3.1 Mechanism of Parton Energy Loss in QCD Matter

Energetic partons traversing the QGP medium lose energy via QCD processes which can be categorised as eliciting collisional or radiative energy loss [18]. Energy loss mechanism is conjectured to be responsible of the strong jet quenching observed in central heavy-ion collisions. The relative strengths of radiative and collisional energy loss contributions to jet quenching, and more generally the detailed mechanisms at work in the jet-medium interaction are still a topic of intense theoretical developments and can be studied by the measurement of the jet nuclear modification factor which is the subject of the thesis.

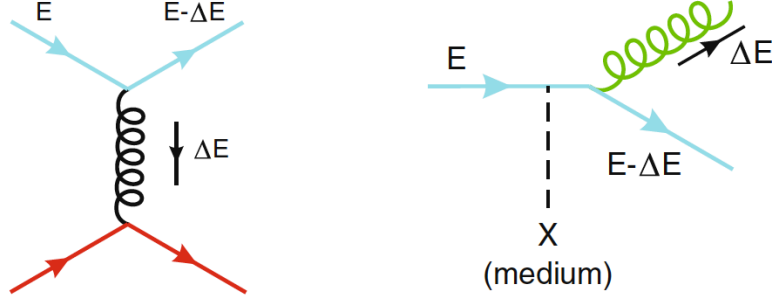


Fig 1.8: Diagrams for collisional (left) and radiative (right) energy loss of quark with energy E . [18]

Collisional Energy Loss

The collisional energy loss originates from the parton elastic scatterings with the medium constituents (diagram in Fig. 1.8 left). The average loss of energy per scattering is given by

$$\langle \Delta E_{\text{coll}}^{1\text{scat}} \rangle = \frac{1}{\sigma T} \int_{m_D^2}^{t_{\text{max}}} t \frac{d\sigma}{dt} dt \quad (1.2)$$

where $d\sigma/dt$ is the cross section of the incoming parton-medium interaction, t is the corresponding momentum transfer and $m_D \sim \alpha_s^{1/2} T$ is the Debye mass which characterises the lowest momentum exchange with the medium. The collisional energy loss due to elastic scatterings of a parton with energy E inside QGP of temperature T was originally estimated by Bjorken and Braaten-Thoma [22] and later on augmented (including running coupling, finite energy kinematics, and quark mass effects) by several authors [23, 24, 25]. Using Eq. 1.2 with integral limits of the momentum-transfer as

1. the QGP Debye mass squared, $t_{\text{min}} = m_D^2(T) \simeq 4\pi\alpha_s T^2(1 + N_f/6)$
where N_f is the number of flavours,
2. and $t_{\text{max}} = s \simeq ET$,

and taking the primary contribution of the t -differential parton-parton elastic cross section to be:

$$\frac{d\sigma}{dt} \approx C_i \frac{4\pi\alpha_s(t)}{t^2}, \quad \text{where } \alpha_s(t) = \frac{12\pi}{(33 - 2n_f) \ln(t/\Lambda_{\text{QCD}}^2)} \quad (1.3)$$

where $C_i = 9/4, 1, 4/9$ are the colour factors for $gg, gq,$ and qq scatterings respectively, finally, the collisional energy loss per unit length has the following form for:

1. Light quarks and gluons

$$-\left. \frac{dE_{\text{coll}}}{dl} \right|_{q,g} = \frac{1}{4} C_R \alpha_s(ET) m_D^2 \ln \left(\frac{ET}{m_D^2} \right) \quad (1.4)$$

2. Heavy quarks

$$-\left. \frac{dE_{\text{coll}}}{dl} \right|_Q = -\left. \frac{dE_{\text{coll}}}{dl} \right|_{q,g} - \frac{2}{9} C_R \pi T^2 \left[\alpha_s(M^2) \alpha_s(ET) \ln \left(\frac{ET}{M^2} \right) \right]. \quad (1.5)$$

with $C_R = 4/3$ (3) being the quark (gluon) colour charge. The amount of ΔE_{coll} is linear with the medium thickness, and it depends only logarithmically on the initial parton energy (c.f. Fig. 1.9).

Radiative Energy Loss

Radiative energy loss through inelastic scatterings within the medium (diagram in Fig. 1.8 right), can be determined using the spectrum of single or double differential gluon/photon bremsstrahlung ($\omega dI_{\text{rad}}/d\omega$ or $\omega d^2I_{\text{rad}}/d\omega dk_{\perp}^2$):

$$\Delta E_{\text{rad}}^{1\text{scat}} = \int^E \omega \frac{dI_{\text{rad}}}{d\omega} d\omega, \text{ or} \quad (1.6)$$

$$\Delta E_{\text{rad}}^{1\text{scat}} = \int^E \int^{k_{\perp}^{\text{max}}} \omega \frac{d^2I_{\text{rad}}}{d\omega dk_{\perp}^2} d\omega dk_{\perp}^2. \quad (1.7)$$

where ω and k_{\perp} are the energy and transverse momentum of the radiated gluon/photon respectively.

Considering incoherent scatterings, the total energy loss is simply given by $\Delta E^{\text{tot}} = N \cdot \Delta E^{1\text{scat}}$, where $N = L/\lambda$ is the opacity and $\lambda = 1/(\rho\sigma)$ is the mean-free-path of the parton in the medium. Thus, the stopping power, the lost energy in unit length, is expressed as:

$$-\frac{dE}{dl} = \frac{\langle \Delta E^{\text{tot}} \rangle}{L}, \quad (1.8)$$

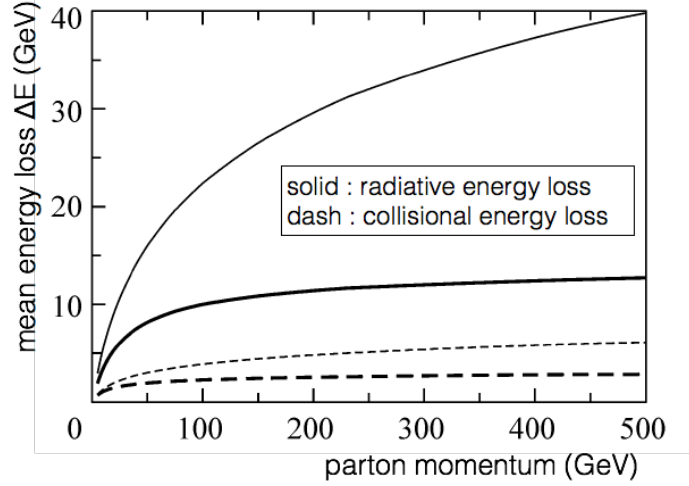


Fig 1.9: Light quark radiative and collisional energy loss for $\sqrt{s_{\text{NN}}} = 5.5$ TeV conditions for $L=5$ fm. The thick curves correspond to the running α_s and thin curves to $\alpha_s = 0.5$, utilise the T-dependent Debye mass from the lattice calculations. [26]

which reduces to $-dE/dl = \langle \Delta E^{1\text{scat}} \rangle / \lambda$ for incoherent scatterings.

A parton traversing a QGP loses energy by medium induced multiple gluon emission. The radiated gluon spectrum, $\omega dI(\omega, l)/d\omega$, has been computed under various approximations. The starting point is the QCD radiation probabilities given by DGLAP splitting functions ($P_{q \rightarrow gg}$): $\omega dI(\omega)/d\omega \propto P_{q \rightarrow gg}(\omega/E)$, modified to take into account the enhanced medium induced radiation. All medium modifications are often encoded into the “transport coefficient” parameter, $\hat{q} \equiv m_D^2/\lambda$, defined as the average transverse momentum squared gained by the incoming parton per unit distance λ . For thin (thick) media, one deals with the Bethe-Heitler (Landau-Pomeranchuk-Migdal) gluon bremsstrahlung spectrum. In the LPM case, one further differentiates between the soft and hard gluon emission cases with respect to the characteristic gluon radiation energy $\omega_c = 1/2 \hat{q} L^2$. Making use of Eq. 1.6 and Eq. 1.7, the basic QCD radiative energy loss formulas read

1. Bethe-Heitler (BH) regime

$$\omega \frac{dI_{\text{rad}}}{d\omega} \approx \alpha_s C_R \frac{\hat{q} L^2}{\omega} \Rightarrow \Delta E_{\text{rad}}^{\text{BH}} \approx \alpha_s C_R \hat{q} L^2 \ln \left(\frac{E}{m_D^2 L} \right) \quad (1.9)$$

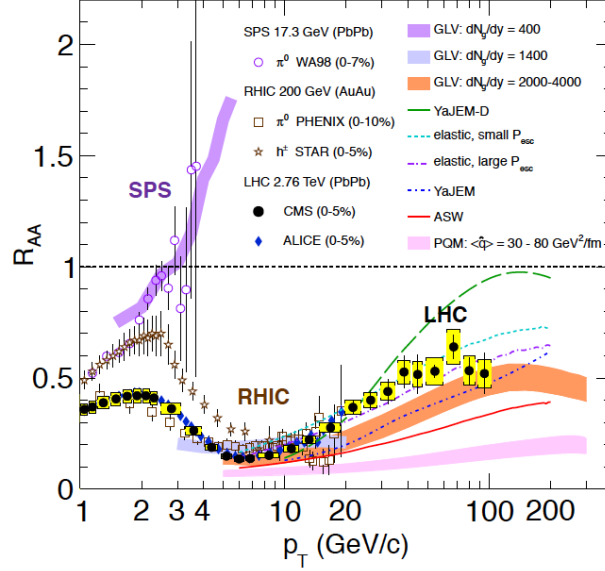


Fig 1.10: Single particle nuclear modification factor R_{AA} for different collision energies up to 2.76 TeV. [27]

2. Landau-Pomeranchuk-Migdal (LPM) regime

$$\omega \frac{dI_{\text{rad}}}{d\omega} \approx \begin{cases} \alpha_s C_R \sqrt{\hat{q} L^2 / \omega} \\ \alpha_s C_R \hat{q} L^2 / \omega \end{cases} \Rightarrow \Delta E_{\text{rad}}^{\text{LPM}} \approx \begin{cases} \alpha_s C_R \hat{q} L^2 & (\omega < \omega_c) \\ \alpha_s C_R \hat{q} L^2 \ln(E / (\hat{q} L^2)) & (\omega > \omega_c) \end{cases} \quad (1.10)$$

One can note that the main differences between the energy loss in a QCD and QED plasma are the colour factors (C_R) and the extra logarithmic dependence of ΔE_{rad} on the energy E of the traversing particle.

1.3.2 Experimental Results of Jet Quenching

The effect of energy loss can be quantified through the nuclear modification factor (R_{AA}) as mentioned above, which is defined as the ratio of single (identified) particle or jet yields per event in heavy-ion collisions (dN^{AA}) over those in pp (dN^{PP}), as follows:

$$R_{AA} = \frac{dN^{\text{AA}}/dp_T}{\langle N_{\text{coll}} \rangle dN^{\text{PP}}/dp_T} = \frac{dN^{\text{AA}}/dp_T}{\langle T_{AA} \rangle d\sigma^{\text{PP}}/dp_T}. \quad (1.11)$$

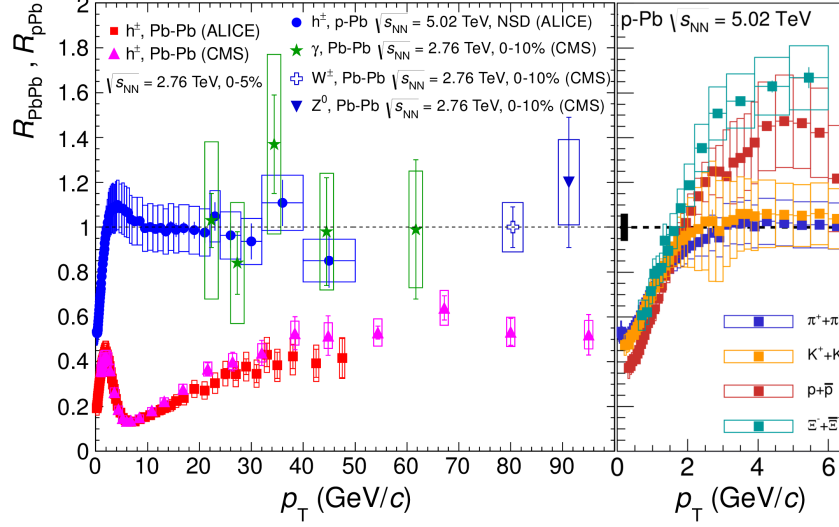


Fig 1.11: (left) Single particle nuclear modification factor R_{AA} (for Pb-Pb collisions at $\sqrt{s_{NN}} = 2.76$ TeV) and R_{pA} (for p-Pb collisions at $\sqrt{s_{NN}} = 5.02$ TeV) of particles at LHC energies. (right) for four particle species. [27]

$\langle T_{AA} \rangle$ is the nuclear overlap function, and $\langle N_{\text{coll}} \rangle = \langle T_{AA} \rangle \times \sigma_{\text{inel}}^{\text{NN}}$ is the average number of nucleon-nucleon collisions occurring in heavy-ion collisions. $\langle N_{\text{coll}} \rangle$ is calculated with a Glauber model consisting of a detailed description of the nuclear collision geometry (for a review see [17]).

No in-medium modification results in a R_{AA} equal to unity. R_{AA} less than unity could suggest a reduction of production rate, energy loss of the particles or its mother particle. Additionally for jets, it suggests the change of the jet structure due to jet(parton)-medium interactions. R_{AA} amplitude and overall trend as a function of transverse momentum, centrality, rapidity, particle specie (heavy or light quarks) and collision energy, can reveal the underlying mechanism at work (shadowing, Cronin effect, medium back-reaction or absorption, interplay of quark/gluon quenching, and parton spectra), but with the caveat that several effects might balance out each other resulting in a null net effect. For instance, the increase of $\sqrt{s_{NN}}$ should result in both a hardening of the spectrum shape and a larger energy loss which compensate each other, the arising R_{AA} being unmodified.

The charged particle nuclear modification factors measured at SPS, RHIC and LHC are shown in Fig. 1.10. The LHC results at $\sqrt{s_{NN}} = 2.76$ TeV show a slightly stronger

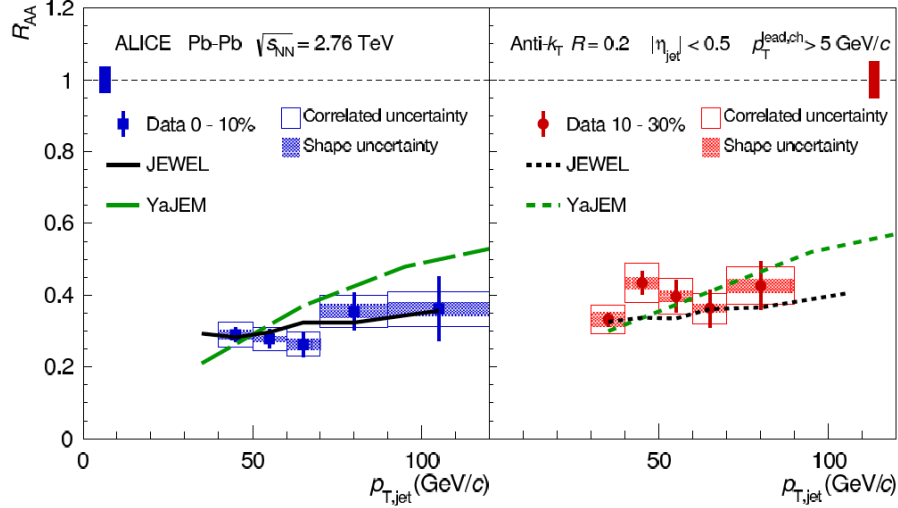


Fig 1.12: Nuclear modification factor R_{AA} of $R = 0.2$ jets in 0-10%(left) and 10-30%(right) most central Pb-Pb collisions at $\sqrt{s_{NN}} = 2.76$ TeV, comparing to the calculations from two kind of model (YaJEM and JEWEL). [28]

suppression than those from RHIC (Au-Au, $\sqrt{s_{NN}} = 200$ GeV) and SPS (Pb-Pb, $\sqrt{s_{NN}} = 17.3$ GeV); the largest measured suppression, in the 6 to 9 GeV/c in p_T range, is a factor of about 7 at the LHC, while at RHIC only a factor of 5 was observed. A novelty observed at the LHC is that with increasing p_T the suppression becomes smaller: the R_{AA} suppression is followed by a rising trend from $p_T \sim 6$ GeV/c, but it is still smaller than unity at about 100 GeV/c. This demonstrates that even very energetic partons of highest p_T suffer considerable energy loss when interacting with the medium.

The measurements of the R_{AA} of charged hadrons and electro-weak bosons is shown in Fig. 1.11 on the left panel; the charged-particle R_{AA} in central Pb-Pb collisions at $\sqrt{s_{NN}} = 2.76$ TeV is compared with the R_{AA} of W , Z (from leptonic decays) and (isolated) photons at the same energy, as well as the R_{pA} from p-Pb collisions at $\sqrt{s_{NN}} = 5.02$ TeV. Although hadron production is strongly suppressed, isolated photons, W and Z bosons which do not carry colour charge are not suppressed. This observation is compatible with the hypothesis that the origin of the suppression of charged hadrons are final-state strong interactions with the created hot and dense medium. Additionally, R_{pA} , meant to distinguish initial from final-state effects support the same conclusion. The R_{pA} ALICE measurement at high p_T is

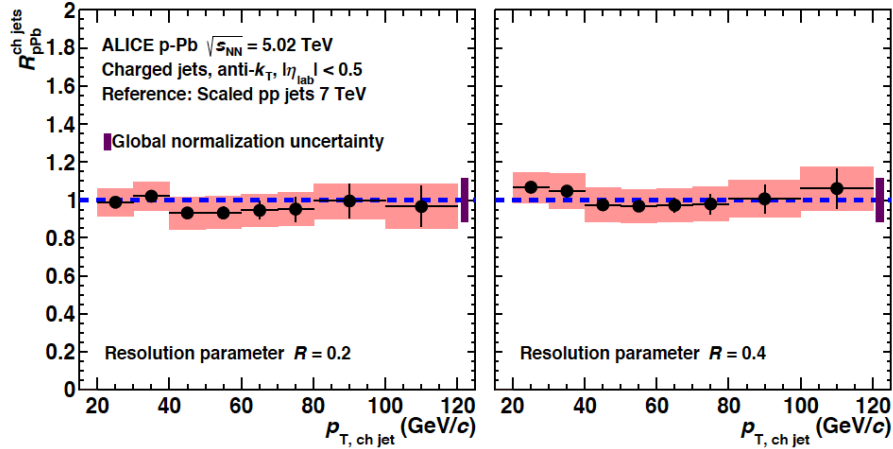


Fig 1.13: Nuclear modification factor R_{pA} of charged jets for $R = 0.2$ (left) and $R = 0.4$ (right) in $\sqrt{s_{NN}} = 5.02$ TeV p-Pb collisions. [29]

comparable with unity. It shows no indication of hadron production modification due to nuclear matter and is consistent with binary collision scaling. In conclusion, the global view tends to confirm that the observed suppression of the high- p_T hadron production in central Pb-Pb collisions is not imputable to initial-state effect, but instead to the presence of dense quark-gluon matter.

The jet nuclear modification factor measured in Pb-Pb collisions at $\sqrt{s_{NN}} = 2.76$ TeV and p-Pb collisions at $\sqrt{s_{NN}} = 5.02$ TeV are shown in Fig. 1.12 and Fig. 1.13 respectively. The jet production similarly shows strong suppression in central Pb-Pb collisions (a factor of about 3). Conversely in p-Pb collisions the jet R_{pA} is close to one. This support the hypothesis of parton-medium interactions. The jet suppression in mid-central (10-30%) collisions is slightly lower than in the most central collisions. The observed suppressions are in fair agreement with predictions from jet quenching models.

1.4 Thesis Motivation

As mentioned in previous section, the strong suppression of single particles/jets observed in the central AA collisions is interpreted as in terms of parton energy loss through parton-medium interaction. However, studying jet quenching via single particle measurements biases the jet population towards surface emission, and furthermore limits the access to the

full dynamics of the energy loss mechanism. Fully reconstructed jets copiously produced at the LHC thanks to the increase of centre-of-mass energy, are instead expected to give better access to the initial parton kinematics (direct comparison to theory made easier), mitigate fragmentation bias by capturing the jet substructure in-medium modifications (provided that the jet radius is taken large enough). Besides the fully reconstructed jet production cross section measurements, this thesis presents a phenomenological study of jet quenching in AA collisions at highest-ever centre of mass energy of 5.02 TeV.

Chapter 2 Experimental Setup

2.1 A Large Hadron Collider

The Large Hadron Collider (LHC) is a two-ring-superconducting hadron accelerator constructed at CERN. It is installed in the existing 26.7 km circular tunnel constructed between 1984 and 1989 for the CERN Large Electron-Positron Collider (LEP). Many superconducting magnets are used to bend or focus the beams around the circumference of the LHC, e.g. 1232 of 15 metre length dipole magnets and 392 of 5-7 metres quadrupole magnets.

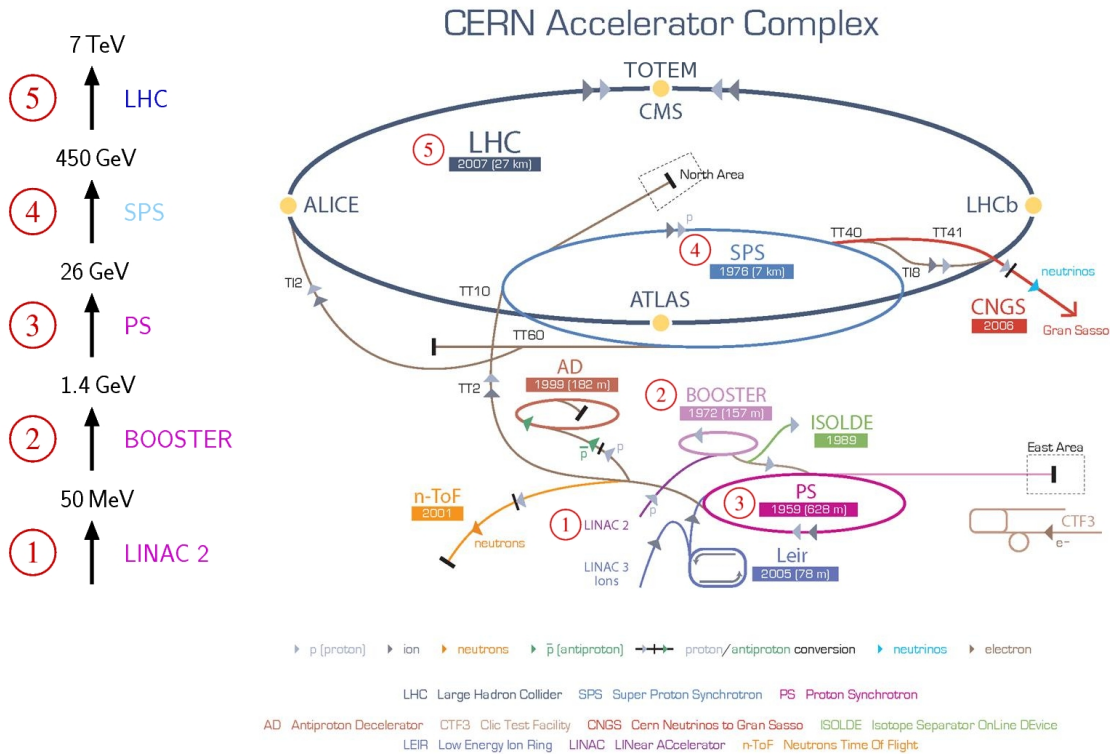


Fig 2.1: Schematic of the CERN accelerator complex. [30]

Year	Collision system	\sqrt{s} or $\sqrt{s_{\text{NN}}}$ (TeV)	Peak Lumi. ($\text{cm}^{-2}\text{s}^{-1}$)
2009	pp	0.9	–
		2.36	–
2010	pp	7	0.21×10^{33}
	Pb-Pb	2.76	0.03×10^{27}
2011	pp	2.76	–
		7	3.7×10^{33}
	Pb-Pb	2.76	0.51×10^{27}
2012	pp	8	7.7×10^{33}
	p-Pb	5.02	–
2013	pp	2.76	–
	p-Pb	5.02	–
2015	pp	5.02	0.32×10^{33}
		13	5.0×10^{33}
	Pb-Pb	5.02	2.7×10^{27}
2016	pp	13	13.8×10^{33}
	p-Pb	8.16	–
2017	pp	5.02	–
		13	20.6×10^{33}
	Xe-Xe	5.44	–

Tab 2.1: Summary of LHC runs operated until 2017 [31]. The peak luminosities are measured at ATLAS.

Almost all these superconducting magnets adopt the “two-in-one” or “twin-bore” design, one for clockwise beam (Beam 1) and the other for anti-clockwise beam (Beam 2).

The CERN accelerator complex is shown in Fig. 2.1. The particle beams are transferred from one machine to another with increasing energy before their injection in the LHC (Fig. 2.1). The first accelerator of the chain is the Linac 2 injector for proton beams (up to $50 \text{ MeV}/c$) or the Linac 3 injector for heavy-ion beams (up to $160 \text{ MeV}/c$), followed by the Proton Synchrotron (PS) and the Super Proton Synchrotron (SPS) (up to $450 \text{ GeV}/c$). Subsequently, the beams are divided and supplied to two transfer lines, one for Beam1 and the other for Beam 2, and are finally fed in the LHC rings.

The LHC was designed to deliver collisions with centre-of-mass energy of $\sqrt{s} = 14 \text{ TeV}$ for proton-proton collisions, and $\sqrt{s_{\text{NN}}} = 5.5 \text{ TeV}$ for Pb-Pb ion collisions. The design luminosity of the LHC is $10^{34} \text{ cm}^{-2}\text{s}^{-1}$ for pp collisions and $10^{27} \text{ cm}^{-2}\text{s}^{-1}$ for Pb-Pb collisions.

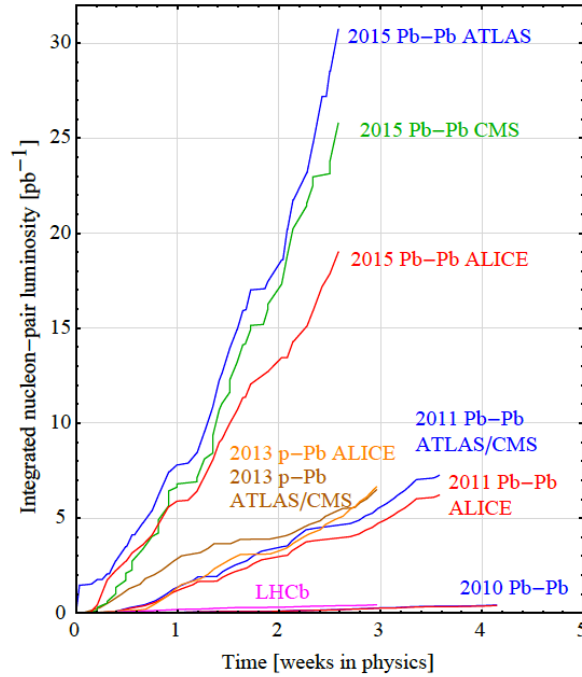


Fig 2.2: Nucleon-nucleon integrated luminosity delivered to each experiment for all LHC heavy-ion runs to date. [32]

LHC reached the design luminosity for Pb-Pb collisions (in 2015) and pp collisions (in 2016); and in 2017, it exceeded its design pp luminosity by a factor 2. The LHC energy ramp up is still on-going although the bending magnet training was limited so far to 6.5 TeV /*beam* in pp.

The LHC started regular operation from 2009 and since then, various collision systems and energies were provided (see Tab. 2.1). Detectors are installed in experimental caverns at the 4 collision points: the ATLAS (at Point 1), CMS (at Point 5), ALICE (Point 2) and LHCb (Point 8). Fig. 2.2 summarises the integrated luminosity delivered by the LHC to each experiment during Pb-Pb and p-Pb Run1 and Run2 (still on-going at the time of writing this document).

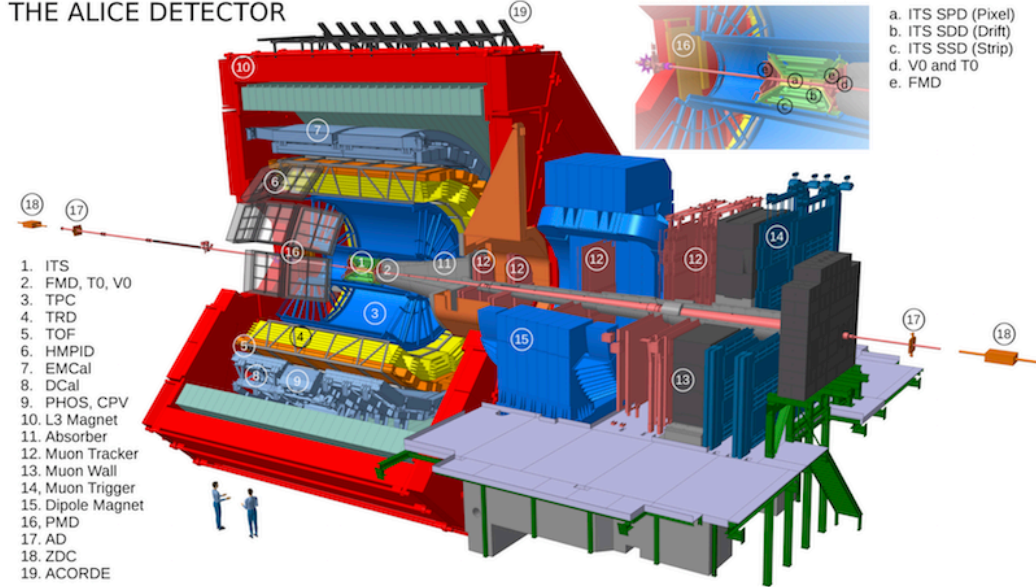


Fig 2.3: Cut-away view of the ALICE detector. [33]

2.2 The ALICE Experiment

The ALICE experiment is the only LHC experiment dedicated to the study of QGP, and consequently optimised for heavy-ion collisions. ALICE started to record pp collision data in 2009 at the LHC injection energy ($\sqrt{s} = 900$ GeV). The first high-energy pp and Pb-Pb runs at respectively $\sqrt{s} = 7$ TeV and $\sqrt{s_{NN}} = 2.76$ TeV successfully took place in 2010. At the end of 2011, a second Pb-Pb run of much higher statistics followed. In 2013, ALICE collected data of asymmetric p-Pb collisions. After the first LHC long shutdown period (LS1), the second LHC run started in 2015 with increased beam energies.

ALICE is a 10,000-ton detector, 26 m long, 16 m high, and 16 m wide. The detector is designed to measure the particles produced in the collisions which take place at its centre, so that the evolution of the system produced during these collisions can be reconstructed and studied. To achieve this goal, many different sub-detectors providing different pieces of information were installed. ALICE consists of 19 sub-detectors, which use different techniques to measure particles. The ALICE detector layout is given in Fig. 2.3.

To access the collision centrality Zero Degree Calorimeters (ZDC) [34] which are located about 110 m away on both sides of the ALICE interaction point, measure the number of

spectators. FMD, V0 and T0 detectors [35] measure the signal from participants and their spatial distribution. Furthermore, T0 supplies high precision measurement of interaction time used for fast timing and triggering.

Charged particle reconstruction is provided by data from a set of cylindrical tracking detectors called “central barrel detectors” (from inside to outside: ITS [36], TPC [37] and TRD [38]) which sample the particle trajectories into many hits. These tracking detectors are immersed in a longitudinal magnetic field ($B_{\max} = 0.5 T$), produced by the former L3 experiment solenoid magnet, which bends particle trajectories to measure their momentum.

The particle identification (PID) is provided by combining momentum measurement with dE/dx measurement given by ITS and TPC or velocity of charged particles measured with TOF [39]. TOF measures time of flight traveling from the primary vertex with a precision of a few tens of ps. Additionally, particle-specific features are exploited for PID; the HMPID [40] measures the Cherenkov light patterns generated by fast particles extending the PID toward high p_T and the TRD measures transition radiation which is emitted when fast and lightweight particle (mainly electron) crosses boundary of materials of different dielectric constants, enabling the discrimination between electrons and pions.

Electrons and photons are measured using the ALICE electromagnetic calorimeters: EMCAL [41], DCAL [42], and PHOS [43] (PHOS is a homogeneous lead-tungsten crystal calorimeter, EMCAL and DCAL are lead/scintillator sampling calorimeters). PHOS performs high energy- and position-resolution measurement in a limited area, while EMCAL and DCAL have larger acceptance suitable for jet measurement but with worse energy resolution.

In the following, a further description of the detectors used in the analysis presented in this thesis will be given.

2.2.1 V0 detector

The V0 detector is a forward detector consisting of two arrays of 32 scintillating counters, called V0A and V0C, which sits on each side of the ALICE interaction point. The V0A is located 330 cm away from the primary vertex while the V0C is mounted at 90 cm in the opposite direction. They cover the pseudo-rapidity regions of $2.8 < \eta < 5.1$ (V0A) and $-3.7 < \eta < -1.7$ (V0C) as shown in Fig. 2.4.

V0 is made by plastic scintillator BC404 (2.5 and 2.0 cm thickness for V0A and V0C,

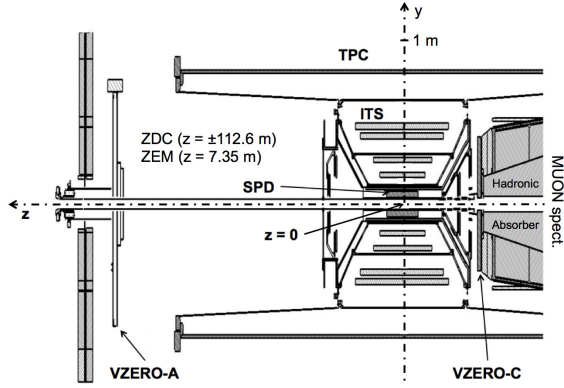


Fig 2.4: Position of the two VZERO detectors in the ALICE layout. [44]

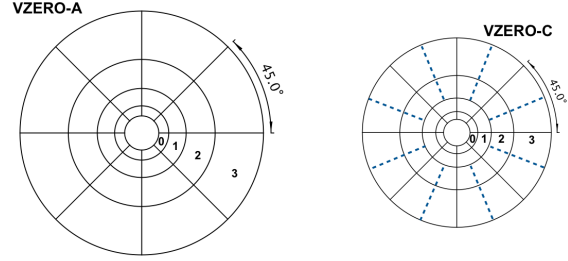


Fig 2.5: The segmentation of V0A and V0C. The two scintillator segments divided by dashed line are read out by the same PMT. [44]

respectively). The scintillating light is collected by photomultipliers (PMT) through Wave-Length Shifting (WLS) fibres of 1 mm in diameter.

The V0A array has 32 individual counters arranged in 4 rings and 8 sectors of 45° (see Fig. 2.5). The V0C array has 48 individual counters distributed following two inner rings of 8 counters and two outer rings of 16 counters. The latter are paired to build one single cell.

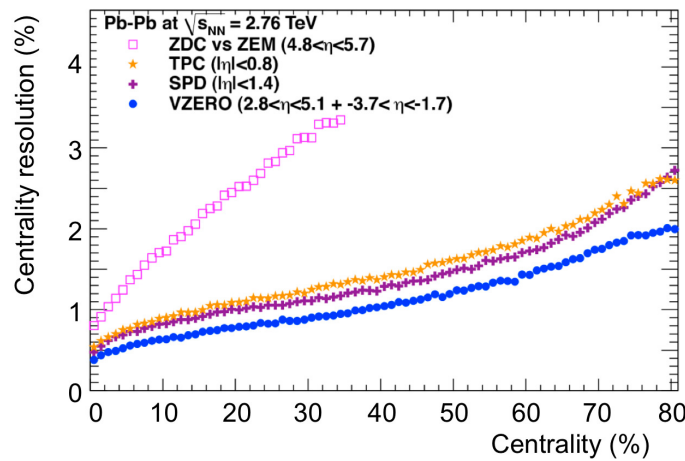


Fig 2.6: Centrality percentile resolution versus centrality in Pb-Pb collisions at $\sqrt{s_{NN}} = 2.76$ TeV for various ALICE detectors. [44]

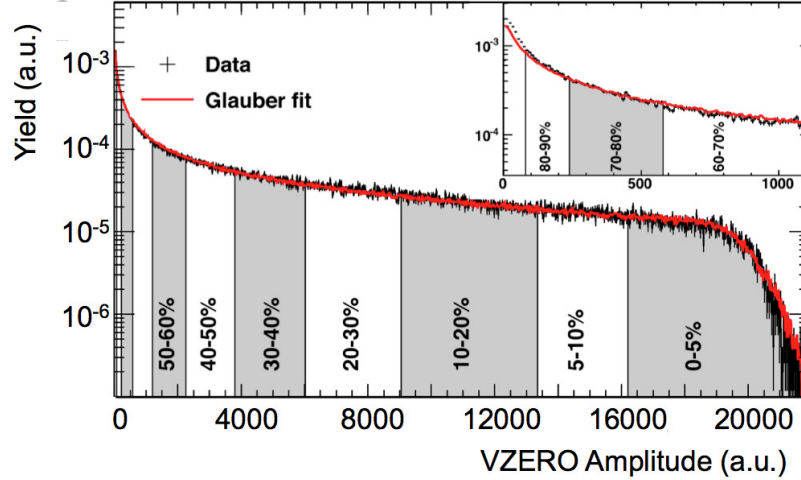


Fig 2.7: Distribution of the sum of amplitudes in V0A and V0C in Pb-Pb collisions at $\sqrt{s_{NN}} = 2.76$ TeV. The red line shows the fit with a Glauber model. [44]

The V0 detector is dedicated to the:

- discrimination of beam-gas interactions by correlating V0A and V0C timing,
- estimation of collision centrality and event plane by V0A and V0C amplitudes,
- measurement of the charged particle multiplicity density.

In particular, a high resolution collision centrality estimation is of prime importance for all heavy-ion measurements which include system size dependence. V0 detector allows for the best centrality resolution as can be seen in Fig. 2.6. The centrality is estimated from a Glauber based fitting of the charge sum distribution of the two V0 detectors (see Fig. 2.7).

2.2.2 Inner Tracking System (ITS)

ITS consists of two layers of Silicon Pixel Detectors (SPD), two layers of Silicon Drift Detectors (SDD) and two layers of Silicon Strip Detectors (SSD) from inside out (see Fig. 2.8). It is the most inner detector among central barrel detectors, covering central pseudo-rapidity range of $|\eta| < 0.9$ and distance from the beam pipe from $r = 4$ cm up to $r = 44$ cm (4 cm and 7 cm for SPD, 15 cm and 24 cm for SDD, 39 cm and 44 cm for SSD). The four inner layers (SPD and SDD) provide a 2-dimensional tracking to separate tracks in a large track density environment up to 90 tracks/cm², while 1-dimensional read-out is sufficient for the

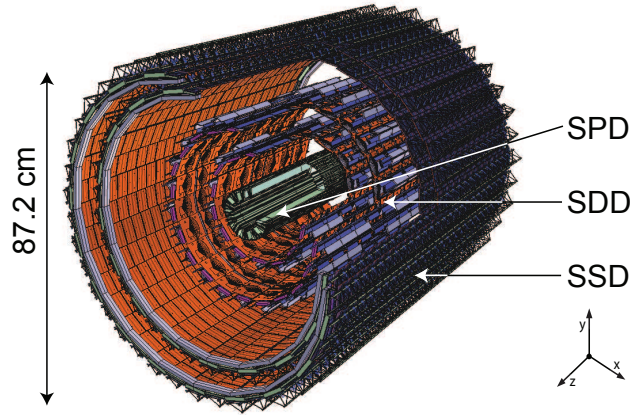


Fig 2.8: Layout of the ITS which constituted in SPD, SDD and SPD. [45]

two outermost layers (SSD) due to smaller track densities. Outer four layers (SDD and SSD) provide an analog read-out to measure the energy loss (dE/dx) of particles traversing them.

ITS is used to:

- measure secondary vertices from weak decays of strange, charm and beauty particles,
- improve tracking of charged particles (especially at low- p_T) in combination with other detectors (TPC, TRD),
- reconstruct primary vertex position with high precision ($< 100 \mu\text{m}$).

The charged particle p_T resolution as function of p_T (Fig. 2.9) shows that a primary vertex constraint and/or the incorporation of ITS space point in the tracking drastically improve tracking resolution compared to TPC only tracks, particularly at high- p_T .

2.2.3 Time Projection Chamber (TPC)

TPC is the largest tracking device of the ALICE central barrel (and moreover, the world's largest TPC) with a cylindrical shape of 88 m^3 volume covering distance from the beam pipe from $r = 85 \text{ cm}$ to $r = 250 \text{ cm}$ and pseudo-rapidity range of $|\eta| < 0.9$ (corresponding to 500 cm in the beam direction).

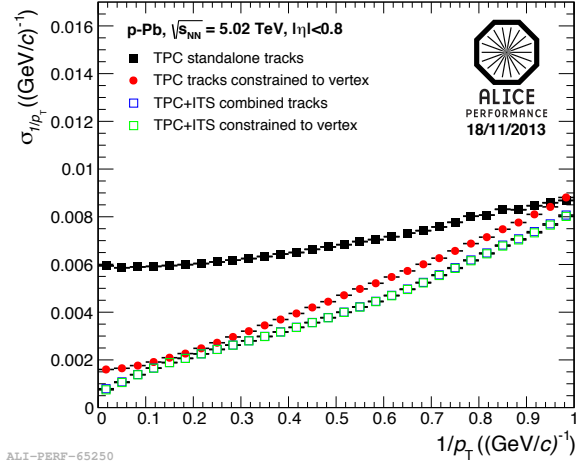


Fig 2.9: Charged particle $1/p_T$ resolution ($= \sigma(p_T)/p_T^2$) as a function of $1/p_T$ for TPC and ITS in p-Pb collisions at $\sqrt{s_{NN}} = 5.02$ TeV. [33]

The TPC geometry is shown in Fig. 2.10. It is divided into two drift regions by a central electrode, filled with an $Ar-CO_2$ (or $Ne-CO_2$) gas mixture. A uniform electric field of 400 V/cm is applied in each volume along beam direction to transport ionisation electrons towards the readout pad chambers within a maximum drift time of ~ 100 μs . The signals

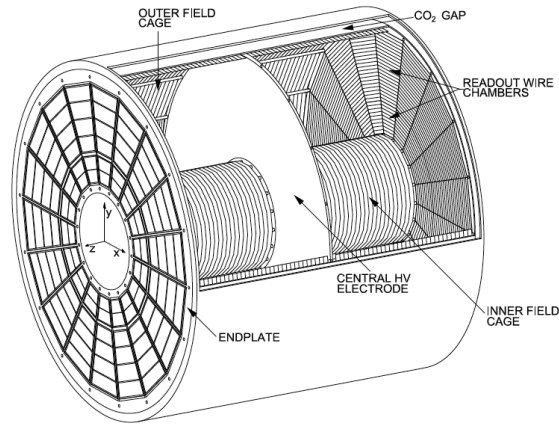


Fig 2.10: Schematic view of the TPC field cage. [37]

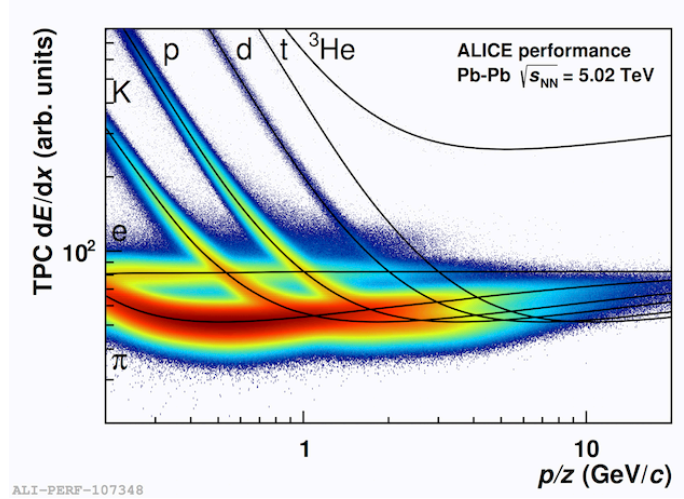


Fig 2.11: TPC dE/dx as a function of momentum with superimposed Bethe-Bloch lines for various particle species, measured in Pb-Pb collisions at $\sqrt{s_{NN}} = 5.02$ TeV. [33]

read out by the $\sim 557k$ pads of multi-wire proportional end plate chambers allow for particle trajectory reconstruction and measurement of their energy loss (dE/dx) in the TPC gas volume which is used for PID (Fig. 2.11).

2.2.4 Electromagnetic Calorimeters (EMCAL, DCAL and PHOS)

The EMCAL and DCAL are lead-scintillator sampling calorimeters with large acceptance, comprising 12,288 and 5,376 individual towers respectively. They are located inside the ALICE solenoid magnet, occupying a cylindrical volume of approximately 110 cm deep in the radial direction, with front face located at 450 cm from the beam line (see Fig. 2.12). The basic detector unit of EMCAL/DCAL is a “module” comprising 2×2 independent detection channels (towers). The module is a sandwich of 77 plastic scintillator layers and 76 lead foils which corresponds to $20.1 X_0$ radiation lengths.

A particle passing through the module and interacting with the lead produces an electromagnetic shower, which in turn produces light in the plastic scintillators. Avalanche Photodiodes (APD) convert the light which is collected and guided by WLS optical fibres, into an electrical signal.

The structural units of EMCAL and DCAL are called “Super Modules” (SMs) arranged following a continuous arch, spanning 20° in azimuth. The Super Modules are classified into

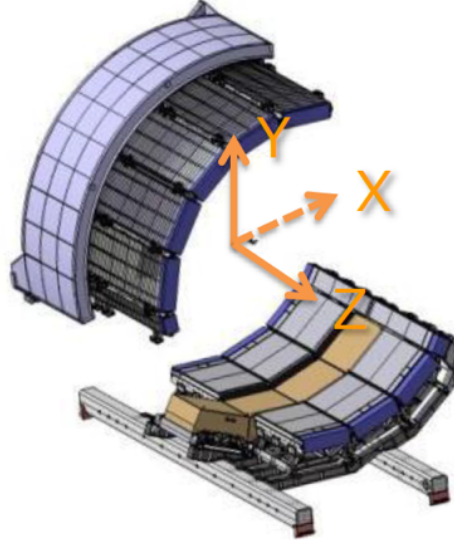


Fig 2.12: Three calorimeters installed in ALICE at Run2 period: EMCAL (upper side), PHOS (bottom side, drawn in orange) and DCal (placed on both side of PHOS in z -direction).

two types, full size and one-third size SMs. Each full size Super Module consists of 24×12 modules for EMCAL and 16×12 modules for DCAL, and one-third size SM contains 24×4 modules. A total of 10 full size SMs and 2 one-third SMs constitute EMCAL, while DCAL numbers 6 full size and 2 one-third SMs.

PHOS is a high resolution electromagnetic calorimeter made of lead tungstate crystals (PbWO_4), covering a limited acceptance at central rapidity, and located inside the solenoid magnet at 440 cm from the beam line. The basic unit of the detector is a “crystal” which size is $22 \times 22 \times 180\text{mm}^3$ corresponding to $20 X_0$ radiation lengths, and on which the read out APD is directly glued.

When high energy photons or electrons cross lead tungstate, they induce electromagnetic cascade (pair production and bremsstrahlung) and make it scintillate. However the lead tungstate is so dense that it stops most of the incoming photons. Furthermore, this inorganic scintillating crystals have a strong light yield temperature dependence. Therefore, in order to achieve a high energy resolution, PHOS is operated under a temperature of -25°C , where the deterioration of the energy resolution due to noise is minimised.

	EMCAL	DCAL	PHOS
Total Weight	~ 82 t	~ 36 t	12.5 t
Number of SMs	10 SMs 2 one-third SMs	6 SMs 2 one-third SMs	3 SMs 1 half SM
Coverage	$80^\circ < \phi < 187^\circ$ $ \eta < 0.7$	$260^\circ < \phi < 327^\circ$ $ \eta < 0.7$ ^a	$250^\circ < \phi < 320^\circ$ $ \eta < 0.13$
Tower size ($\Delta\eta \times \Delta\phi$)	$\sim 60 \times 60 \times 246$ mm ³ 0.0143 x 0.0143	$\sim 60 \times 60 \times 246$ mm ³ 0.0143 x 0.0143	$\sim 22 \times 22 \times 180$ mm ³ 0.004 x 0.004
Effective Rad. Length X_0	20.1	20.1	20
Effective density	5.68 g/cm ³	5.68 g/cm ³	8.28 g/cm ³
Energy resolution	$7\%/\sqrt{E} \oplus 1.5\%$	$7\%/\sqrt{E} \oplus 1.5\%$	$3.3\%/\sqrt{E} \oplus 1.1\%$

Tab 2.2: Specification of ALICE electromagnetic calorimeters

PHOS consists of 3 SMs and 1 half SM. Each SM (half SM) is made up of 56×64 (56×32) crystals; in all PHOS has 12,544 crystals. The main specifications of EMCAL, DCAL and PHOS are summarised in Tab. 2.2.

EMCAL and DCAL focus on jet physics, where the improvement of jet energy resolution is very desired for the tomographic study of QGP. They improve the charged jet measurement by adding the neutral constituents. Furthermore, the association of EMCAL and DCAL makes hadron-jet and/or jet-jet high precision correlation measurement possible, because of their back-to-back in azimuth layout in agreement with the di-jet topology. The event display in Fig. 2.13 shows a typical jet-jet event recorded during the 2015 Pb-Pb run. The primary aim of PHOS is to measure and identify photon and neutral meson from the hot QCD matter. It has been designed to detect photons produced over a wide energy range, up to 100 GeV and reconstruct neutral mesons decaying to photons with very high energy and position resolutions.

In Fig. 2.14 and Fig. 2.15, the $\pi^0 \rightarrow \gamma\gamma$ invariant mass distribution measured in EMCAL and PHOS respectively are shown. A clear peak is observed (larger S/B) even in the very demanding heavy-ion environment.

^awith exception: $260^\circ < \phi < 320^\circ$, $|\eta| < 0.25$

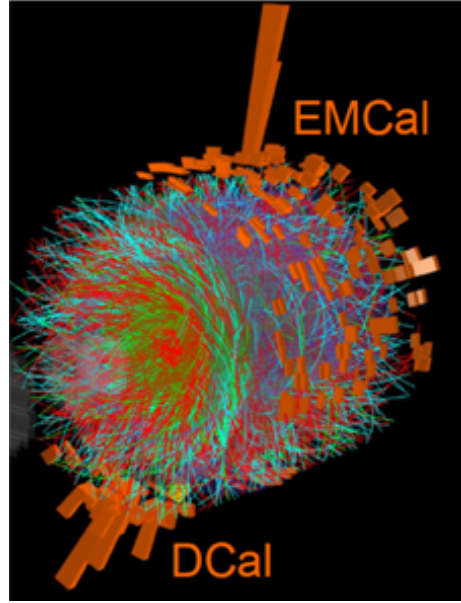
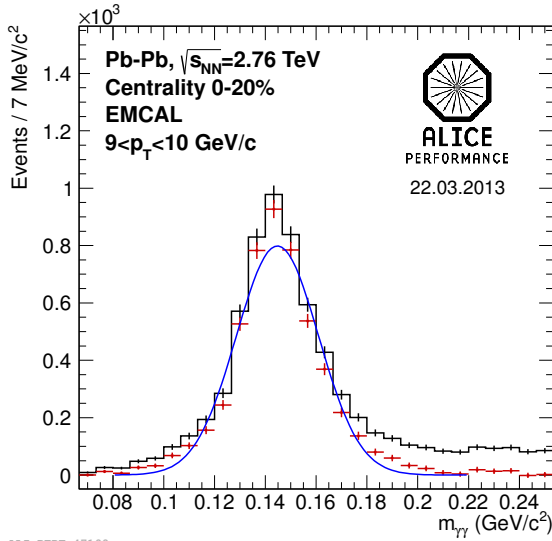
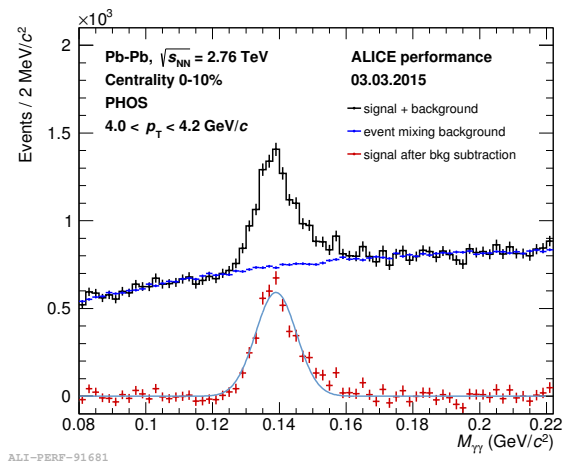


Fig 2.13: ALICE event display taken in 2015 Pb-Pb run. [33]

Fig 2.14: Invariant mass spectrum of photon pairs with $p_T = 9-10$ GeV/c measured in EMCAL in $\sqrt{s_{NN}} = 2.76$ TeV Pb-Pb collisions at centrality 0-20%. [33]Fig 2.15: Invariant mass spectrum of photon pairs with $p_T = 4.0-4.2$ GeV/c measured in PHOS in $\sqrt{s_{NN}} = 2.76$ TeV Pb-Pb collisions at centrality 0-10%. [33]

Chapter 3 ALICE Calorimeter Trigger Development

During the two-year long shutdown period (LS1) from 2013, LHC accelerator was upgraded to achieve higher beam luminosity and beam energy close to design values. At the same time, the ALICE experiment took the chance to upgrade some of its detectors to cope with the new beam conditions and keep improving measurements of QGP properties.

During LS1, a new Electromagnetic calorimeter “DCAL” was installed to enhance the acceptance for neutral particles and measure di-jet energy with charged plus neutral particles. Along with this upgrade, a new online trigger system was deployed to select and enrich dataset with rare events including jets or high p_T photons.

In this section, the trigger system which was developed by the author during LS1 for the ALICE EMCAL/DCAL is presented.

3.1 Overview of Trigger Generation

The trigger inputs from each detector are treated by the Central Trigger Processor (CTP) of the ALICE trigger system. These trigger inputs are grouped into three successive levels (Level-0, Level-1 and Level-2). The trigger inputs from an event of a given bunch crossing arrive to the CTP with a delay: the trigger input latency amounting to:

- 800 ns for L0 triggers
- 6,100 ns for L1 triggers
- 87,600 ns for L2 triggers

The calorimeters (EMCAL, DCAL and PHOS) are used for L0 and L1 triggering because their signals are faster than other detectors (e.g. TPC due to its large drift time). Two L1 triggers are generated by calorimeters: L1-photon and L1-Jet to select high- p_T photons and jets respectively.

L1 trigger signals are produced by the Summary Trigger Unit (STU) which is displayed on Fig. 3.1. To generate output signals, the STU processes a number of inputs. Trigger

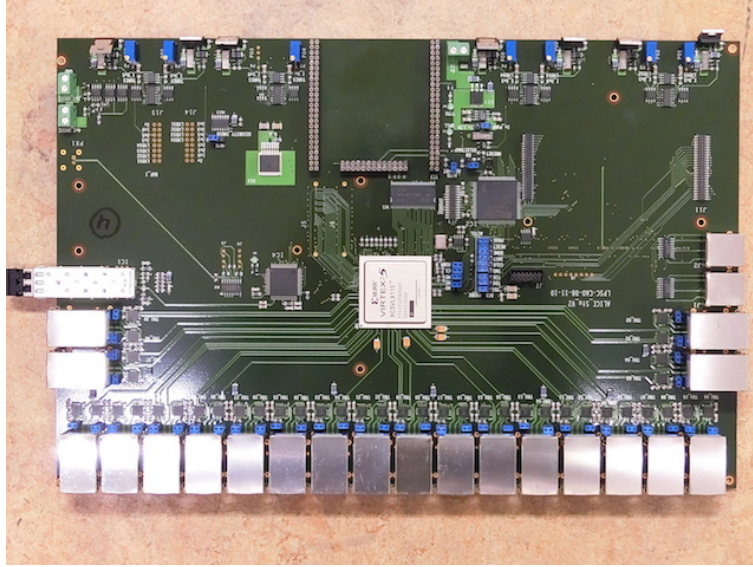


Fig 3.1: Summary Trigger Unit board (STU).

Region Units (TRU) in charge of triggering at local areas of the detector (1 TRU handles signals from 1/3 of a SM). TRUs provide a single photon trigger (L0) receiving an analog sum of each group of 2×2 adjacent towers from the Front End Electronics (FEE) cards. This group of towers is called “Module” or “FastOR” and is the smallest unit of trigger calculation. Subsequently, FastOR signal amplitudes are flash digitised in the TRU and used as STU inputs. The relation between each trigger unit is shown in Fig. 3.2.

EMCAL (DCAL) has totally 3,072 (1,344) FastORs and PHOS has 12,544 crystals which corresponds to 3,136 FastORs. One FEE card can deal with 8 modules, and one TRU is in charge of 12 FEEs (for EMCAL and DCAL) or 14 FEEs (for PHOS). The TRU coverage in detector coordinate system is shown in Fig. 3.3 and Fig. 3.4. The STU collects FastORs’ amplitudes and produces L1 triggers following its internal trigger algorithm.

The L1 trigger calculation is carried out by a FPGA (Xilinx Virtex-5) mounted on the STU board. During LHC LS1, the upgrade of the ALICE calorimeter trigger system was accomplished by developing an original STU firmware.

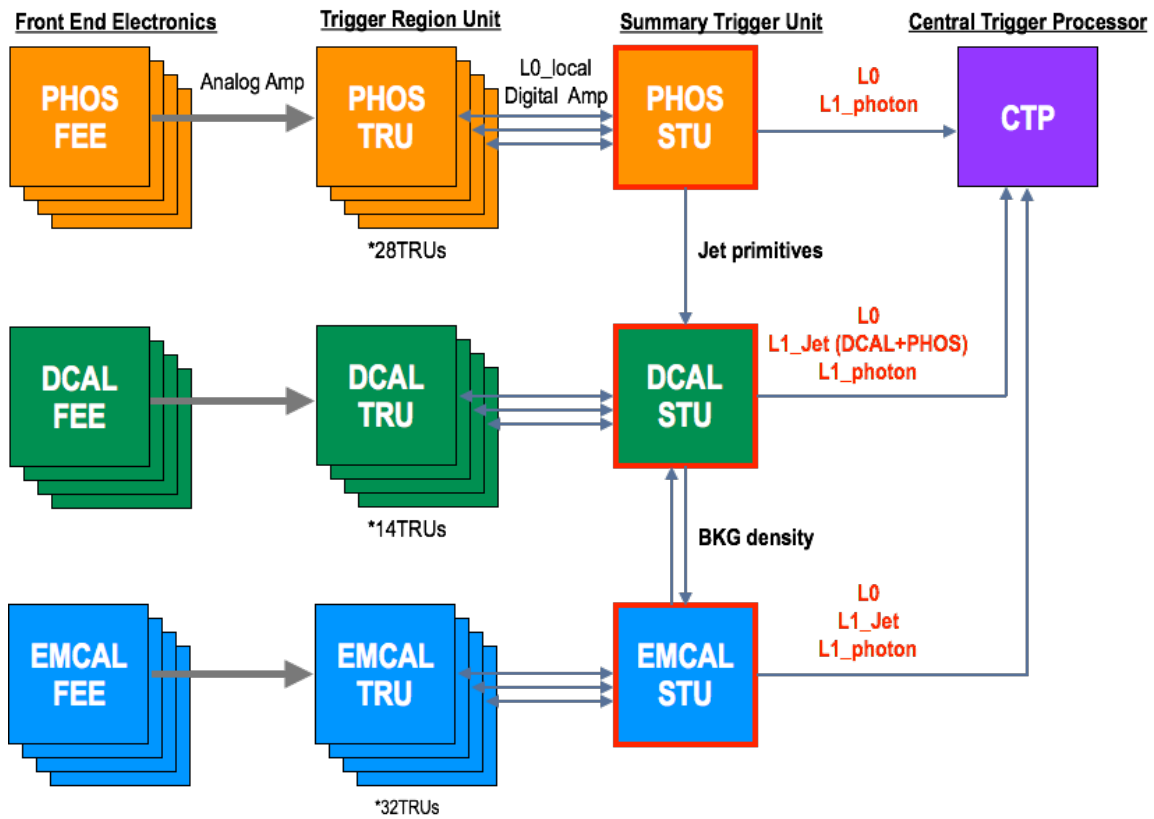


Fig 3.2: Data flow of L1 trigger production in ALICE calorimeters. In total 7 L1-photon triggers (3 for PHOS, 2 for DCAL and 2 for EMCAL) and 4 L1-Jet triggers (2 for DCAL and 2 for EMCAL) are generated.

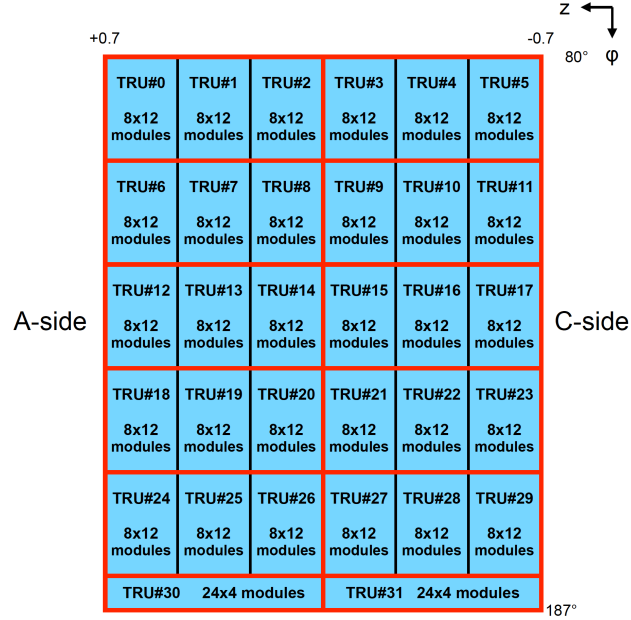


Fig 3.3: EMCAL geometry in terms of trigger production. Each TRU charged area contains 96 FastORs.

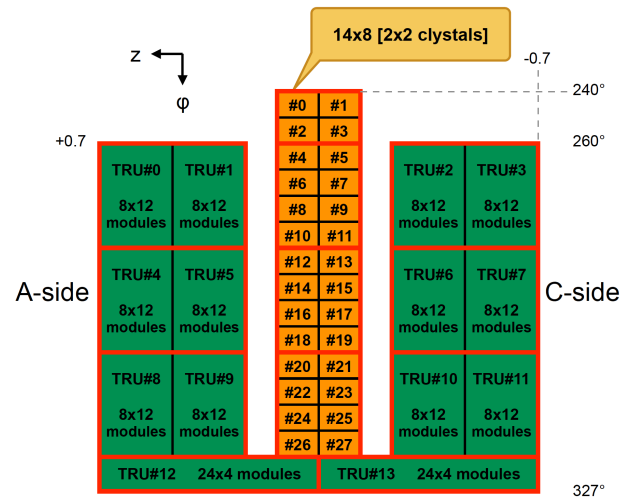


Fig 3.4: DCAL+PHOS geometry in terms of trigger production. Each PHOS (DCAL) TRU contains 112 (96) FastORs respectively.

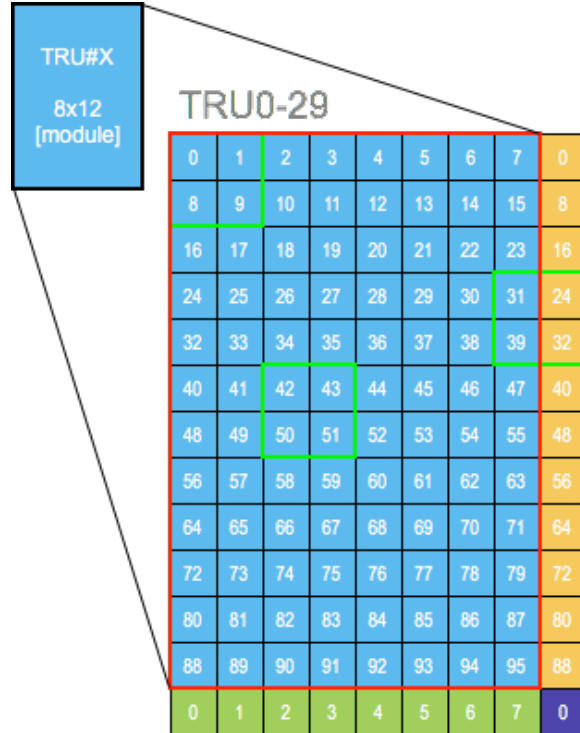


Fig 3.5: Example of L1-photon patch ($= 2 \times 2$ FastORs). Amplitudes of these patches are calculated over TRU boundaries.

3.2 L1 Trigger Algorithm

Taking advantage of the freshly commissioned DCAL back-to-back in azimuth to the EMCAL, the new L1 trigger algorithms exploit this two-arm setup by aggregating DCAL and PHOS regions to estimate the event energy density and thereby correct EMCAL trigger patches from soft background contamination, and vice versa. The new approach (a.k.a. median mode), besides providing uniform trigger efficiency across event centrality, makes the calorimeter triggers more self-consistent (using energy measurements only) without relying anymore on the V0 detector to compute a multiplicity-dependent trigger threshold as implemented during LHC Run1. Furthermore, preliminary Monte-Carlo simulations have also predicted shaper trigger turn-on curves.

The L1-photon trigger calculation starts from summing up the amplitudes within a 2×2 FastOR trigger patch. The patch slides in units of FastOR and scans the whole detector

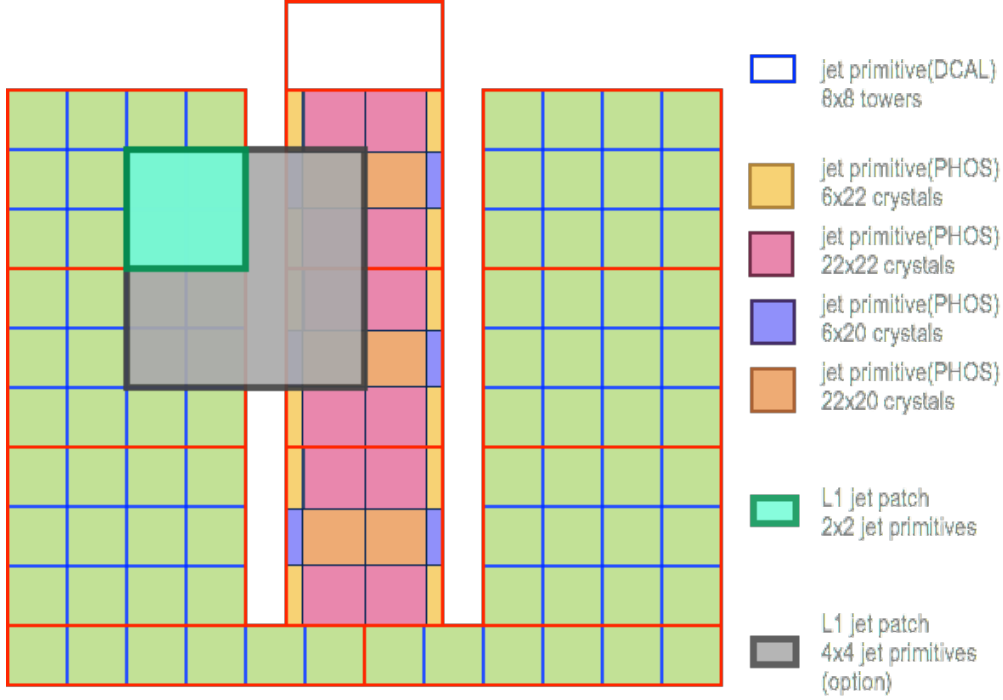


Fig 3.6: Example of L1-Jet patches ($= 2 \times 2$ or 4×4 jet-primitives) in DCAL+PHOS side.

area including TRU boundaries (see Fig. 3.5). This process is running on-the-fly while receiving TRU data. The same sliding window method is applied for L1-Jet calculation but with a larger patch size of 8×8 (or 16×16) FastORs, and a sliding unit of 4×4 FastORs which is called “jet primitive”.

In fact, the optimum threshold, which is made up of only bulk contribution, depends on underlying event density which fluctuates event-by-event. Thus, the estimated event background should be subtracted before the comparison with threshold. In this upgrade, event background is estimated event-by-event using median calculation of background patch (correspond to 2×2 jet-primitives). This estimated background is sent to opposite side STU in azimuth and used for background subtraction. The calculation flow for L1-Jet is summarised in Fig. 3.7. In addition, the jet patches in DCAL side need to collect the amplitude of jet-primitives from PHOS due to their respective gain parameters and complicated geometry. (PHOS has been excluded from L1-Jet calculation in physics runs operated in 2015-2017.)

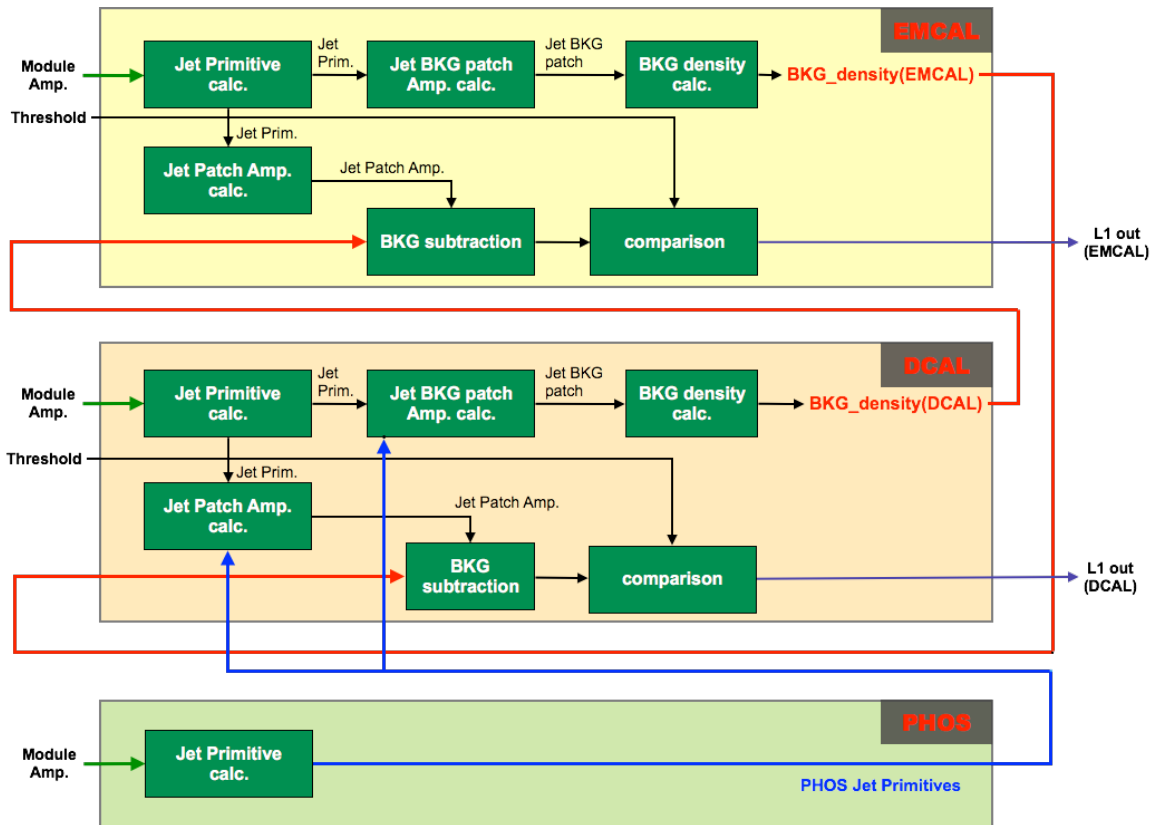


Fig 3.7: Schematic of event background calculation. Underlying event density estimated by median method are swapped between EMCAL STU and DCAL STU.

3.3 Trigger Performance

The ALICE calorimeters started operation with the new L1 median mode algorithm for the first Run2 Pb-Pb run in November 2015. Trigger performances was then evaluated from the first data recorded by STUs.

First of all, we validated the principle of background median estimate exchange between EMCAL and DCAL. Fig. 3.8 shows the correlation of background densities estimated from event-by-event median calculation of background patch in EMCAL and DCAL. The clear positive correlation observed proves firstly that both estimates are consistent and can be safely swapped, and secondly, that the data transfer between EMCAL and DCAL is reliable.

The trigger capability to control event rates for data acquisition is quantified by the trigger rejection factor defined as the fraction of events passing the trigger condition in a minimum bias events sample. The L1-photon and L1-Jet trigger rejection factors as a function of trigger threshold are shown in Fig. 3.9 and Fig. 3.10 respectively. A 10 GeV threshold gives a ~ 100 L1-photon trigger rejection, while a 20 GeV threshold results in a ~ 1000 of L1-Jet trigger rejection. Such trigger rejection factors are used for trigger threshold settings to comply with the bandwidth allocated to the calorimeters according to ALICE data taking strategy.

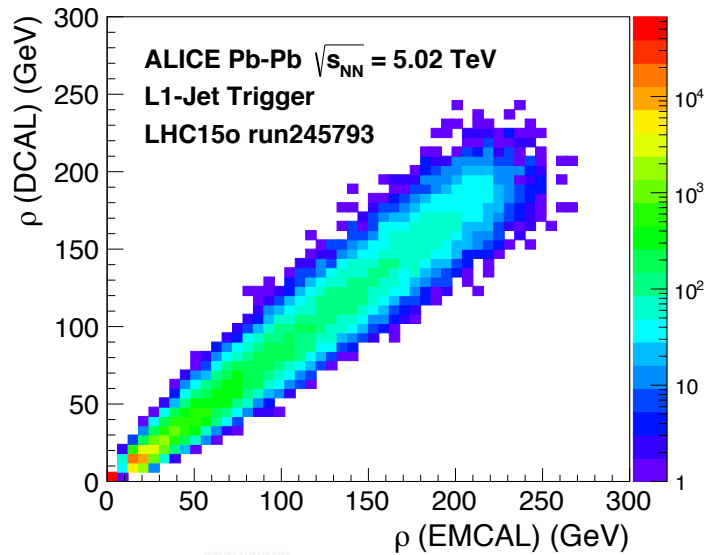


Fig 3.8: Correlation of underlying event densities estimated by DCAL and EMCAL STUs.

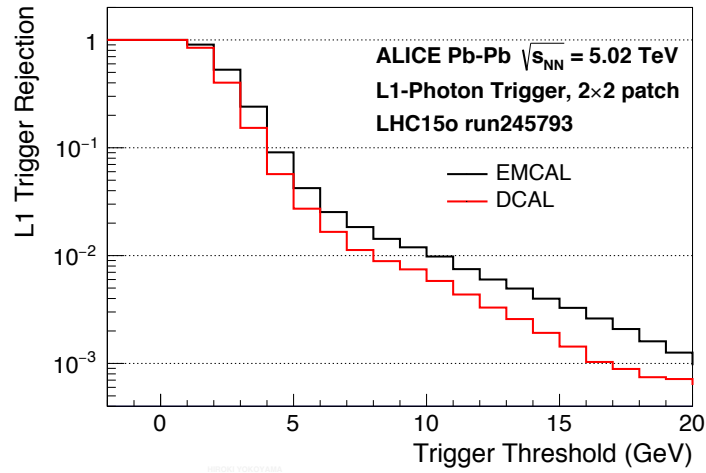


Fig 3.9: Rejection factor of L1-photon triggers given by DCAL and EMCAL in 2015 Pb-Pb run.

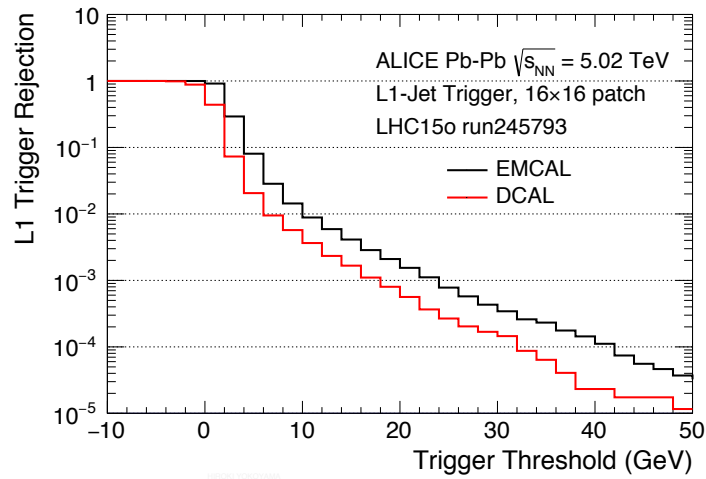


Fig 3.10: Rejection factor of L1-jet triggers given by DCAL and EMCAL in 2015 Pb-Pb run.

The other important trigger performance to assess is how rapidly full selection efficiency is reached, the so-called turn-on curve. Fig. 3.11 and Fig. 3.12 show the PHOS cluster spectrum with the L1-photon trigger and minimum bias trigger in different event centrality classes. The ratios of these spectra show clear step-function like shape around the threshold setting of 8 GeV. The height of the plateau gives the photon enhancement factor provided by the trigger system. This value is larger in peripheral collisions than central collisions. The difference comes from the fact that the PHOS L1-photon trigger does not implement any background subtraction, resulting in larger patch energies in central collisions. The trigger efficiency is evaluated by the proportion of jet/photon-trigger events in the minimum-bias trigger events. Fig. 3.13 and Fig. 3.14 show the L1-photon and L1-Jet trigger efficiencies respectively as a function of trigger patch energy measured in FEE. They also show a sharp turn-on around the threshold value.

The results shown in the Fig. 3.8 to Fig. 3.14 demonstrate the good performance of the new L1-trigger in Pb-Pb collisions. Large event samples have been collected with this triggers since its commissioning which are now being analysed for paper publication by the ALICE collaboration.

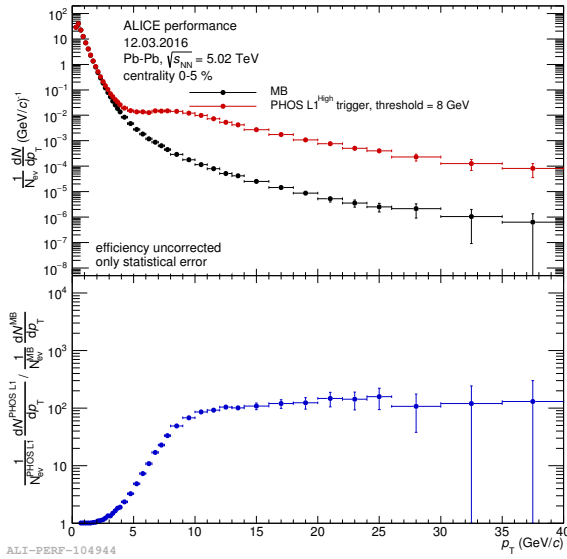


Fig 3.11: (top) p_T spectra of clusters reconstructed in PHOS with minimum bias and PHOS L1-photon triggers at 0-5% Pb-Pb collisions. (bottom) The ratio of them. [33]

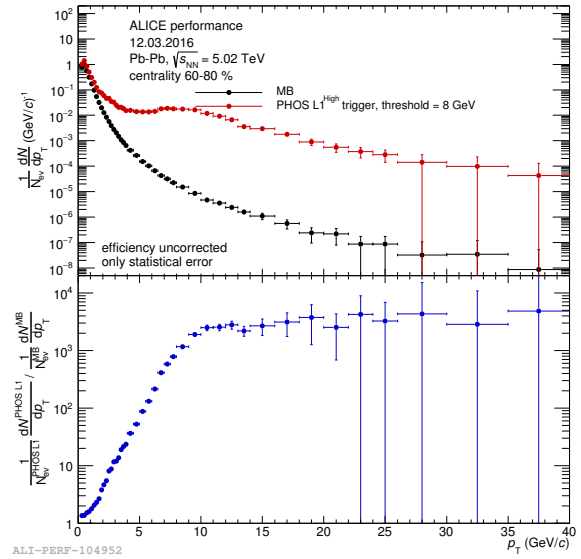


Fig 3.12: (top) p_T spectra of clusters reconstructed in PHOS with minimum bias and PHOS L1-photon triggers at 60-80% Pb-Pb collisions. (bottom) The ratio of them. [33]

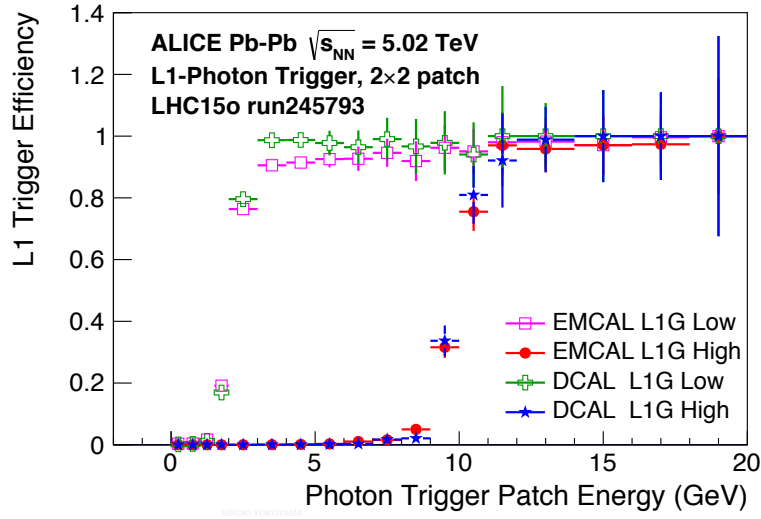


Fig 3.13: EMCAL and DCAL L1-photon trigger efficiency in 2015 Pb-Pb run.

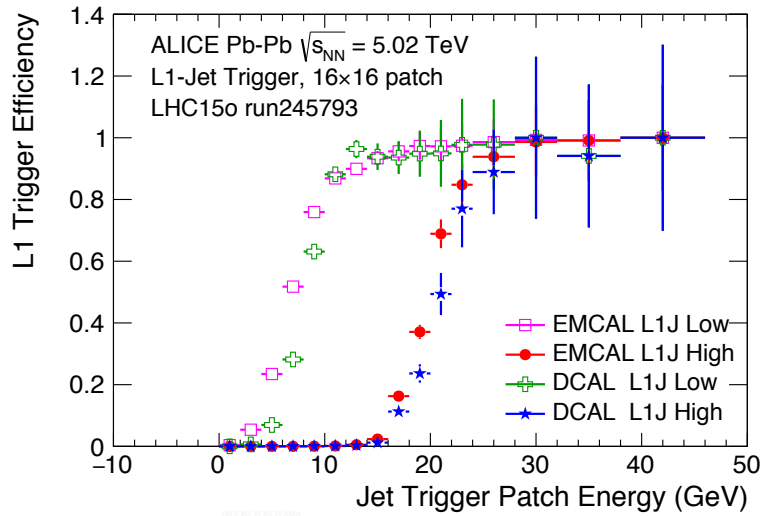


Fig 3.14: EMCAL and DCAL L1-Jet trigger efficiency in 2015 Pb-Pb run.

Chapter 4 Analysis

This chapter presents the measurement of the inclusive jet nuclear modification factor in Pb-Pb collisions at $\sqrt{s_{\text{NN}}} = 5.02$ TeV.

4.1 Data Samples

This analysis utilises two types of data samples: (i) experimental data and (ii) Monte-Carlo simulation (MC) data.

The experimental dataset is made of Pb-Pb collisions collected by the ALICE detector in 2015. A feature of this dataset was that it was taken with increasing interaction rates (from 15 Hz to 7800 Hz depending of beam tuning and filling schemes). The analysis presented hereafter is based on the lowest interaction rate data. The event statistics is 3.3M after applying event selection. The data sample was divided into four classes of centrality interval ranging from very central to peripheral collisions: 0-10%, 10-30%, 30-50% and 50-90%.

The ALICE detector response is modelled by the convolution of Pb-Pb and pp events generated by HIJING [46] and PYTHIA [47, 48] respectively, with the detector description (geometry, material, calibration. . .) from a GEANT3-based simulation [49]. The same track reconstruction code is used for data and simulation. In order to enhance the statistics of high- p_{T} jets, PYTHIA is run in bins of parton scattering transverse momentum in addition to minimum bias events. These dataset and statistics are summarised in Tab. 4.1.

Expt./MC	system	energy	statistics	remark
Expt.	Pb-Pb	$\sqrt{s_{\text{NN}}} = 5.02$ TeV	3.3M	Minimum Bias Trigger
HIJING MC	Pb-Pb	$\sqrt{s_{\text{NN}}} = 5.02$ TeV	2.5M	
PYTHIA MC	pp	$\sqrt{s} = 5.02$ TeV	20.4M	
PYTHIA MC	pp	$\sqrt{s} = 5.02$ TeV	670-680k/bin	jet production (10 pthard bins)

Tab 4.1: Dataset used for the analysis.

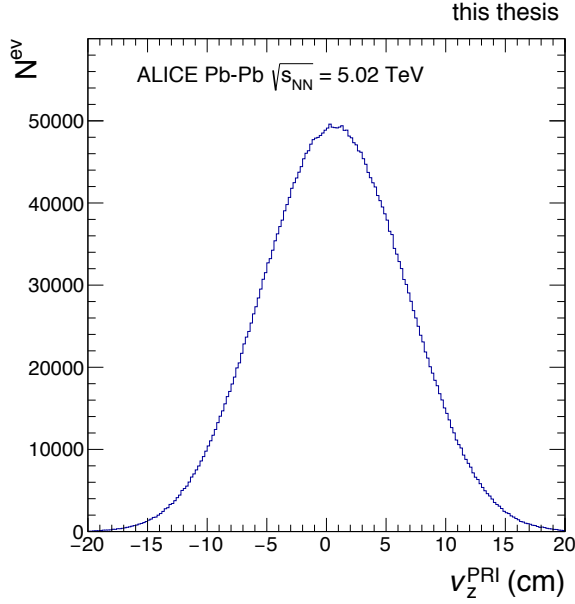


Fig 4.1: Primary vertex position along beam direction. The events with $|v_z| < 10\text{cm}$ are selected.

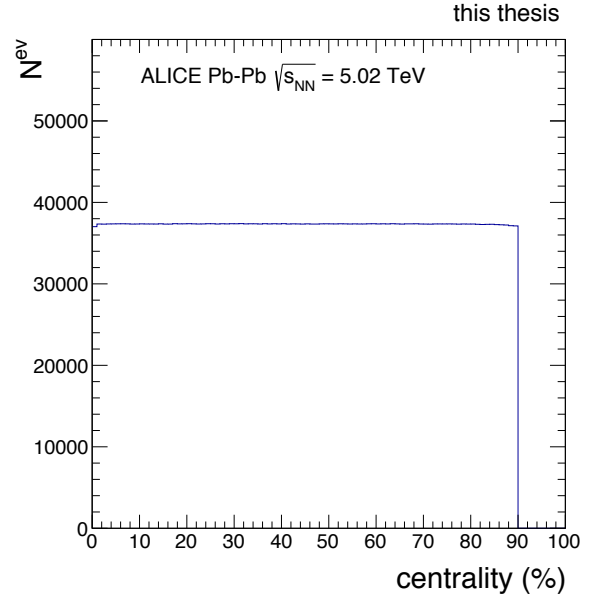


Fig 4.2: Event centrality distribution calculated with the VOM (= V0A + V0C) estimator.

4.2 Event Selection

The analysis presented in this thesis uses minimum-bias events (MB) triggered by two V0 detectors, requiring a signal in both the V0A and the V0C.

To ensure high tracking efficiency the primary vertex is required to be within 10 cm from nominal ALICE interaction point along the beam axis; $|v_z| < 10\text{cm}$. Fig. 4.1 shows the primary vertex position in beam direction. This requirement rejects $\sim 9\%$ of MB events.

To reject the remaining background events from beam-gas interaction, which generally show large signal amplitudes in the V0 detector while small track multiplicities in central barrel, the primary vertex position along the beam axis (z) reconstructed by SPD hits is used for additional requirement: $|v_z^{\text{PRI}} - v_z^{\text{SPD}}| < 0.1\text{cm}$. Fig. 4.3 shows the correlation between $v_z^{\text{SPD}} - v_z^{\text{PRI}}$ and track multiplicity. These events (outlier in Fig. 4.3) have such small numbers of tracks that the resolution of primary vertex position is bad. This event cut removes $\sim 0.3\%$ of MB events.

As seen in Fig. 4.2, the centrality distribution after event selection which is defined by V0 detector amplitude (c.f. section 2.2.1 for the definition) ensures that event cuts did not introduce any bias.

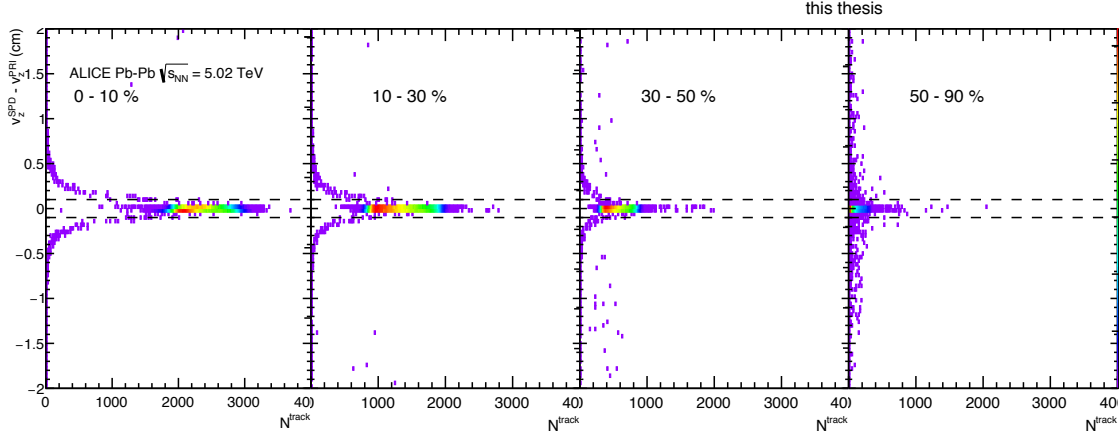


Fig 4.3: Correlation between $v_z^{\text{SPD}} - v_z^{\text{PRI}}$ and track multiplicity for four centrality classes. The events with bad vertex reconstruction resolution are rejected.

4.3 Track Selection

To avoid biasing jet reconstruction, track selection should provide a uniform η and ϕ track acceptance. The tracks are reconstructed in the ALICE central barrel (pseudo-rapidity region $|\eta| < 0.9$) with the ITS in conjunction with TPC. In order to ensure a uniform tracking efficiency in the (η, ϕ) plane despite some switched off SPD ladders, a dedicated track selection has been developed, the so-called “hybrid tracks”. The hybrid track sample is made of two exclusive track types:

- **global tracks:** with at least one hit in the SPD layers and successful inward track refit through the ITS.
- **complementary tracks:** which are primary vertex constrained global tracks with no hit in the SPD but still with a successful refit in the ITS.

The azimuthal and pseudo-rapidity distributions of the two component hybrid tracks with $p_T > 150 \text{ MeV}/c$ are given in Fig. 4.4 and Fig. 4.5 respectively. Hybrid track reconstruction succeeds in making ϕ distribution uniform. Furthermore, no centrality dependence are observed in η and ϕ distribution.

The hybrid track p_T distributions shown in Fig. 4.6 show no unusual peaks caused by hot channels or tracking reconstruction problems.

High- p_T tracks tend to be affected the inefficient area due to their straight trajectories as seen in Fig. 4.7 (blue line). The TPC sector boundaries which introduce track inefficiencies are responsible for the bumps observed in the ϕ distribution of high- p_T tracks.

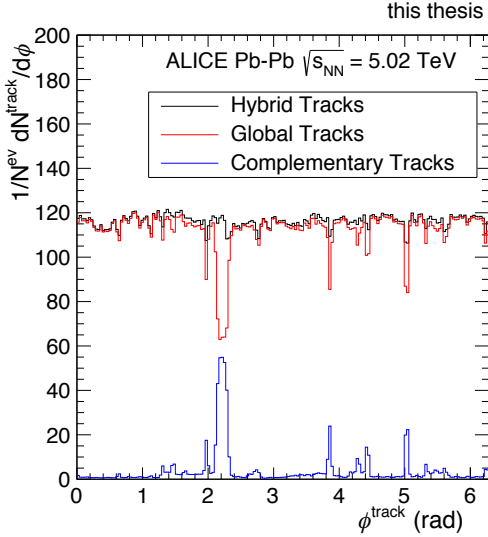


Fig 4.4: Track ϕ distributions for two components of hybrid tracks.

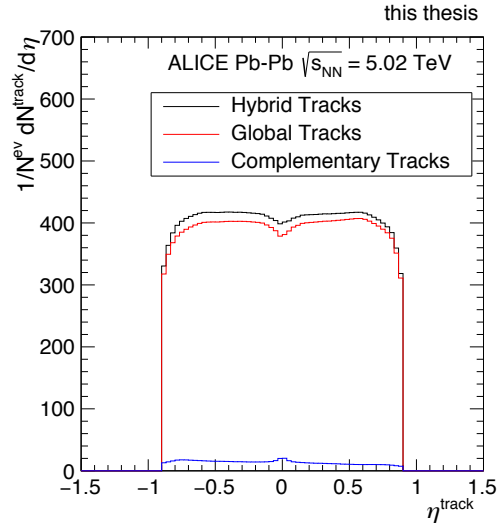


Fig 4.5: Track η distributions for two components of hybrid tracks.

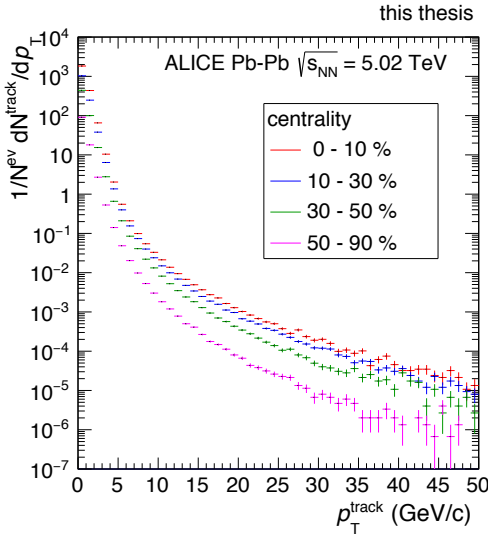


Fig 4.6: Hybrid track p_T distributions for four centrality classes.

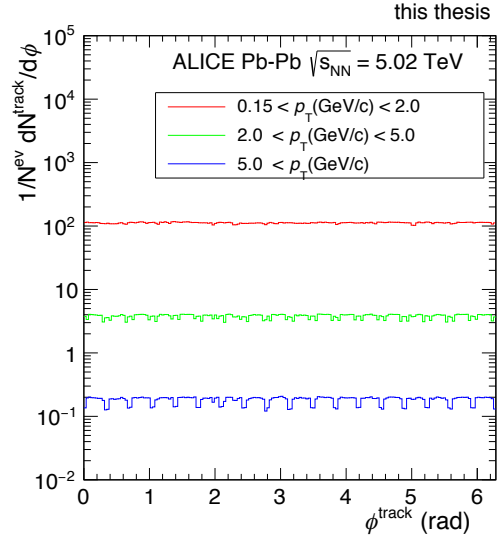


Fig 4.7: Hybrid track ϕ distributions for three transverse momentum classes.

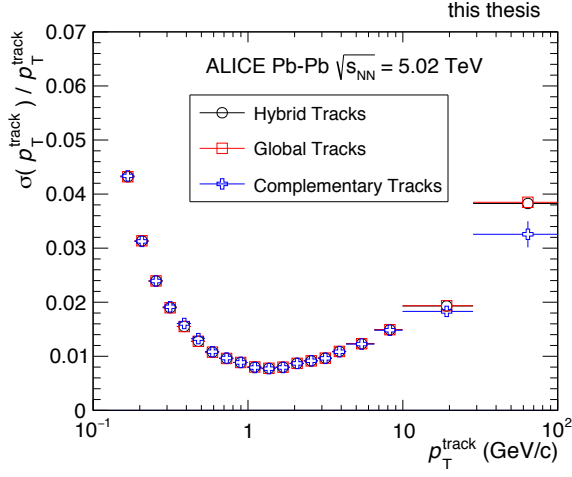


Fig 4.8: Transverse momentum resolution ($\sigma(p_T)/p_T$) for two components of hybrid tracks.

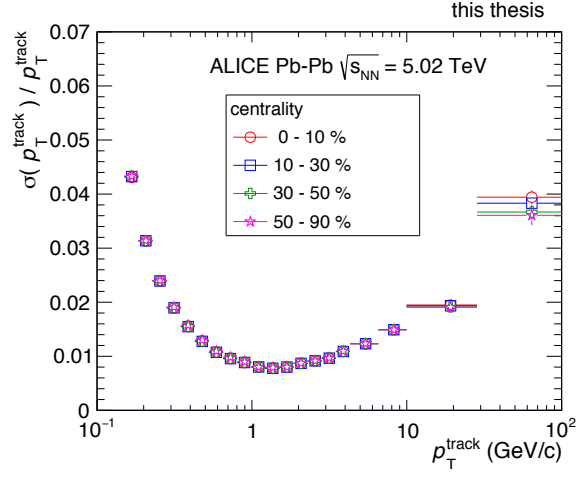


Fig 4.9: Transverse momentum resolution ($\sigma(p_T)/p_T$) for four centrality classes.

4.3.1 Tracking Resolution

The track transverse momentum resolution is extracted from the track parameter covariance matrix. The p_T resolution for two hybrid track components is shown in Fig. 4.8. The global and complementary track resolutions are similar: the difference is less than 1% at least up to 100 GeV/c. p_T resolution centrality dependence shows a small discrepancy smaller than 0.5% across all centrality classes (see Fig. 4.9). The p_T resolution of $\sigma(p_T)/p_T \simeq 0.6\%$ (4%) at 1 GeV/c (50 GeV/c) are given respectively.

4.3.2 Tracking Efficiency

The tracking efficiency of hybrid tracks is evaluated based on MC simulations: PYTHIA and HIJING events propagated through a GEANT3 detector description. On one hand, the number of generated particles is defined as all charged tracks in the final state (N^{gen}), emerging from the primary vertex within $|\eta| < 0.8$. On the other hand, the reconstructed tracks are hybrid tracks associated with generated particles ($N^{\text{rec,matched}}$) within a wider range of $|\eta| < 0.9$ in order to avoid boundary effects at the limit of detector acceptance. The ratio of above mentioned generated track p_T spectra gives the tracking efficiency:

$$\varepsilon(p_T^{\text{gen}}) = \frac{dN_{\text{matched}}^{\text{rec}}(|\eta| < 0.9)/dp_T^{\text{gen}}}{dN^{\text{gen}}(|\eta| < 0.8)/dp_T^{\text{gen}}} \quad (4.1)$$

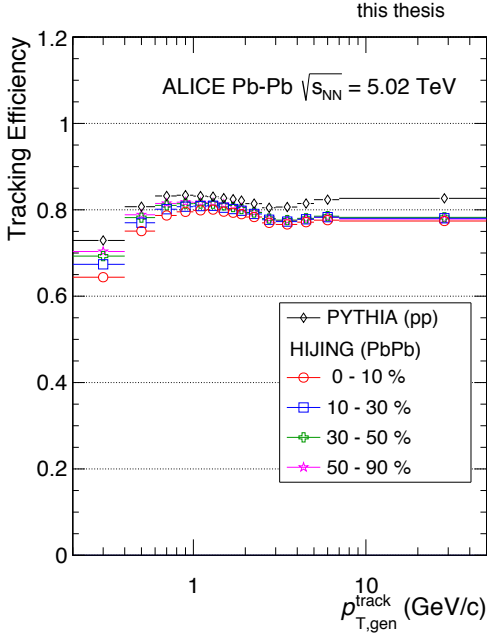


Fig 4.10: Tracking efficiency of hybrid tracks estimated by PYTHIA (pp) and HIJING (PbPb) events, propagated through GEANT simulation.

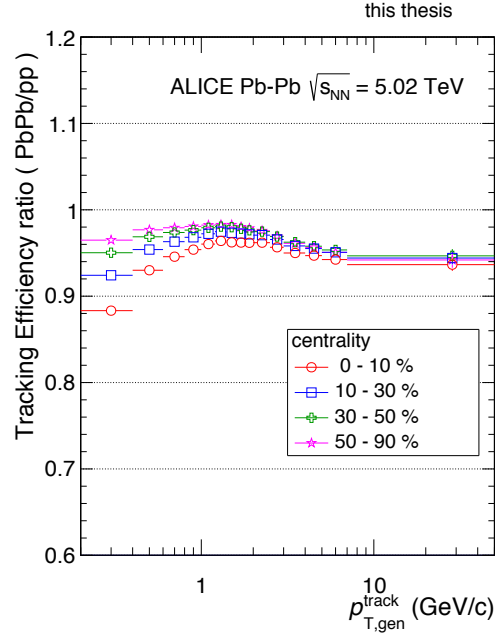


Fig 4.11: Ratio of tracking efficiency in Pb-Pb collisions to pp collisions.

The tracking efficiencies computed from HIJING and PYTHIA, and their ratio: HIJING/PYTHIA are shown in Fig. 4.10 and Fig. 4.11 respectively (for four centrality classes in HIJING). The tracking efficiency increases from about 70% at $p_T = 200 \text{ MeV}/c$ up to 80% at $p_T = 1 \text{ GeV}/c$ with a few percent decrease in central Pb-Pb collisions, mainly due to larger track multiplicities. For Pb-Pb collisions (HIJING), the tracking efficiency is from 2 to 7% smaller than that in pp collisions (PYTHIA) down to $0.5 \text{ GeV}/c$.

4.4 Jet Reconstruction

The jets are reconstructed by feeding the anti- k_T sequential clustering algorithm [50] with hybrid tracks lying within $|\eta| < 0.9$. Since in the anti- k_T algorithm, harder particles are merged first, it proves to be less sensitive to back-reaction from the soft underlying event which is particularly well suited for the Pb-Pb environment.

The anti- k_T algorithm is controlled by the input parameter named “Resolution Parameter”, R . It is sometimes called as “jet radius” since this parameter usually has a value close to the radius of the reconstructed jet. The reconstructed jets contain a number of

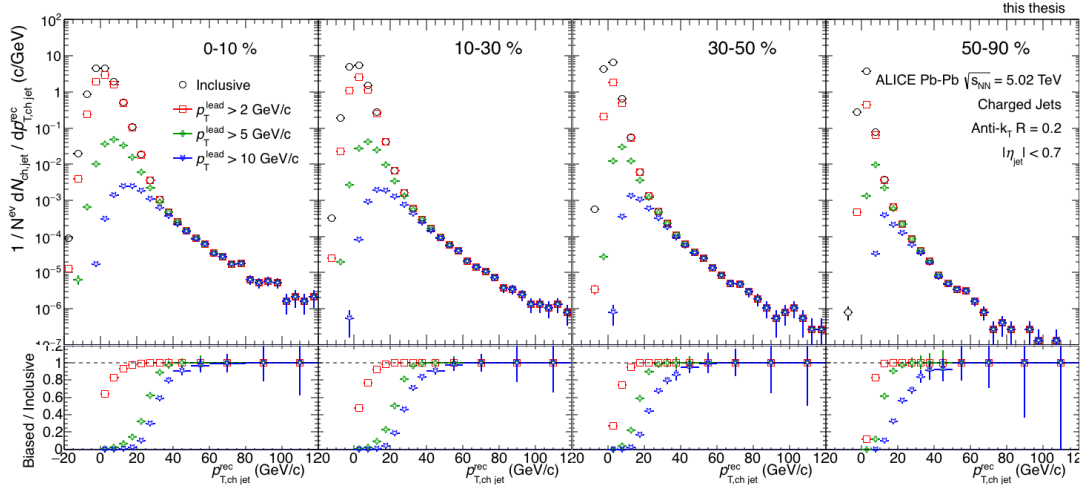


Fig 4.12: (top) Jet p_T distributions after average background subtraction for different p_T^{lead} requirements. (bottom) The ratio to inclusive jet spectrum which shows leading track p_T bias.

particles which don't originate from the initial hard partons. This phenomenon makes jet energy resolution worse especially at large R . To minimise this contamination, this analysis selects $R = 0.2$ as a resolution parameter. Furthermore, three additional requirements are applied to improve the quality of the reconstructed jet sample:

1. Jet Direction

Jets whose whole area is expected to stay within the detector acceptance: $|\eta_{jet}| < 0.9 - R$.

2. Jet Area

A minimum jet area from anti- k_T of 60% of rigid cone area is required to reduce the fake jet contamination in the low- p_T region: $A_{jet} > 0.6 \pi R^2$, where A_{jet} is jet area calculated in the anti- k_T algorithm.

3. Leading Track Momentum

A minimum transverse momentum of 5 GeV/ c is applied to the jet leading track constituent to cut down the combinatorial jet contamination, which is accidentally

reconstructed by tracks from underlying event, at the cost of introducing a fragmentation bias: $p_T^{\text{lead}} > 5 \text{ GeV}/c$.

The average background energy density ρ is calculated on event-by-event basis using k_T clusters [51] (for the detail description, see section 4.5). The background is then subtracted from each anti- k_T jet as follows:

$$p_{T,\text{ch,jet}}^{\text{rec}} = p_{T,\text{ch,jet}}^{\text{raw}} - \rho \cdot A_{\text{jet}}. \quad (4.2)$$

The jet p_T distributions with different leading track p_T requirement are shown in Fig. 4.12 for four centrality classes (top), and their ratios to the $p_T^{\text{lead}} > 0.15 \text{ GeV}/c$ case (bottom). As expected, the low- p_T jet yield is suppressed up to $35 \text{ GeV}/c$ due to the leading track p_T requirement for $p_T^{\text{lead}} > 5 \text{ GeV}$ in the most central collisions, while this bias is negligible at higher p_T . Furthermore this bias decreases for peripheral collisions in which the jet fragmentation pattern become harder. Note that the leading track p_T requirement reduces not only combinatorial jets but also true jets with soft fragmentation.

Fig. 4.13 and Fig. 4.14 show $p_{T,\text{ch,jet}}^{\text{rec}} > 40 \text{ GeV}/c$ reconstructed jet ϕ and η distributions respectively. Thanks to hybrid track selection, a fluctuation of $\lesssim 20\%$ is achieved over the whole jet acceptance.

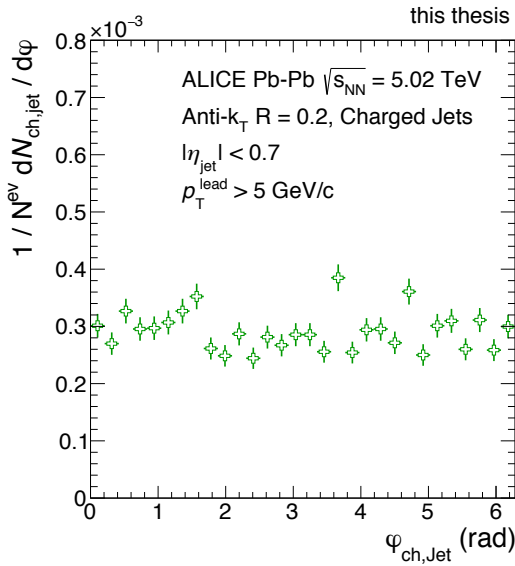


Fig 4.13: Reconstructed jet ϕ distribution with $p_{T,\text{ch,jet}}^{\text{rec}} > 40 \text{ GeV}/c$.

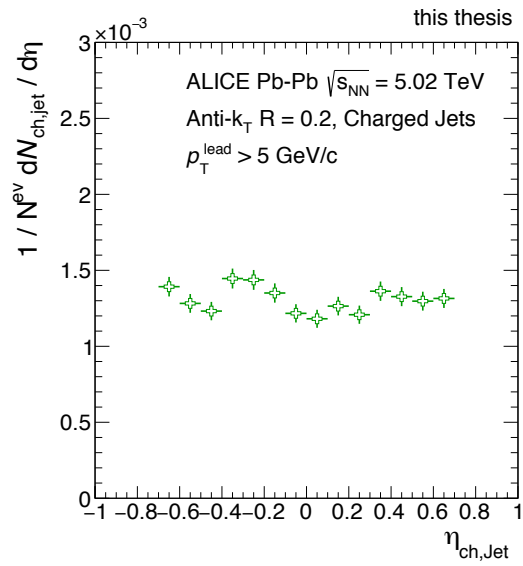


Fig 4.14: Reconstructed jet η distribution with $p_{T,\text{ch,jet}}^{\text{rec}} > 40 \text{ GeV}/c$.

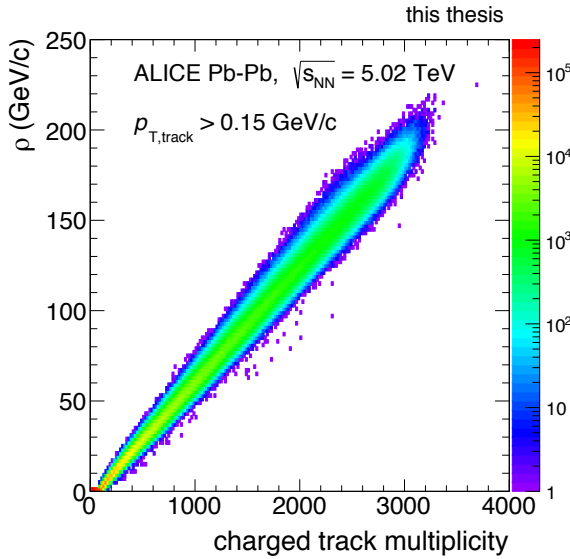


Fig 4.15: Correlation between average background density and charged track multiplicity.

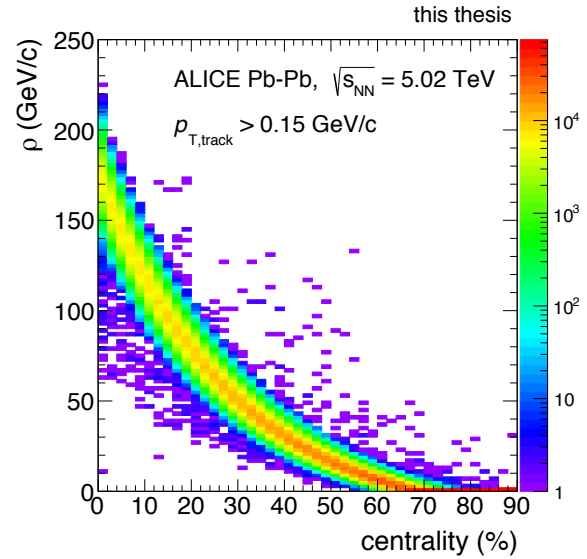


Fig 4.16: Correlation between average background density and event centrality.

4.5 Underlying Event

In high-energy heavy-ion collisions, a number of particles which do not originate from hard partons should be considered as background for the jet signal of interest. This soft background fluctuates both from event to event, but also from one location to another within the same event. As mentioned in section 4.4, the background average p_T density per unit area, ρ , is evaluated event-by-event. Local fluctuations of the background density with respect to the event median cause large uncertainty in the reconstructed jet energy. These fluctuations are quantified by known probes (random cones, single high- p_T tracks, PYTHIA jets...) into real Pb-Pb events as explained hereafter. For this local fluctuation within the same event, statistical correction of the spectrum is available utilising the distribution of residual error from average background density.

Average Underlying Event Density

The average background density (ρ) which is used to correct the jet momentum in Eq. 4.2 is estimated as follows:

1. k_T clusters are reconstructed with the FastJet k_T algorithm using hybrid tracks of

centrality	$\langle \rho \rangle$ (GeV/c)	$\langle \rho \rangle \times \pi R^2$ (GeV/c) ($R = 0.2$)
0 - 10 %	146.4	18.4
10 - 30 %	81.4	10.2
30 - 50 %	32.3	4.1
50 - 90 %	3.7	0.5

Tab 4.2: The average underlying event density.

$p_T > 0.15$ GeV/c within the ALICE acceptance ($|\eta| < 0.9$, $0 < \phi < 2\pi$), and $R = 0.2$ as resolution parameter.

- two types of k_T clusters are excluded: (i) clusters outside of the fiducial area ($|\eta_{\text{jet}}| > 0.9 - R$), and (ii) the two highest transverse momentum clusters in order to reduce the influence of true hard jets on the background estimate.
- the statistical median of the remaining cluster $p_{T,i} / A_i$ ratios is calculated and defined as background density ρ .

ρ correlation with centrality percentiles and charged track multiplicities are shown in Fig. 4.15 and Fig. 4.16 respectively. It is noticeable that the average background energy density scales linearly with track multiplicity and shows an amplitude of about 145 GeV/c in the most central collisions (0-10%) which in turn corresponds to 18 GeV/c for $R = 0.2$ jets. The mean background densities, $\langle \rho \rangle$ for four centrality classes are quoted in the Tab. 4.2.

Underlying Event Fluctuation

Region-to-region background energy fluctuations in a heavy-ion collision, δp_T , is determined by randomly placed cones (RC) of radius R as follows:

$$\delta p_T = \sum_i^{RC} p_{T,i}^{\text{track}} - \rho \pi R^2 \quad (4.3)$$

where $p_{T,i}^{\text{track}}$ is the transverse momentum of track i belonging to the RC considered. Fig. 4.17 shows the δp_T distributions for two RC definitions:

- Randomly located cones directing within fiducial area of $R = 0.2$ jet: ($|\eta^{\text{RC}}| < 0.7$).

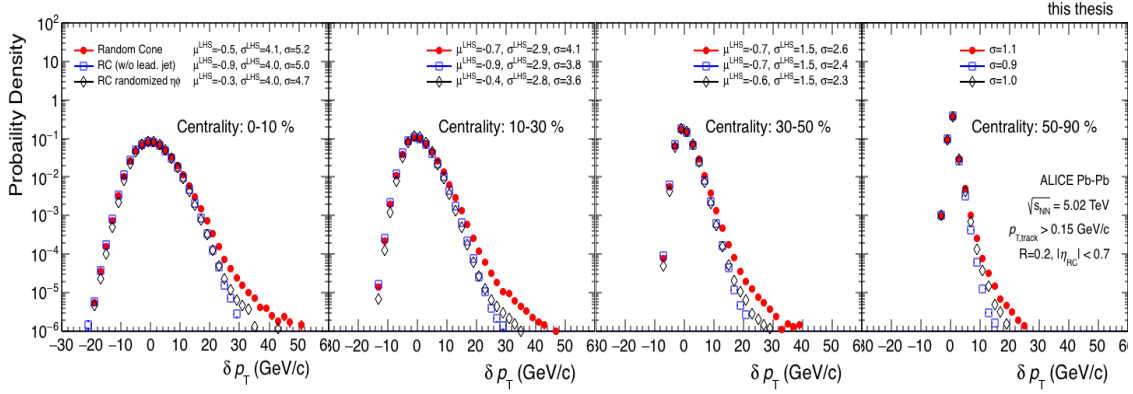


Fig 4.17: δp_T distributions for two RC selections and RC in track randomised event.

- RC is apart from the leading jet by at least 1 unit in the η - ϕ plane:

$$\Delta R = \sqrt{(\eta^{\text{RC}} - \eta^{\text{lead.jet}})^2 + (\phi^{\text{RC}} - \phi^{\text{lead.jet}})^2} > 1.$$

For comparison to purely statistical fluctuations, RC are also thrown throughout randomised events constructed from real events by cancelling particle correlations.

The right-hand-side tail of the δp_T distribution is caused by RC overlapping with the leading jet when the leading jet is not excluded while it is due to high- p_T tracks of the leading jet for randomised events. The background fluctuation is characterised by the width of the δp_T distribution: $\sigma(\delta p_T)$. The RMS of the δp_T distribution is shown as function of track multiplicity in Fig. 4.18. In addition to the RMS, the width of gaussian fit of the left-hand-side region; $[\mu^{\text{LHS}} - 3\sigma^{\text{LHS}}, \mu^{\text{LHS}} + 0.5\sigma^{\text{LHS}}]$, which is independent of the leading jet constituents, is quoted in Fig. 4.17. These results indicate that the background fluctuates within ~ 5 GeV/c around average background density for $R = 0.2$ charged jets in the most central (0-10%) collisions. As expected, a lower fluctuation is observed for peripheral collisions. The minimum p_T limit of measured jet spectrum is typically selected as $5\sigma(\delta p_T)$, in which $\sigma(\delta p_T)$ is the width of δp_T distribution. The spectrum collection is hard below this limit due to poor jet energy resolution (see section 4.7).

4.6 Jet Finding Efficiency

Similarly to tracking efficiency evaluation, jet finding efficiency is estimated from MC simulations (PYTHIA + GEANT). The generator-level jets are reconstructed from generated

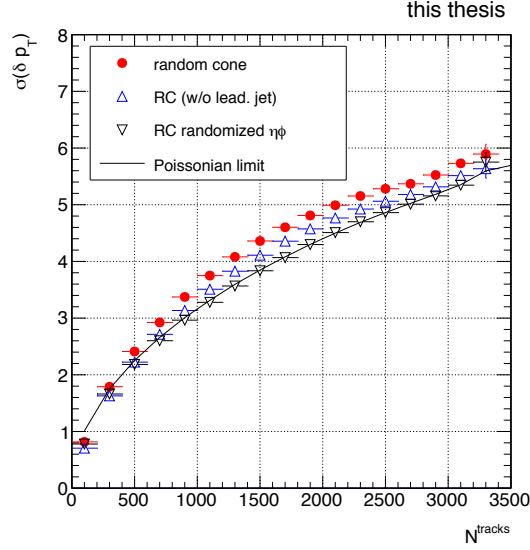


Fig 4.18: The width of δp_T distributions for two RC selections and RC in track randomised event as a function of charged particle multiplicity.

particles, while reconstruction-level jets are made from tracks smeared by the GEANT3 detector response. The jet finding efficiency is defined as the fraction of reconstruction-level jets which match with generator-level jets within $|\eta| < 0.5$ as follows:

$$\varepsilon_{\text{jet}} \left(p_{T, \text{ch jet}}^{\text{gen}} \right) = \frac{N_{\text{matched}}^{\text{rec}}}{N_{\text{gen}} (|\eta^{\text{gen}}| < 0.5)} \quad (4.4)$$

A one-to-one matching between the I -th generator-level jet and the J -th reconstruction-level jet established based on the distance in the $(\eta-\phi)$ plane $\Delta R(i, j) = \sqrt{(\eta_i^{\text{gen}} - \eta_j^{\text{rec}})^2 + (\phi_i^{\text{gen}} - \phi_j^{\text{rec}})^2}$, as follows:

1. for the index j running over all the reconstruction-level jets, find the index j' of the closest generator-level jet.
2. for the index i running over all the generator-level jets, find the index i' of the closest reconstruction-level jet.
3. $j' = J$ and $i' = I$
4. $\Delta R(I, J) < 0.1$

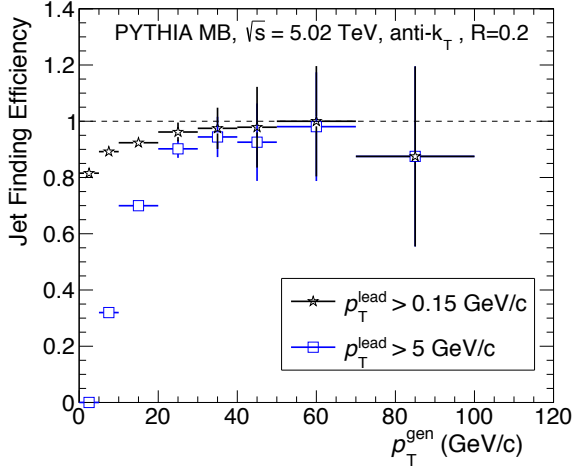


Fig 4.19: Jet finding efficiency for different p_T^{lead} requirements.

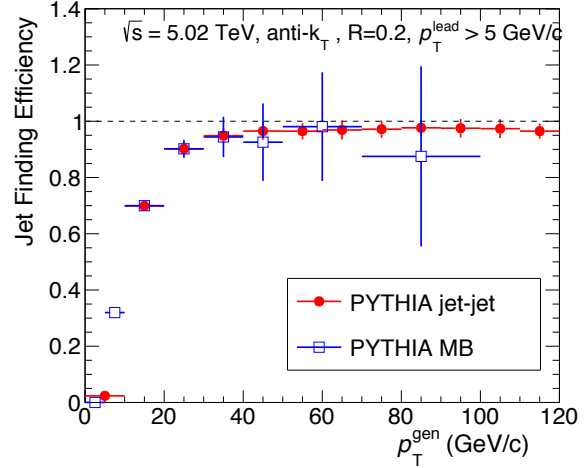


Fig 4.20: Jet finding efficiency for different event samples; PYTHIA MB and PYTHIA jet-production.

Fig. 4.19 shows the jet finding efficiency extracted from a PYTHIA MB dataset for reconstruction-level jets with/without leading track p_T cut. The leading track p_T cut decreases jet finding efficiency since the reconstructed jet doesn't have constituents with $p_T > 5 \text{ GeV}$ and/or the leading track might not be reconstructed due to tracking inefficiency. This result is cross-checked against the jet finding efficiency obtained with a PYTHIA jet production dataset (see Fig. 4.20). The results are in good agreement, so that the jet finding efficiency computed from the PYTHIA jet production sample, are more statistically precise at high- p_T , have been used.

4.7 Unfolding

The measured jet spectra are usually distorted due to finite resolution/tracking efficiency of the detector and fluctuating background especially in the most central heavy-ion collisions. An unfolding procedure [52] is performed to revert to true spectrum from the measured one based on the concept that the measured distribution is described as a convolution of distortion responses with the true one, which, more specifically, could be written as:

$$M_m = G_{md} \cdot (G_{d,t} \cdot T_t) \quad (4.5)$$

$$T_t = \left(G_{d,t}^{-1} \cdot G_{md}^{-1} \right) \cdot M_m \quad (4.6)$$

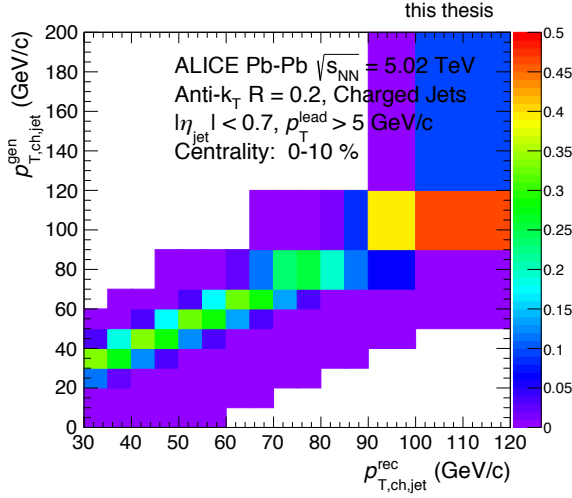


Fig 4.21: Response Matrix on background fluctuation in 0-10% centrality class.

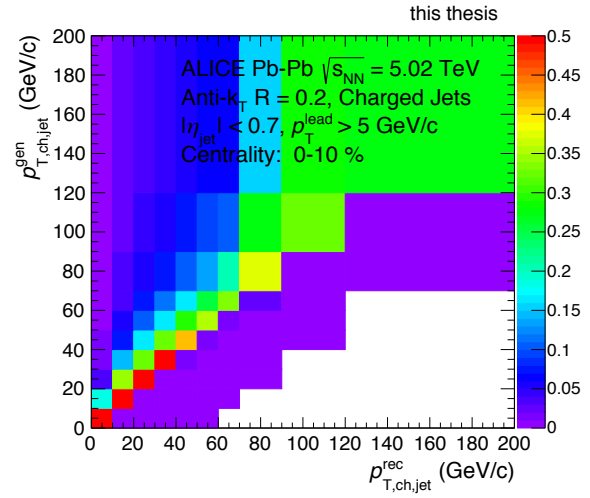


Fig 4.22: Response Matrix on detector effects in 0-10% centrality class.

where M_m is the measured spectrum, $G_{m,d}$ ($G_{d,t}$) is the distortion response from background fluctuations (detector resolution/inefficiency) and T_t is the true unknown spectrum to be extracted. $G_{m,d}$ and $G_{d,t}$ are called “Response Matrix” on account of their Matrix format. This analysis utilises the “SVD unfolding” [53] method.

On the one hand, $G_{m,d}$ (background fluctuation response) is given by the following procedure:

1. normalise the δp_T distribution given in section 4.5 to unity.
2. shift normalised δp_T distribution by the p_T^{gen} such that the diagonal elements contain the $\delta p_T = 0$ bin content (see Fig. 4.21).

On the other hand, $G_{d,t}$ (response from detector effects) is calculated using a PYTHIA MC simulation as follows:

1. remove PYTHIA tracks following the tracking efficiency defined in section 4.3.2,
2. reconstruct jets with the resulting reduced number of tracks, ,
3. match generator-level jets and jets reconstructed in step (2), using the same matching conditions as those described in section 4.6,
4. fill the response matrix with the p_T of the matched jet pairs,

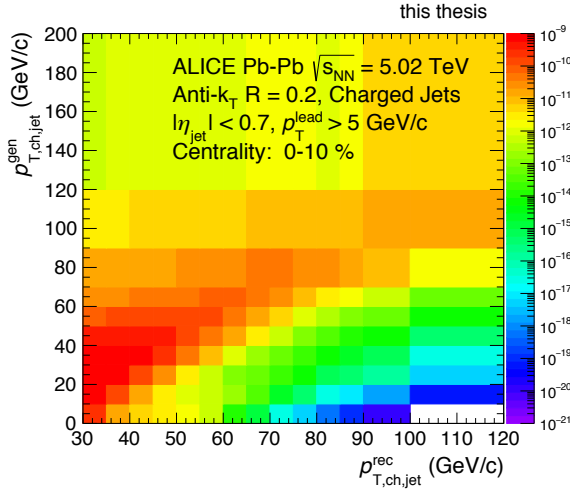


Fig 4.23: Combined Response Matrix for 0-10% centrality class.

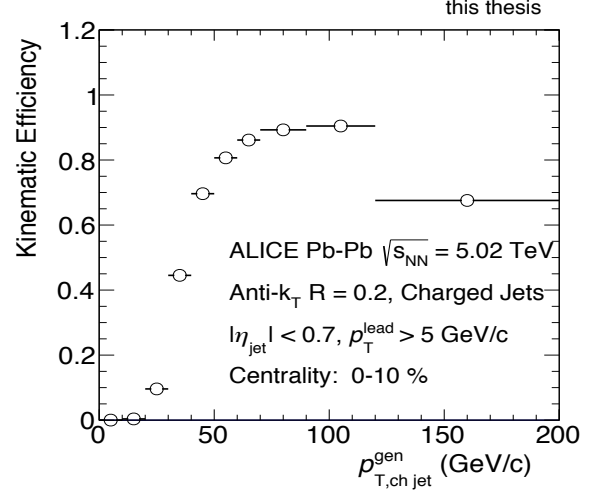


Fig 4.24: Kinematic efficiency, the jet yield fraction lays inside the selected window of combined response matrix.

5. normalise the projection on the p_T^{gen} -axis to unity. (see. Fig. 4.22)

Subsequently, $G_{m,d} \cdot G_{dt}$, called “combined response matrix” is calculated and weighted by the prior which is the base spectrum of unfolding. The generator-level jet spectrum passing step (3) of $G_{d,t}$ construction process is used as a prior. The combined response

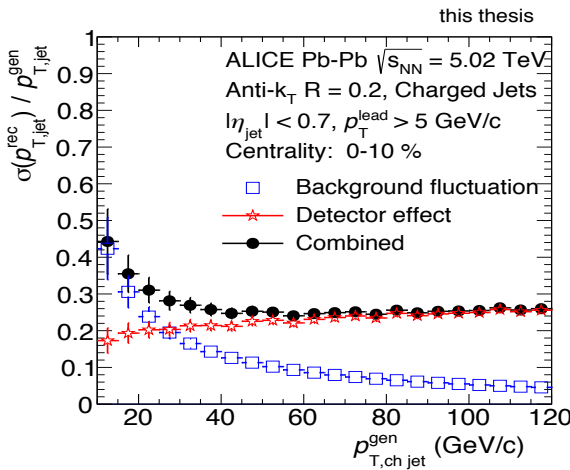


Fig 4.25: Jet momentum resolution for 0-10% centrality class.

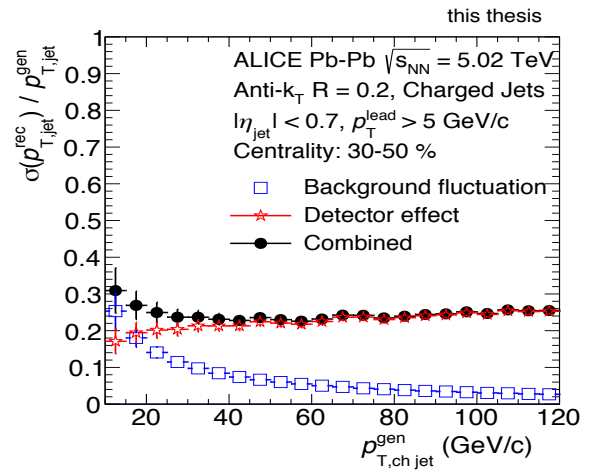


Fig 4.26: Jet momentum resolution for 30-50% centrality class.

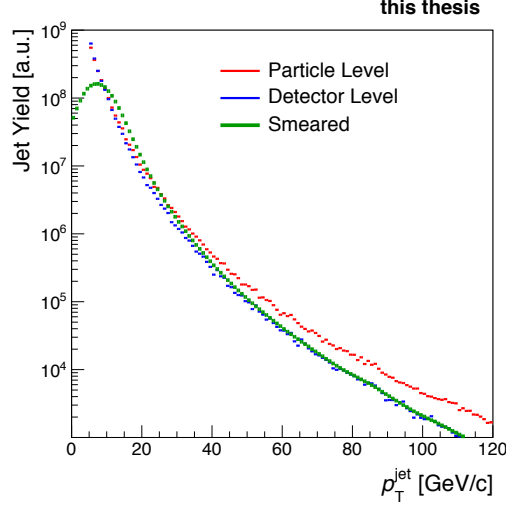


Fig 4.27: p_T distributions used for unfolding performance check; (red) PYTHIA generator-level jets, (blue) PYTHIA reconstruction-level jets, (green) and reconstruction-level spectrum after δp_T smearing.

matrix in the 0-10% centrality class is shown in Fig. 4.23. The kinematic range of the generated p_T -axis is wider than the reconstructed p_T -axis one in the combined response matrix in order to allow for feed-in into the measured p_T range. The fraction of jets which will be smeared outside the acceptance of the response matrix, is known as the kinematic efficiency (Fig. 4.24) and is taken into account in the unfolding procedure.

Fig. 4.25 and Fig. 4.26 show the jet momentum resolution in Pb-Pb collisions for the 0-10% and 30-50% centrality classes respectively. The momentum resolution is defined as $\sigma(p_{T,\text{chjet}}^{\text{rec}}) / p_{T,\text{chjet}}^{\text{gen}}$ and derived from the response matrices. The background fluctuations dominate the detector resolution at low- p_T while the opposite happens at high- p_T .

The SVD unfolding is controlled by a regularisation parameter k which can be optimised by the D-vector distribution (for the detail, see [53]). Finally, the unfolded spectra are scaled down by jet finding efficiency to compensate for jets not reconstructed.

4.7.1 Test of Unfolding Performance

The performance of unfolding is benchmarked against a known spectrum given by MC simulation. The settings of this test are listed below:

- the true jet spectrum to be recovered is the PYTHIA generator-level jet spectrum,

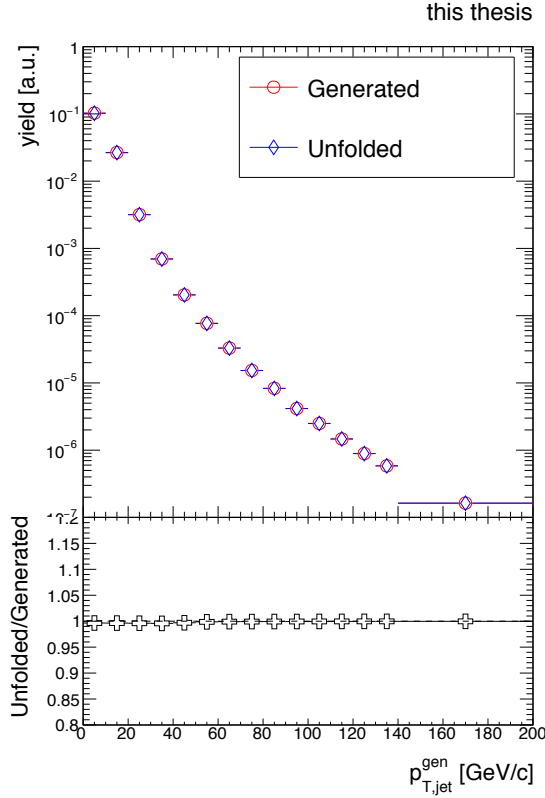


Fig 4.28: (top) Unfolded jet spectrum and generator-level jet spectrum. (bottom) The ratio of these spectra.

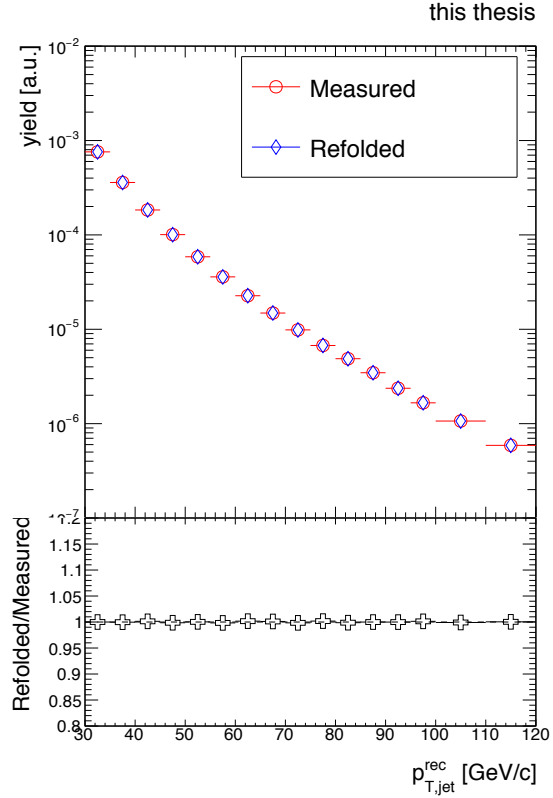


Fig 4.29: (top) Refolded jet spectrum and reconstruction-level spectrum after δp_T smearing. (bottom) The ratio of these spectra.

- the detector response is calculated from the same PYTHIA with GEANT simulation,
- background Gaussian fluctuations ($\sigma = 4 \text{ GeV}/c$) are assumed,
- the unfolding input jet spectrum is δp_T smeared PYTHIA reconstruction-level jet spectrum.

Fig.4.27 shows each input/output spectrum used in this test. The smearing by the background fluctuations changes the spectrum shape in the low- p_T region, while the detector effects are dominant at higher p_T . The unfolded and true jet spectra are shown in Fig. 4.28. Additionally, the refolded spectrum which is produced by refolding the unfolded spectrum by the same response matrix is shown in Fig. 4.29 along with the smeared input spectrum. Both results agree with a precision of $\sim 1\%$.

4.7.2 Unfolded Spectrum

The cross section of charged jet with $R = 0.2$ in Pb-Pb collisions are shown in Fig. 4.30 for four centrality classes together with the charged jet cross section in pp collisions at same centre-of-mass energy. In the next chapter, the systematic uncertainties displayed in this plot are detailed.

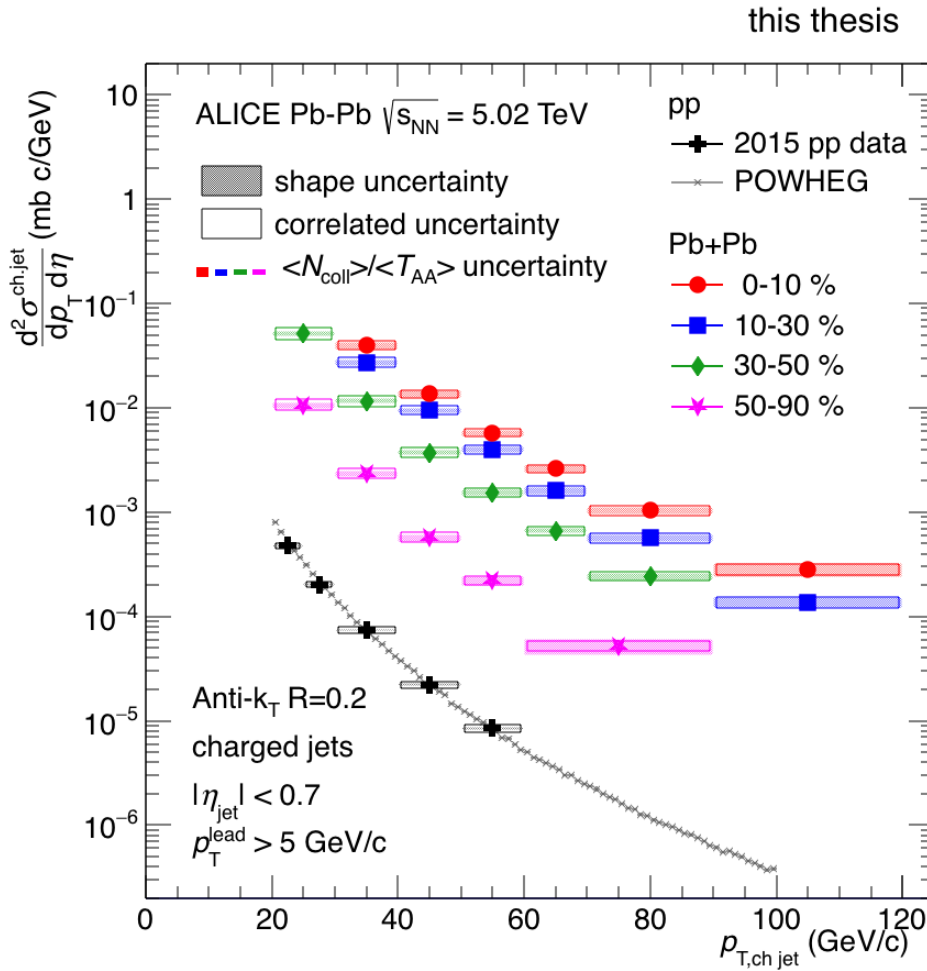


Fig 4.30: The cross section of charged jet with $R = 0.2$ in Pb-Pb and pp collisions at $\sqrt{s_{NN}} = 5.02$ TeV.

Chapter 5 Systematic Uncertainties

In this chapter, the main sources of systematic uncertainties affecting the jet spectrum measurement in Pb-Pb collisions presented in this thesis are discussed in detail and estimated. They can basically be classified into four topical groups (each group sometimes itself broken down into several uncertainties):

1. the uncertainties due to the unfolding procedure,
2. the uncertainty on the δp_T distribution evaluation,
3. the uncertainty on background p_T density due to elliptic flow,
4. the uncertainties on tracking efficiency and resolution.

5.1 Unfolding

5.1.1 p_T Range of the Unfolded Jet Spectrum

The unfolded p_T range is chosen to be much wider than the measured p_T range in order to allow bin-to-bin migration likely to occur in the unfolding process. To estimate how feed-in/out from high/low- p_T jets affect the unfolded jet spectrum, the unfolded p_T range is varied around its nominal limits by 10 GeV/ c (25 GeV/ c) at low(high) p_T . The contribution to the relative systematic uncertainty in the most central collisions is shown in Fig. 5.1. The influence of these variations are less than 2% over all centrality classes and p_T ranges.

5.1.2 p_T Range of the Measured Jet Spectrum

The measured p_T range is varied by 5 GeV/ c both on the upper and lower limits. At low- p_T , the extension of the p_T range enhances the combinatorial background despite the leading track requirement. In the high- p_T region, the influence of the limited statistics emerges. Fig. 5.2 shows the contribution of the $p_{T,\min}^{\text{rec}}$ and $p_{T,\max}^{\text{rec}}$ cut-off variations to the systematic uncertainty on the unfolded jet spectrum.

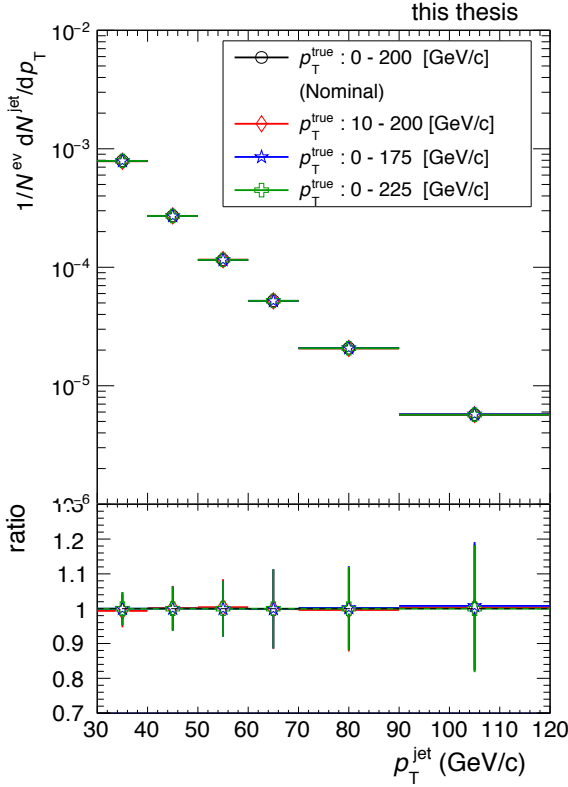


Fig 5.1: Unfolded spectra for different unfolded jet p_T range selections(top), and their deviations from nominal selection(bottom), in 0-10% centrality class.

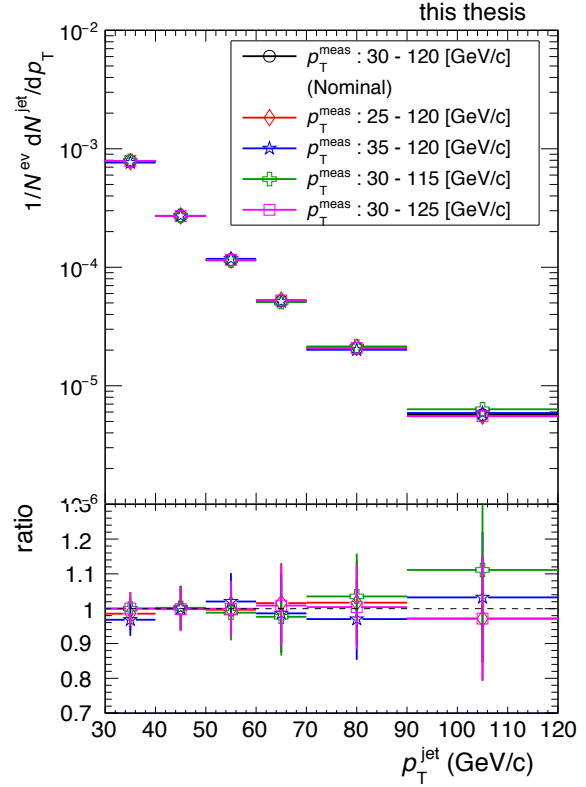


Fig 5.2: Unfolded spectra for different measured jet p_T range selections(top), and their deviations from nominal selection(bottom), in 0-10% centrality class.

5.1.3 Unfolding Method

The unfolded spectrum given by the ‘‘Bayes Unfolding’’ is compared to the result of the SVD unfolding method. In Fig. 5.3, the unfolded spectra and their ratios are shown. Deviations up to $\sim 5\%$ at low p_T are observed for the Bayesian method.

5.1.4 Unfolding Regularisation Parameter

The choice of SVD regularisation parameter k is driven by the D-vector. The regularisation parameter should be set to coincide with the critical value beyond which the d values drop to and stick around unity. In order to check that the result does not change dramatically, k is varied around the nominal value, $k \pm 1$. The corresponding variation of the jet spectrum is shown in Fig. 5.4.

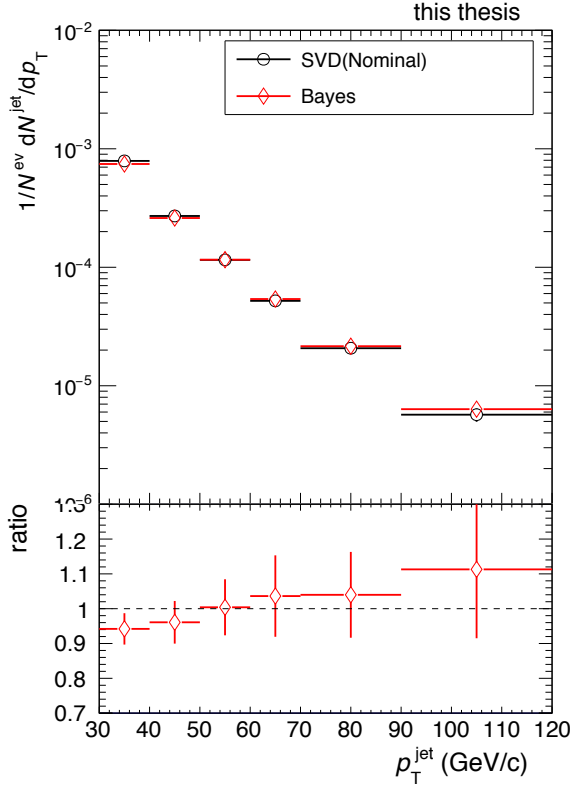


Fig 5.3: Unfolded spectra for different unfolding method selections(top), and their deviation from nominal selection(bottom), in 0-10% centrality class.

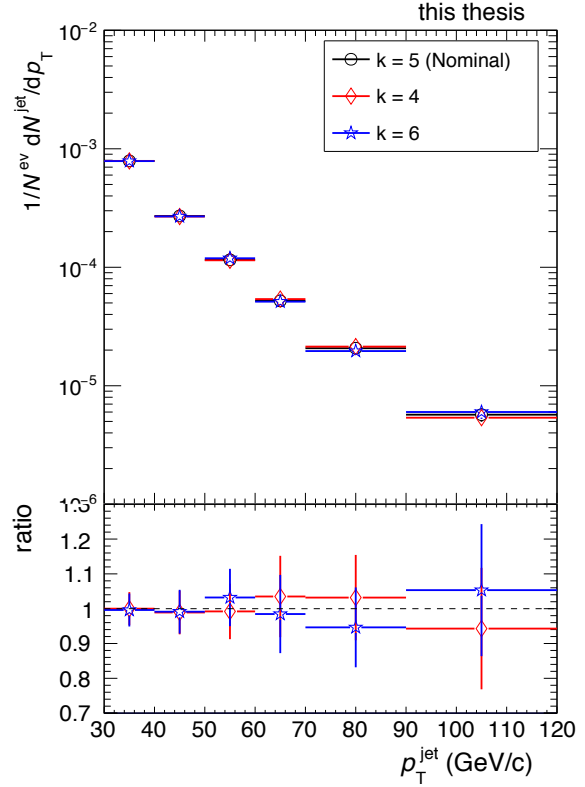


Fig 5.4: Unfolded spectra for different s regularisation parameter selections(top), and their deviations from nominal selection(bottom), in 0-10% centrality class.

5.1.5 MC Generator and Prior Selection

The uncertainty related to the choice of the MC event generator is estimated using two event generations: PYTHIA with a different tune (Perugia0) and HERWIG. The difference of the simulated jet spectrum and fragmentation between the event generators can induce differences in the jet response matrix and the prior used for the unfolding. The method to estimate this uncertainty is based on a fast simulation. We simulate PYTHIA events, extract the charged final-state particles, apply a parametrised tracking efficiency and p_T resolution particle-by-particle and use the FastJet anti-kt algorithm to cluster both the original generator-level event and the reconstruction-level event to derive the response matrix. The deviations are shown in Fig. 5.5, resulting in uncertainties of the order of 5%.

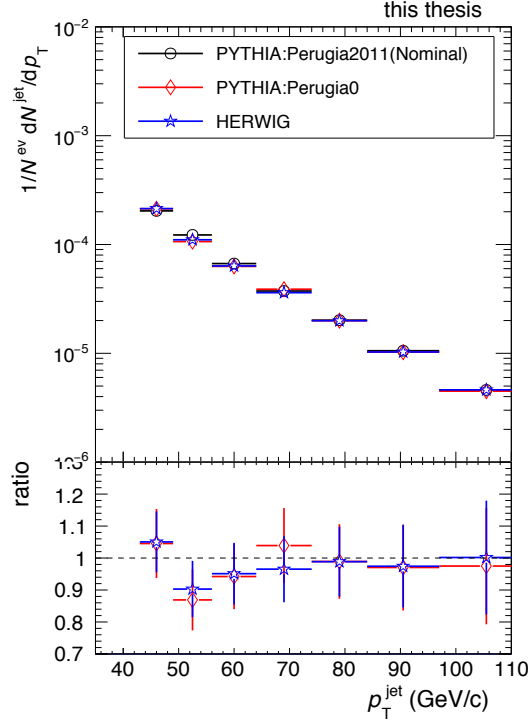


Fig 5.5: Unfolded spectra for different event generator selections(top), and their deviations from nominal selection(bottom), in 0-10% centrality class.

5.2 Background Fluctuation δp_T Estimation

Three random cone selections are used to assess the δp_T distribution variation: (i),(ii) excluding the surrounding areas defined by $\Delta R > 0.5$ and 1.5 and (iii) excluding the 1st and 2nd leading jet neighbourhood of $\Delta R > 1.0$. The resulting δp_T distribution width variation is of a few hundred MeV/c corresponding to less than 5% change of the unfolded spectrum for the most central collisions (see Fig. 5.6).

5.3 Correction for the Elliptic Flow Bias

The sample of jets selected with a leading track cut is biased by elliptic flow in heavy-ion collisions. The azimuthal dependence with respect to the leading track in the event of the mean background density departure from the nominal value (full azimuth) is shown in Fig. 5.7. The azimuthal regions are defined as:

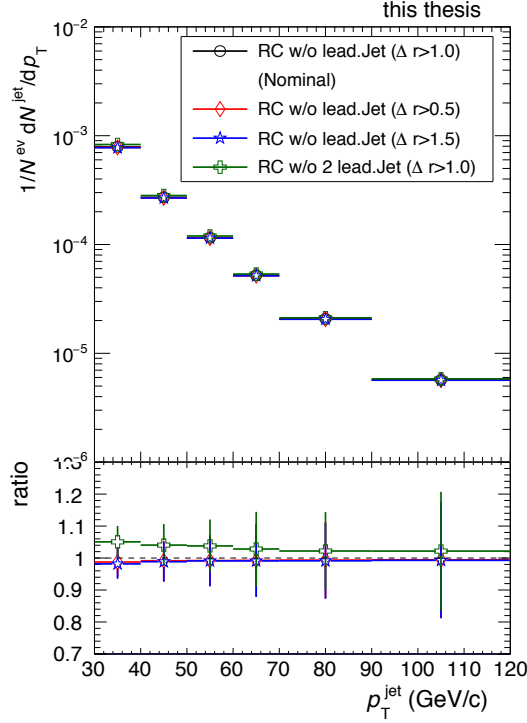


Fig 5.6: Unfolded spectra for different δp_T definitions(top), and their deviations from nominal value(bottom), in 0-10% centrality class.

$$\left| \phi_{\text{leading track}} - \phi_{k_T \text{ cluster}} \right| = \begin{cases} [0, \pi/4 - R] & : \text{near side} \\ [\pi/4 + R, 3\pi/4 - R] & : \text{perpendicular} \\ [3\pi/4 + R, \pi] & : \text{away side} \end{cases}$$

The difference of the azimuthal background density to the mean background density in the full event is $4 \text{ GeV}/c$ in the 0-10% centrality class. The uncertainty on the background density due to the flow bias is estimated by shifting the δp_T distribution by $\pm 4 \pi R^2 \text{ GeV}/c$. Since the upper and lower variations of the background density due to flow are symmetric with respect to the nominal value, the systematic uncertainty is also symmetric as seen in Fig. 5.8. The uncertainty due to the flow bias decreases with $p_{T,\text{jet}}$, from 7% at $p_{T,\text{jet}} = 40 \text{ GeV}/c$ to 4% at $p_{T,\text{jet}} = 100 \text{ GeV}/c$.

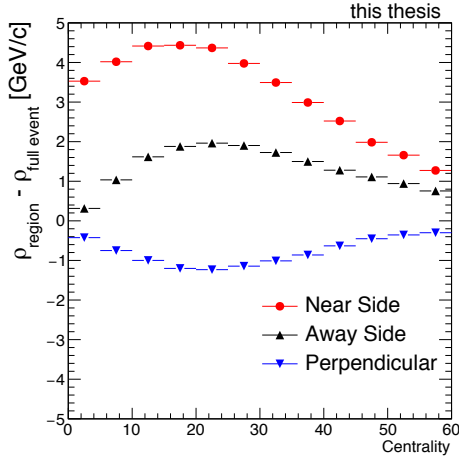


Fig 5.7: The azimuthal dependence with respect to the event leading track of average background density deviation from the nominal (full azimuth) value.

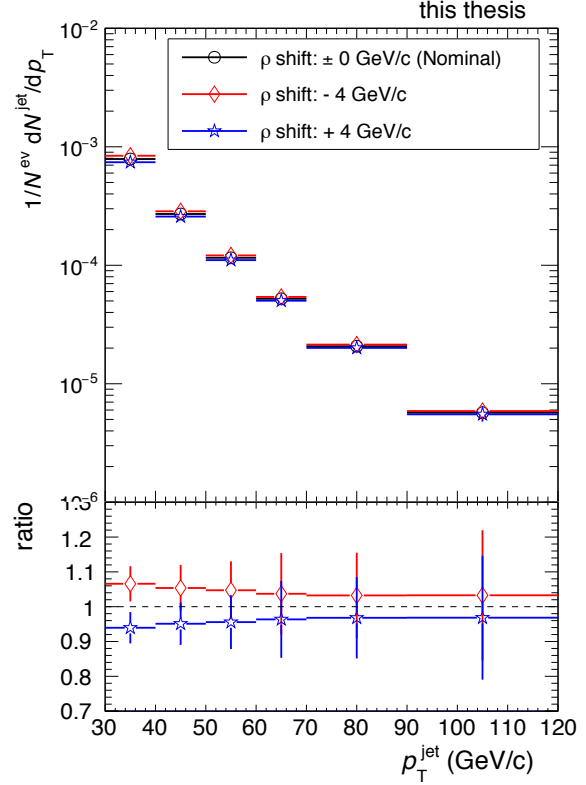


Fig 5.8: Unfolded spectra for different average background densities due to flow bias(top), and their deviations from nominal value(bottom), in 0-10% centrality class.

5.4 Tracking Efficiency and Resolution

The uncertainty on the tracking efficiency is estimated to be 4% based on the track cut parameters which are applied during track reconstruction, see Fig. 5.9. New detector response matrices are built using a fast simulation including a tracking efficiency variation of $\pm 4\%$ around the default efficiency. The PYTHIA jet spectrum smeared by the nominal combined response matrix is unfolded using these variations. The difference between the nominal unfolded solution and the unfolded spectra with modified tracking efficiencies gives $\sim 10\%$ systematic uncertainty on the unfolded yield at $p_{T,\text{jet}} = 100 \text{ GeV}/c$.

Furthermore, the uncertainty related to momentum resolution with much larger variation ($\pm 20\%$) gives a $\sim 5\%$ deviation as shown in Fig. 5.10.

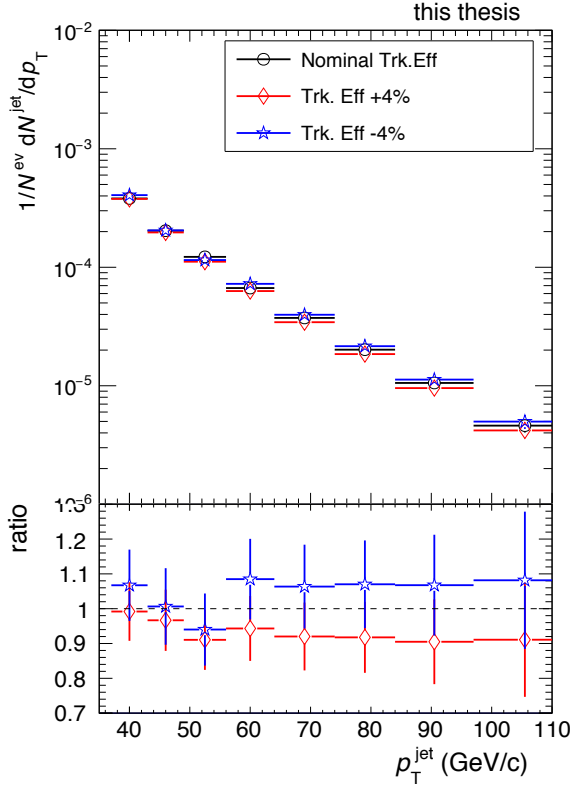


Fig 5.9: Unfolded spectra for different tracking efficiency estimation(top), and their deviations from nominal value(bottom), in 0-10% centrality class.

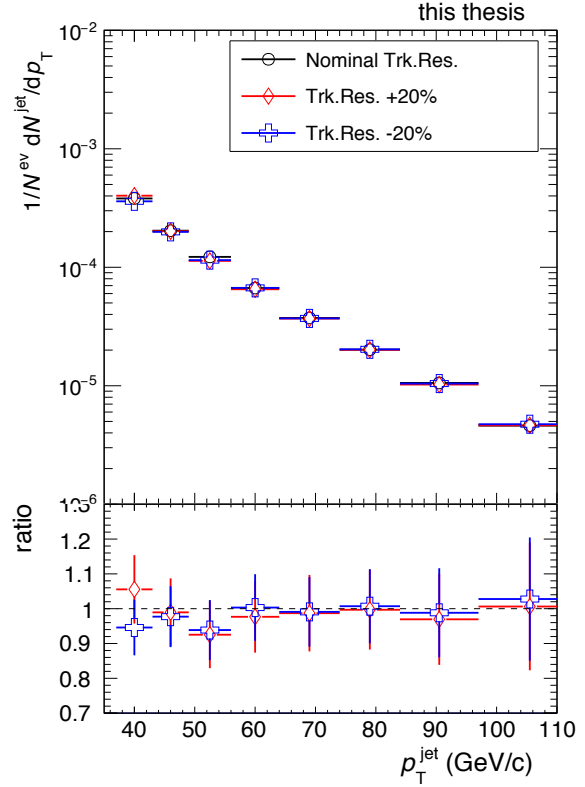


Fig 5.10: Unfolded spectra for different track momentum resolution(top), and their deviations from nominal value(bottom), in 0-10% centrality class.

5.5 Summary of Systematic Uncertainties

In Tab. 5.1 and Tab. 5.2 the breakdown of the present systematic uncertainties for three jet p_T bins are quoted. The final jet cross-section measurement incorporates systematic uncertainties divided into two categories: (i) Spectrum shape uncertainties and (ii) Correlated uncertainties. The shape uncertainties are anti-correlated or less correlated between bins of the unfolded spectrum: if the yield increases in some bins, it concomitantly decreases in the other bins or are not correlated. The correlated uncertainty, for their part, result in correlated changes over the entire spectrum which means that the spectrum shape is almost conserved.

Contributions to the spectrum shape systematic uncertainties include regularisation parameter, p_T range of the unfolded jet spectrum, p_T range of the measured jet spectrum,

the unfolding method, and the choice of the generator. The uncertainties are added in quadrature to calculate the total systematic uncertainty.

Correlated uncertainties originate from the uncertainty on the knowledge of the tracking efficiency and resolution, the correction for the flow bias and the background fluctuation δp_T estimation. These contributions are also added quadratically.

In the same tables, the shape and correlated systematic uncertainties are reported.

$p_{T,\text{ch,jet}}$	30 - 40 GeV/ c	50 - 60 GeV/ c	70 - 90 GeV/ c
p_T range unfolded	± 1.0	± 1.0	± 1.0
p_T range measured	± 2.9	± 1.2	± 3.7
Unfolding method	± 4.4	± 4.4	± 4.4
Regularisation	± 0.4	± 2.4	± 4.8
Generator/Prior	± 5.7	± 5.7	± 5.7
Total shape uncertainty	± 7.8	± 7.7	± 9.5
δp_T	+5.1 -1.8	+3.8 -0.9	+2.2 -0.9
Flow bias	+6.6 -6.1	+4.7 -4.4	+3.2 -3.2
Tracking efficiency	± 5.3	± 6.8	± 8.6
Tracking resolution	± 3.4	± 3.4	± 3.4
Total correlated uncertainty	+10.4 -8.9	+9.7 -8.8	+10.0 -9.8

Tab 5.1: Systematic uncertainties for 0 - 10%

$p_{T,\text{ch,jet}}$	20 - 30 GeV/ c	40 - 50 GeV/ c	60 - 70 GeV/ c
p_T range unfolded	± 0.5	± 0.5	± 0.5
p_T range measured	± 2.6	± 0.8	± 2.4
Unfolding method	± 1.2	± 1.2	± 1.2
Regularisation	± 0.2	± 1.3	± 2.4
Generator/Prior	± 5.9	± 5.9	± 5.9
Total shape uncertainty	± 6.5	± 6.2	± 6.9
δp_T	+5.0 -1.3	+2.5 -0.8	+1.9 -0.6
Flow bias	+9.0 -8.1	+5.4 -5.1	+4.2 -4.2
Tracking efficiency	± 8.9	± 8.5	± 8.1
Tracking resolution	± 3.4	± 3.4	± 3.4
Total correlated uncertainty	+14.0 -12.6	+10.9 -10.5	+9.9 -9.7

Tab 5.2: Systematic uncertainties for 30 - 50%

Chapter 6 Results and Discussion

In this chapter, the jet cross sections and the corresponding nuclear modification factors are presented. These results will be compared with single particle measurements or jet measurements at lower collision energy for systematic understanding of parton energy loss in the QGP. To go further in the study of parton energy loss, the jet energy loss is extracted from the results of this work. The jet energy loss, which is the more direct observable of parton energy loss, helps to assess the relative contributions of the two energy loss mechanisms, gluon radiation (radiative energy loss) and multiple parton scattering (collisional energy loss).

6.1 Jet Suppression

To estimate jet quenching in heavy-ion collisions, the jet nuclear modification factor is calculated as the ratio of charged jet spectrum in heavy-ion collisions to that of pp collisions, normalised by the number of binary collisions:

$$\langle N_{\text{coll}} \rangle = \langle T_{\text{AA}} \rangle \times \sigma_{\text{inel}}^{\text{AA}} \quad (6.1)$$

$$R_{\text{AA}} = \frac{d^2 \sigma_{\text{ch,jet}}^{\text{AA}} / dp_{\text{T}} d\eta}{\langle N_{\text{coll}} \rangle d^2 \sigma_{\text{ch,jet}}^{\text{pp}} / dp_{\text{T}} d\eta} \quad (6.2)$$

$$= \frac{1/N^{\text{ev}} d^2 N_{\text{ch,jet}}^{\text{AA}} / dp_{\text{T}} d\eta}{\langle T_{\text{AA}} \rangle d^2 \sigma_{\text{ch,jet}}^{\text{pp}} / dp_{\text{T}} d\eta}, \quad (6.3)$$

where $\langle T_{\text{AA}} \rangle$ and $\langle N_{\text{coll}} \rangle$ are respectively the nuclear overlap function and the number of binary collisions given by the Glauber model. The nuclear overlap function, number of participants, and number of binary collisions are reported in Tab. 6.1 for the considered centrality classes (and the corresponding impact parameter b).

Fig. 6.1 shows the charged jet spectra after the normalisation by $\langle T_{\text{AA}} \rangle$. As pp reference for the R_{AA} calculation, the experimental data collected in 2015 by ALICE are used [33]. The statistics of these data is about 25M events, and the kinematic reach of the jet spectrum is up to $\sim 60 \text{ GeV}/c$. In order to extend the kinematic reach of R_{AA} measurement, the

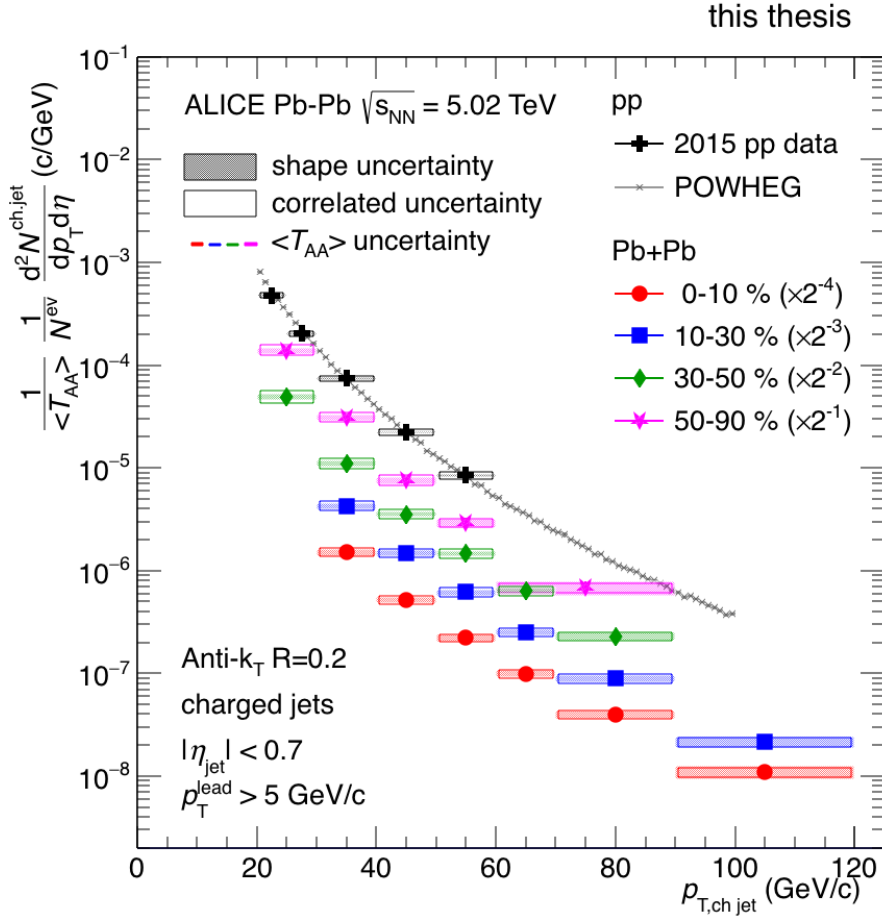


Fig 6.1: Charged jet spectra in Pb-Pb collisions after the normalisation by the number of binary collisions. As a pp reference, the spectrum measured with $\sqrt{s} = 5.02$ TeV pp run and corresponding simulation result are shown.

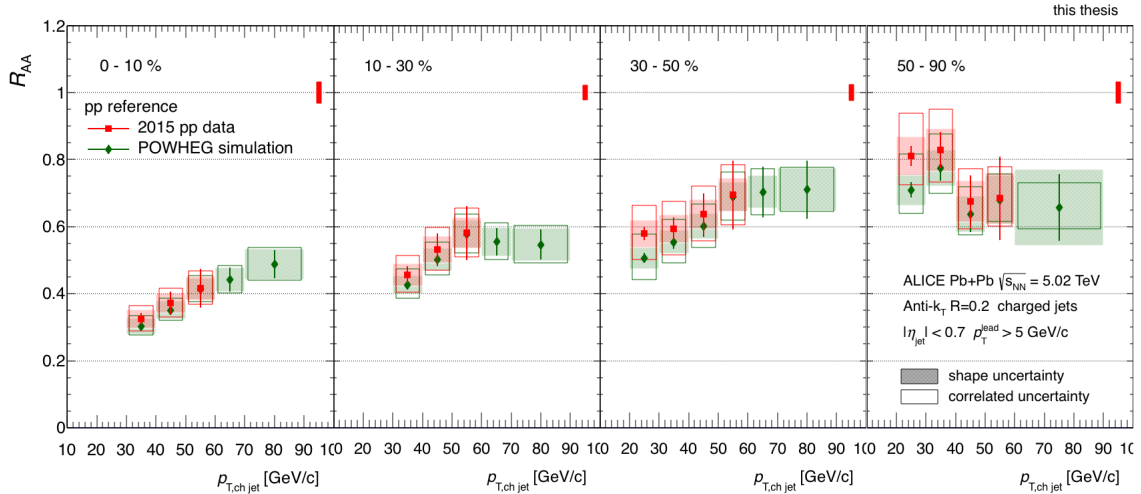
spectrum given by the POWHEG MC event generator [54], which is based on next-to-leading-order QCD calculations, is adopted as an additional pp reference. pp data and the POWHEG predictions are in good agreement as it can be seen in Fig. 6.1.

Fig. 6.2 shows the charged jet R_{AA} for Pb-Pb collisions at $\sqrt{s_{NN}} = 5.02$ TeV for four centrality classes, in which the shaded and open boxes represent the shape and correlated systematic uncertainties respectively. In addition, the red bars at upper-right in the figures

centrality	b_{\min} (fm)	b_{\max} (fm)	$\langle N_{\text{coll}} \rangle$	$\langle N_{\text{part}} \rangle$	$\langle T_{\text{AA}} \rangle$
0-10%	0	4.96	1636.0 ± 170.0	359.0 ± 3.0	23.4 ± 0.9
10-30%	4.96	8.59	801.0 ± 55.5	225.5 ± 2.3	11.4 ± 0.4
30-50%	8.59	11.1	263.5 ± 16.1	108.8 ± 1.4	3.8 ± 0.2
50-90%	11.1	15	38.1 ± 1.6	26.8 ± 0.4	0.54 ± 0.02

Tab 6.1: Geometrical parameters obtained from Glauber model.

are the uncertainties from the $\langle T_{\text{AA}} \rangle$ scaling. A strong jet suppression of $R_{\text{AA}} \sim 0.4$ is observed in the most central events, while for peripheral collisions the suppression is weaker, $R_{\text{AA}} \sim 0.8$. This suppression in central heavy-ion collisions indicates that the full jet energy is not contained in the reconstructed jets ($R = 0.2$). This is consistent with a scenario in which gluons are radiated out-of-cone due to the parton interaction with the dense medium which results in a decrease of jet- p_{T} . Another reason for a jet nuclear modification factor lower than unity, could also be that some jets cannot be resolved anymore or melt in the

Fig 6.2: Charged jet nuclear modification factors of $R = 0.2$ in Pb-Pb collisions at $\sqrt{s_{\text{NN}}} = 5.02$ TeV.

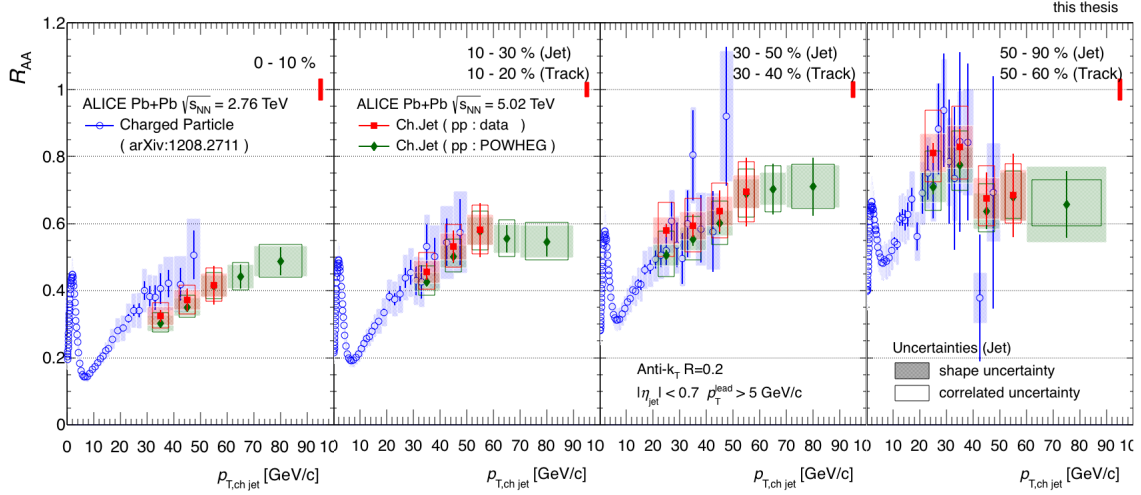


Fig 6.3: Comparison of nuclear modification factor between charged particles at $\sqrt{s_{\text{NN}}} = 2.76$ TeV and charged jets at $\sqrt{s_{\text{NN}}} = 5.02$ TeV.

background. A R_{AA} rise as function of p_{T} is observed in the low- p_{T} region, while at high- p_{T} gently increases or reaches a constant value.

6.2 Comparison to Charged Hadrons

In Fig. 6.3 the jet nuclear modification factor is compared to the single particle nuclear modification factor at $\sqrt{s_{\text{NN}}} = 2.76$ TeV measured by ALICE [55]. Note that the p_{T} scale, centrality bins and centre-of-mass energy of both measurements are different even if the recent results from the ALICE collaboration show no significant difference between charged particle R_{AA} in Pb-Pb collisions at $\sqrt{s_{\text{NN}}} = 2.76$ and 5.02 TeV [56].

A single charged particle and a jet of the same p_{T} originate from different parton energies. Naively one expects that the jet catches some or all of the radiated energy resulting in a larger nuclear modification factor for jets compared to the nuclear modification factor for charged particles. For both measurements, the expected R_{AA} high- p_{T} reach is similar if the proper upscaling of single particle p_{T} is applied. For charged jets fragmenting in the vacuum, the high p_{T} leading particle carries about 50% of the corresponding jet p_{T} . The high- p_{T} region observed in the single particle suppression approximately corresponds to

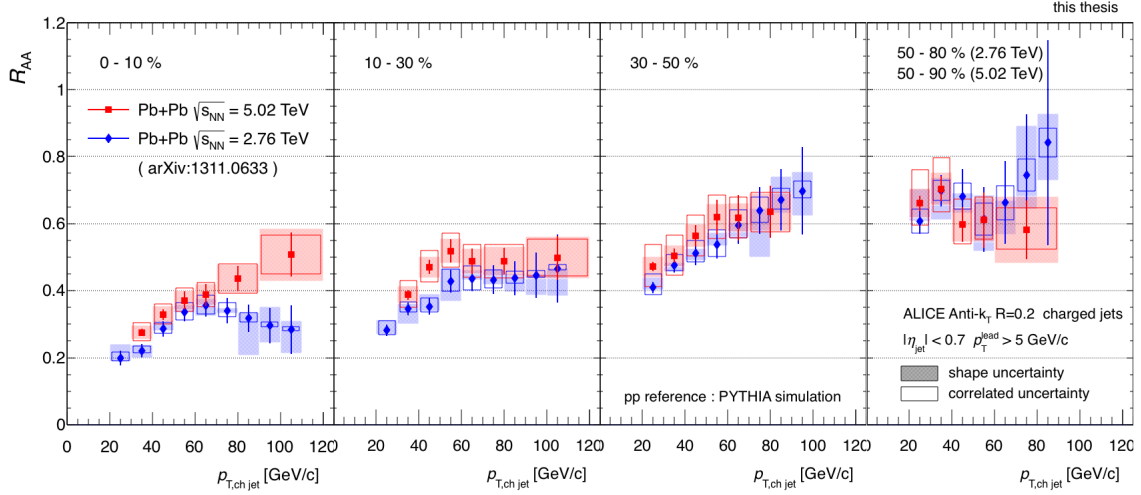


Fig 6.4: Comparison of charged jet nuclear modification factor between $\sqrt{s_{NN}} = 2.76$ TeV and $\sqrt{s_{NN}} = 5.02$ TeV .

$2 \times p_T^{\text{track}}$. The suppression for both high- p_T observables at approximately the same parton energies is consistent even though different centre-of-mass energies are considered.

6.3 Comparison to the Jet R_{AA} in Pb-Pb Collisions at $\sqrt{s_{NN}} = 2.76$ TeV

The ALICE measurement of charged jet nuclear modification factor in Pb-Pb collisions at $\sqrt{s_{NN}} = 5.02$ TeV is compared to that at $\sqrt{s_{NN}} = 2.76$ TeV in Fig. 6.4 [57]. The PYTHIA charged jet spectrum is adopted as pp reference due to the lack of charged jet measurement in pp collisions at $\sqrt{s_{NN}} = 2.76$ TeV. The jet suppression in Pb-Pb collisions at $\sqrt{s_{NN}} = 2.76$ TeV is comparable to that at $\sqrt{s_{NN}} = 5.02$ TeV within systematic uncertainties except for the high- p_T region in the most central collision. As an aside, the same comparison reported by ATLAS with $R = 0.4$ calorimetric jets at higher- p_T is given in Fig. 6.5. A similar magnitude of jet suppression for the two collision energies is observed.

The magnitude of jet suppression is expected to be stronger in higher centre-of-mass energy since heavy-ion collisions of higher centre-of-mass energy produce hotter/denser and longer-lived medium, causing larger parton energy loss. Concomitantly, the increase of collision energy results in a hardening of the jet spectrum shape, which enhances the

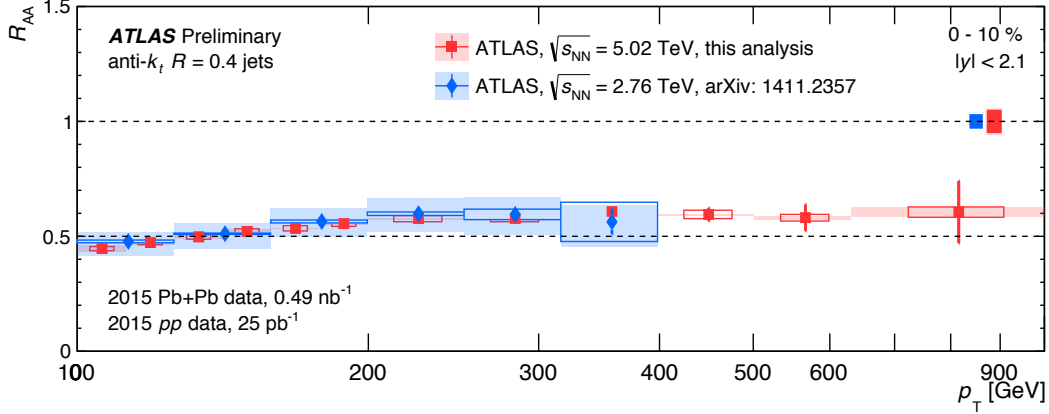


Fig 6.5: Comparison of nuclear modification factor of jets with $R = 0.4$ measured by ATLAS between $\sqrt{s_{\text{NN}}} = 2.76$ TeV and $\sqrt{s_{\text{NN}}} = 5.02$ TeV. [58]

nuclear modification factor.

Thus, the consistent R_{AA} measurements despite the increase of energy can be interpreted as a cancellation between these two effects. In order to quantify each contributions, a direct measurement of jet energy loss is performed.

6.4 Jet Energy Loss Toy Models

The jet energy loss is defined as the difference between the pp and Pb-Pb spectra of same yields. This definition is based on the hypothesis that the jet yield at a given jet momentum in heavy-ion collisions comes from the overlay of pp collisions with the same total yield. Note, however, that the actual jet yield at a certain p_{T} is a convolution of the different parton energies.

Three simple energy loss scenarios are considered in this analysis:

1. The jet energy loss is independent to jet p_{T} .
2. The jet energy loss is proportional to jet p_{T} .
3. A certain fraction of jets disappear.

Since the pp reference spectrum doesn't suffer from energy loss, the PYTHIA charged jet spectrum is used. The spectrum is fitted with a Tsallis function [59] in the $m_0 \rightarrow 0$ limit

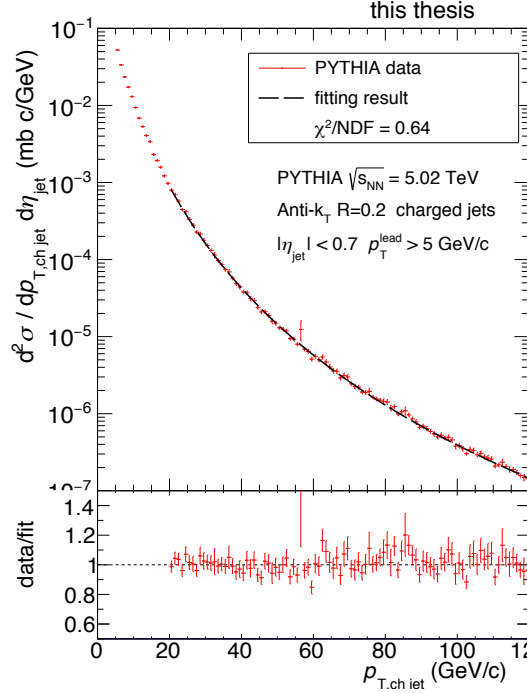


Fig 6.6: (top) PYTHIA Charged jet spectrum given by PYTHIA. The black line is Tsallis fitting result. (bottom) The ratio of data to fitting function.

as:

$$\frac{d^2\sigma}{dp_T d\eta} = p_T A \frac{(n-1)(n-2)}{(nC)^2} \left[1 + \frac{p_T}{nC} \right]^{-n}. \quad (6.4)$$

where A , n and C are the fitting parameters. The fit shown in Fig. 6.6 performs well down to ~ 20 GeV/c due to small χ^2/NDF value of 0.64.

The spectra in Pb-Pb collisions are also fitted by the same function, in which p_T is substituted with $p_T + \Delta$ for the scenario 1, or $p_T/(1-f)$ for the scenario 2, and for the scenario 3, A is substituted with $A/(1-r)$, where Δ , f and r are respectively the jet energy loss, the lost energy fraction and the disappeared jet fraction. The parameters A , C and n given by the reference spectrum fitting are set for these fittings. The fitting results for these scenarios in 0-10% centrality are shown in Fig. 6.7 and extracted Δ , f and r values are summarised in Tab. 6.2 with the fitting χ^2 values.

The R_{AA} distributions extracted from the fitting functions are shown in Fig. 6.8, Fig. 6.9

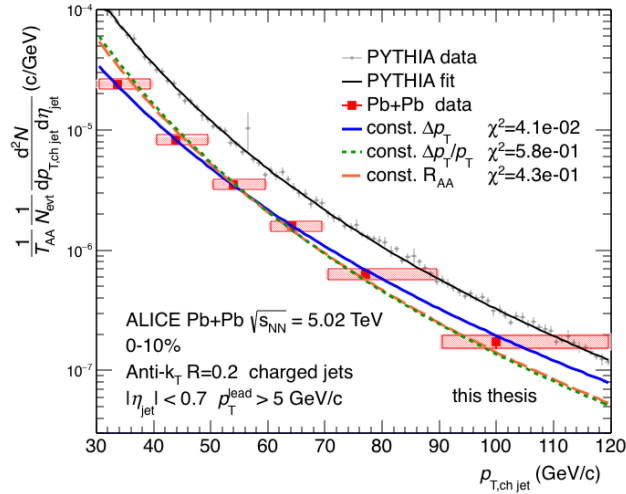


Fig 6.7: Comparison of spectrum fitting from three energy loss models, in 0-10 % centrality class.

and Fig. 6.10 for the three jet energy loss models. The model 1, which assumes a constant energy loss, is in better agreement with data than the other models as shown in smaller χ^2 value, particularly in the low- p_T region. Therefore, a constant jet energy loss is adopted for the following sections.

	0-10%	
	value	fitting χ^2
jet energy loss, Δ (GeV/c)	$9.9^{+1.6}_{-1.5}$	4.1×10^{-2}
lost energy fraction, f (%)	$14.7^{+2.6}_{-2.1}$	5.8×10^{-1}
disappeared jet fraction (%)	$56.3^{+6.4}_{-5.9}$	4.3×10^{-1}
	30-50%	
	value	fitting χ^2
jet energy loss, Δ (GeV/c)	$4.2^{+1.5}_{-1.3}$	4.2×10^{-2}
lost energy fraction, f (%)	$7.2^{+2.8}_{-2.3}$	3.7×10^{-1}
disappeared jet fraction (%)	$32.0^{+9.9}_{-9.0}$	3.0×10^{-1}

Tab 6.2: Estimated value of spectrum fitting from three jet energy loss models.

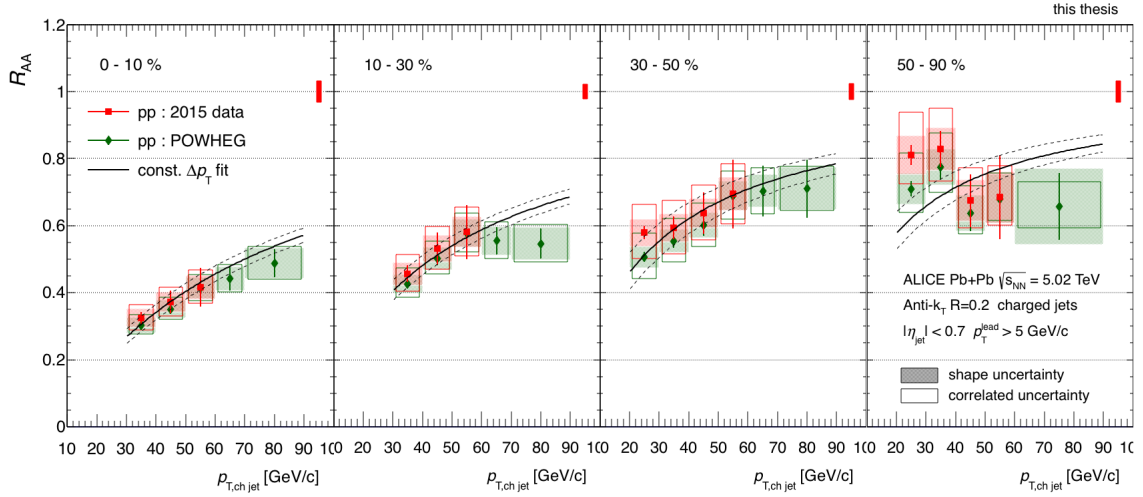


Fig 6.8: Comparison of charged jet nuclear modification with constant energy loss model (black line).

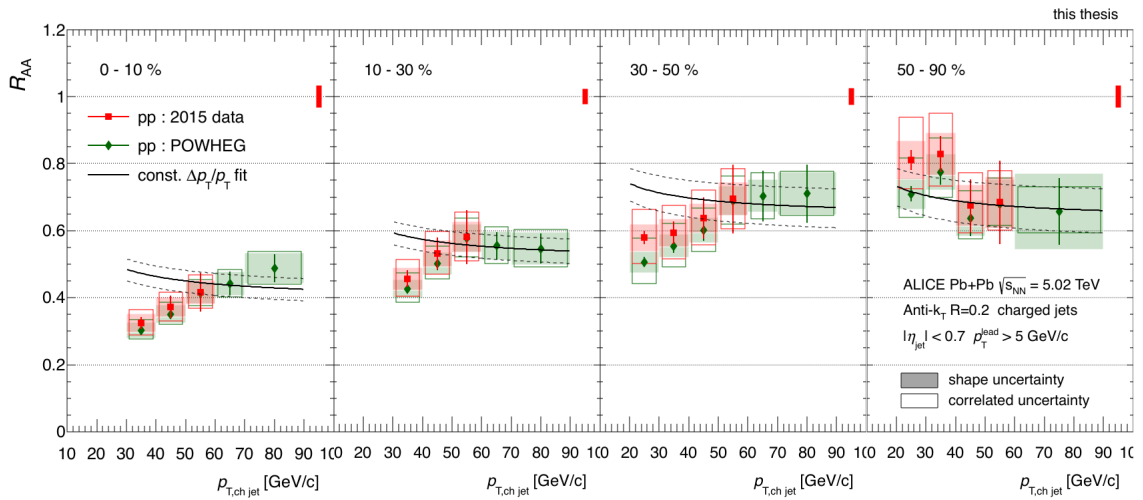


Fig 6.9: Comparison of charged jet nuclear modification with fractional energy loss model (black line).

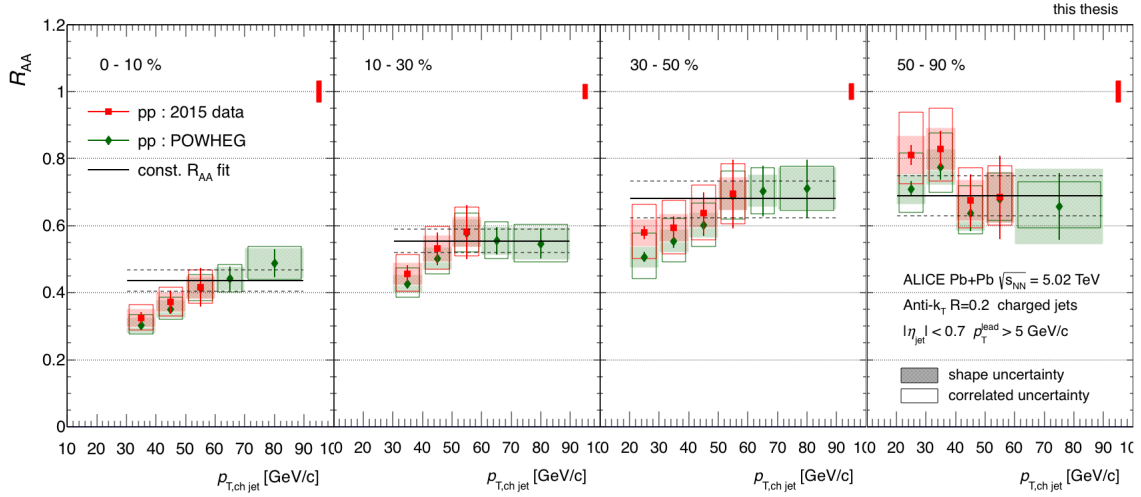


Fig 6.10: Comparison of charged jet nuclear modification with jet disappearance model (black line).

6.4.1 Path Length Dependence

The jet energy loss strongly depends on the parton path length in the QGP. The observed strong jet suppression (presented in section 6.1) results from long parton path lengths throughout the large size system produced in the most central collisions. Therefore, for better understanding the study of jet energy loss as a function of parton path length is of crucial importance. However, the observed inclusive jet spectrum is the result of the superimposition of all possible parton paths (see Fig. 6.11). The corresponding parton path length should then be averaged over all possible paths.

In the following, the average path length will be estimated from the Glauber model. The relation between the impact parameter and the estimated average parton path length is shown in Fig. 6.12. Using this relation, the centrality is converted to an average path length.

Fig. 6.13 and Fig. 6.14 show the jet energy loss as a function of parton path length, fitted with a linear and quadratic function respectively. The χ^2 for the linear function fit is 3.2×10^{-1} and for the quadratic function is 6.0×10^{-4} . Radiative energy loss is then supposed to be responsible of the measured Δp_T distribution since it is known (from QCD calculations, see section 1.3.1) to be proportional to the square of the path length.

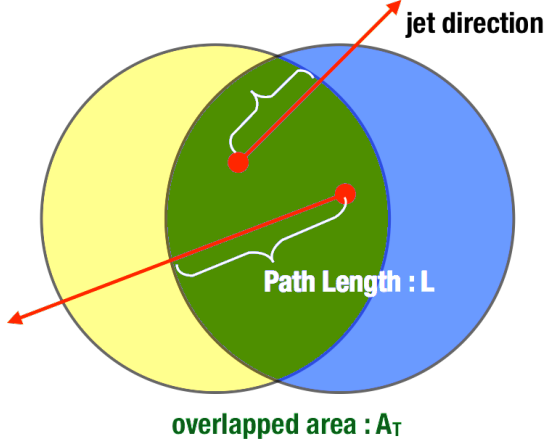


Fig 6.11: The sketch of heavy-ion collision in transverse plane. The average parton path length and overlapped area are estimated by toy model calculation.

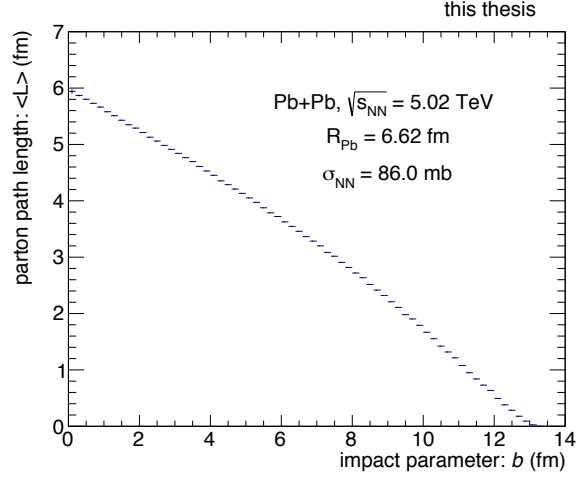


Fig 6.12: The estimated average parton path length as a function of collision impact parameter b .

6.4.2 Centre-of-Mass Energy Dependence

As the nucleus-nucleus collision centre-of-mass energy increases, the produced QGP reaches higher energy/particle densities and the system stays longer in the QGP phase. Since the parton energy loss is correlated with gluon densities and therefore to charged particle multiplicities ($\Delta E_{\text{loss}} \propto dN_g/d\eta \propto dN_{\text{ch}}/d\eta$), it is worth evaluating jet energy loss as a function of $dN_{\text{ch}}/d\eta$.

Fig. 6.15 shows the jet energy loss as a function of charged particle multiplicity per unit transverse area, A_T , for three centre-of-mass energies [57, 60]. A_T is the overlapped area of two incoming nuclei and can be estimated by the Glauber model (see Fig. 6.11). The charged particle multiplicities are given by [61, 62, 63]. There is a significant increase of energy at the LHC compared to RHIC (Au-Au collisions at $\sqrt{s_{\text{NN}}} = 200 \text{ GeV}$), such that a denser QGP is expected to be produced resulting in much larger energy loss.

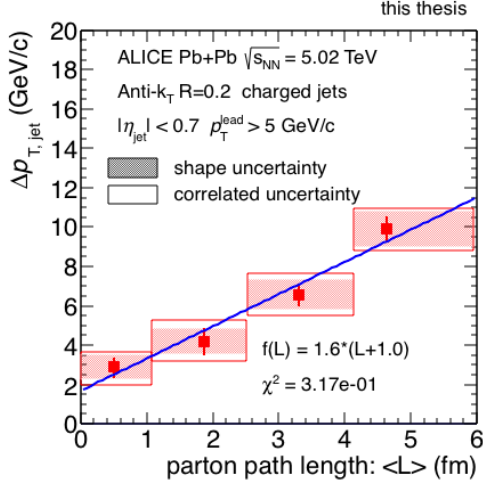


Fig 6.13: Average energy loss of charged jets as a function of estimated parton path length, with fitting result by linear function.

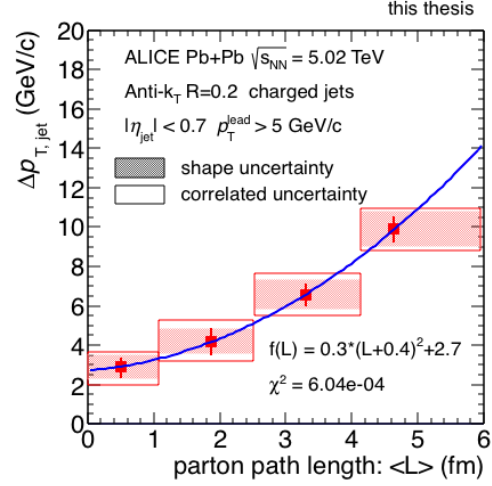


Fig 6.14: Average energy loss of charged jets as a function of estimated parton path length, with fitting result by quadratic function.

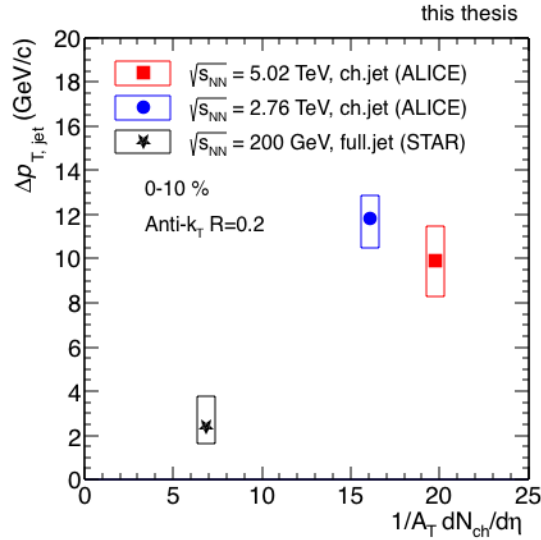


Fig 6.15: Average energy loss as a function of charged multiplicity per unit transverse area in 0-10% centrality class for three centre-of-mass energies.

Chapter 7 Summary

The work undertaken in this thesis aims at revealing the properties of a new state of QCD matter at extreme temperature and/or energy density, the Quark-Gluon Plasma, through the inclusive jet measurement. In the QGP, quarks and gluons become weakly coupled, deconfined from nucleons, due to the asymptotic freedom feature of QCD at high temperature. According to Lattice QCD calculation, a transition from normal nuclear matter to a QGP should occur when energy density exceeds a critical threshold of $\varepsilon_c \sim 0.18\text{-}0.5 \text{ GeV}/\text{fm}^3$ ($T_c = 154 \pm 9 \text{ MeV}$). Relativistic heavy-ion collisions, which produce extremely high temperatures and energy densities, are the unique tool to create QGP in the laboratory. Jets, defined as sprays of hadrons resulting from the fragmentation of high-energy partons, are one of the most powerful probes to study QGP properties. Such partons are indeed produced at very early stages of the collision and propagate through the medium losing energy via gluon radiation or multiple scattering. As such, their modification (yield, fragmentation, shape...) reflects the whole system evolution. This phenomenon, called jet quenching, is confirmed by several experimental observables measured both at RHIC and LHC.

The LHC (Large Hadron Collider) at CERN started operation from 2009 and since then, various collision systems and energies were provided. The ALICE, one of the four LHC experiments, is optimised for the study of QGP in heavy-ion collisions. During the two-year LHC long shutdown period (LS1) from 2013, the LHC accelerator was upgraded to achieve higher beam luminosity and energy. The ALICE experiment seized the opportunity of LS1 to upgrade some of its detectors to cope with the new beam conditions and keep improving QGP measurements.

During LS1, a new Electromagnetic calorimeter “DCAL” was installed in ALICE to enhance the acceptance for neutral particles and measure di-jet energy with charged and neutral particles. Along with this upgrade, a new online trigger system was deployed to efficiently select events containing high energy electromagnetic showers from jets or high- p_T photon. Taking advantage of back-to-back relation in azimuth between DCAL and EM-CAL, the new L1 trigger algorithm implements a median background estimation which makes the calorimeter triggers more self-consistent. The trigger calculation is carried out

by a FPGA mounted on the STU (Summary Trigger Unit) board. The new trigger algorithm performance was validated with the data taken in the first Pb-Pb run of the LHC Run2 period (after LS1).

Using the same Pb-Pb data, jet production was measured at highest-ever centre-of-mass energy of 5.02 TeV provided by the LHC. Jets are reconstructed from charged particles detected in the ALICE central tracking detectors, with jet resolution parameter of $R = 0.2$. One of the basic challenge for the jet measurement in heavy-ion collisions is to separate the jets from the soft underlying event. The average energy contribution from the soft underlying event is quantified on an event-by-event basis and subtracted from the reconstructed jet. The remaining underlying event fluctuations and detector effects are unfolded at an event-ensemble level. Additionally, a jet leading track transverse momentum cut-off of 5 GeV/ c is applied to reduce the fake jet contamination.

A strong suppression of jet production is observed in the most central Pb-Pb collisions and quantified by the measurement of the nuclear modification factor, R_{AA} . The observed suppression confirms the jet quenching picture established by earlier results. To gain further insight into the parton energy loss mechanism, in this work, the jet energy loss is studied using spectrum energy shift between AA and pp collisions. The following notable conclusions were drawn:

- The measured jet nuclear modification factor is well accounted for with a constant energy loss model in the considered momentum range (up to ~ 100 GeV/ c).
- The magnitude of energy loss at LHC energies is larger than at RHIC, which suggests that the nuclear collisions of larger centre-of-mass energy produce denser QGP.
- The energy loss as a function of the average parton path length has a quadratic behaviour which supports the idea that gluon radiation is the dominant source of parton energy loss in QGP.

To go one step further, a systematic study (as a function of centre-of-mass energy, resolution parameters, leading track p_T cut-off, charged+neutral jet measurement...) should be carried out. Complementary jet correlation studies (e.g. requiring an away side jet, high- p_T photon or high- p_T hadron...) would also help to control the parton path length. Especially, the jet/photon triggers developed in this thesis work will help a lot these latter analysis to collect the requested large statistics of jets and/or high- p_T photons.

Bibliography

- [1] R. Oerter, *The Theory of Almost Everything: The Standard Model, the Unsung Triumph of Modern Physics*. Penguin Group, 2006. 0-13-236678-9.
- [2] G. Altarelli, “Collider Physics within the Standard Model: a Primer,” [arXiv:1303.2842 \[hep-ph\]](#).
- [3] “Wikimedia commons.”. Standard model of elementary particles.
- [4] W. Greiner, E. Schramm, Stefan Stein, and D. d’Enteria et al., *Quantum Chromodynamics*. Springer-Verlag Berlin Heidelberg, 2007. 978-3-540-48534-6.
- [5] K. G. Wilson, “Confinement of Quarks,” *Phys. Rev.* **D10** (1974) 2445–2459.
- [6] D. J. Gross and F. Wilczek, “Ultraviolet Behavior of Nonabelian Gauge Theories,” *Phys. Rev. Lett.* **30** (1973) 1343–1346.
- [7] H. D. Politzer, “Reliable Perturbative Results for Strong Interactions?,” *Phys. Rev. Lett.* **30** (1973) 1346–1349.
- [8] Y. Kohsuke, H. Tetsuo, and Y. Miake, *Quark-Gluon Plasma: From Big Bang to Little Bang*. Cambridge University Press, 2008. 9780521089241.
- [9] F. Karsch, E. Laermann, and A. Peikert, “The Pressure in two flavor, (2+1)-flavor and three flavor QCD,” *Phys. Lett.* **B478** (2000) 447–455, [arXiv:hep-lat/0002003 \[hep-lat\]](#).
- [10] A. S. Kronfeld, “Twenty-first Century Lattice Gauge Theory: Results from the QCD Lagrangian,” *Ann. Rev. Nucl. Part. Sci.* **62** (2012) 265–284, [arXiv:1203.1204 \[hep-lat\]](#).
- [11] A. Bazavov *et al.*, “The chiral and deconfinement aspects of the QCD transition,” *Phys. Rev.* **D85** (2012) 054503, [arXiv:1111.1710 \[hep-lat\]](#).

- [12] “Particle data group.”. <http://pdg.lbl.gov/>.
- [13] V. Petousis, “Theoretical Review on QCD and Vector Mesons in Dileptonic Quark Gluon Plasma,” [arXiv:1208.4437](https://arxiv.org/abs/1208.4437) [hep-ph].
- [14] “Particles and friends.”. <https://particlesandfriends.wordpress.com/>.
- [15] “Cern courier.”. <http://cerncourier.com>.
- [16] J. P. Vary, “Multiple Collision Model for Pion Production in Relativistic Nucleus-Nucleus Collisions,” *Phys. Rev. Lett.* **40** (1978) 295–298.
- [17] M. L. Miller, K. Reygers, S. J. Sanders, and P. Steinberg, “Glauber modeling in high energy nuclear collisions,” *Ann. Rev. Nucl. Part. Sci.* **57** (2007) 205–243, [arXiv:nuc1-ex/0701025](https://arxiv.org/abs/nuc1-ex/0701025) [nucl-ex].
- [18] S. Sourav and S. SatzBikash, *The Physics of the Quark-Gluon Plasma*. Springer Berlin Heidelberg, 2010. 978-3-642-02285-2.
- [19] G. Altarelli and G. Parisi, “Asymptotic Freedom in Parton Language,” *Nucl. Phys.* **B126** (1977) 298–318.
- [20] H. Hahn *et al.*, “The RHIC design overview,” *Nucl. Instrum. Meth.* **A499** (2003) 245–263.
- [21] L. Evans and P. Bryant, “LHC Machine,” *JINST* **3** (2008) S08001.
- [22] E. Braaten and M. H. Thoma, “Energy loss of a heavy quark in the quark - gluon plasma,” *Phys. Rev.* **D44** no. 9, (1991) R2625.
- [23] A. Peshier, “The QCD collisional energy loss revised,” *Phys. Rev. Lett.* **97** (2006) 212301, [arXiv:hep-ph/0605294](https://arxiv.org/abs/hep-ph/0605294) [hep-ph].
- [24] S. Peigne and A. Peshier, “Collisional energy loss of a fast heavy quark in a quark-gluon plasma,” *Phys. Rev.* **D77** (2008) 114017, [arXiv:0802.4364](https://arxiv.org/abs/0802.4364) [hep-ph].
- [25] B. G. Zakharov, “Parton energy loss in an expanding quark-gluon plasma: Radiative versus collisional,” *JETP Lett.* **86** (2007) 444–450, [arXiv:0708.0816](https://arxiv.org/abs/0708.0816) [hep-ph].

- [26] B. G. Zakharov, “Parton energy loss in an expanding quark-gluon plasma: Radiative vs. collisional,” *JETP Letters* **86** no. 7, (Dec, 2007) 444–450.
- [27] P. Foka and M. A. Janik, “An overview of experimental results from ultra-relativistic heavy-ion collisions at the CERN LHC: Hard probes,” *Rev. Phys.* **1** (2016) 172–194, [arXiv:1702.07231 \[hep-ex\]](#).
- [28] **ALICE** Collaboration, J. Adam *et al.*, “Measurement of jet suppression in central Pb-Pb collisions at $\sqrt{s_{\text{NN}}} = 2.76$ TeV,” *Phys. Lett.* **B746** (2015) 1–14, [arXiv:1502.01689 \[nucl-ex\]](#).
- [29] **ALICE** Collaboration, J. Adam *et al.*, “Measurement of charged jet production cross sections and nuclear modification in p-Pb collisions at $\sqrt{s_{\text{NN}}} = 5.02$ TeV,” *Phys. Lett.* **B749** (2015) 68–81, [arXiv:1503.00681 \[nucl-ex\]](#).
- [30] C. Lefevre, “The CERN accelerator complex. Complexe des accelerateurs du CERN.” CERN-DI-0812015, Dec, 2008.
- [31] **ALICE** Collaboration, B. B. Abelev *et al.*, “Performance of the ALICE Experiment at the CERN LHC,” *Int. J. Mod. Phys.* **A29** (2014) 1430044, [arXiv:1402.4476 \[nucl-ex\]](#).
- [32] J. Jowett *et al.*, “The 2015 Heavy-Ion Run of the LHC,” in *Proc. of International Particle Accelerator Conference (IPAC’16), Busan, Korea, May 8-13, 2016*, no. 7 in International Particle Accelerator Conference, pp. 1493–1496. JACoW, June, 2016. doi:10.18429/JACoW-IPAC2016-TUPMW027.
- [33] “Alice collaboration.”. <https://alice-collaboration.web.cern.ch/>.
- [34] **ALICE** Collaboration, G. Dellacasa *et al.*, “ALICE technical design report of the zero degree calorimeter (ZDC),”. CERN-LHCC-99-05.
- [35] **ALICE** Collaboration, P. Cortese *et al.*, “ALICE technical design report on forward detectors: FMD, T0 and V0,”. CERN-LHCC-2004-025.
- [36] **ALICE** Collaboration, G. Dellacasa *et al.*, “ALICE technical design report of the inner tracking system (ITS),”. CERN-LHCC-99-12.

- [37] J. Alme *et al.*, “The ALICE TPC, a large 3-dimensional tracking device with fast readout for ultra-high multiplicity events,” *Nucl. Instrum. Meth.* **A622** (2010) 316–367, [arXiv:1001.1950](#) [[physics.ins-det](#)].
- [38] **ALICE** Collaboration, P. Cortese, “ALICE transition-radiation detector,” ALICE-TDR-9.
- [39] **ALICE** Collaboration, G. Dellacasa *et al.*, “ALICE technical design report of the time-of-flight system (TOF),”. CERN-LHCC-2000-012.
- [40] **ALICE** Collaboration, S. Beole *et al.*, “ALICE technical design report: Detector for high momentum PID,”. CERN-LHCC-98-19.
- [41] **ALICE** Collaboration, P. Cortese *et al.*, “ALICE electromagnetic calorimeter technical design report,”. CERN-LHCC-2008-014.
- [42] J. Allen *et al.*, “ALICE DCal: An Addendum to the EMCal Technical Design Report Di-Jet and Hadron-Jet correlation measurements in ALICE,”. CERN-LHCC-2010-011.
- [43] **ALICE** Collaboration, G. Dellacasa *et al.*, “ALICE technical design report of the photon spectrometer (PHOS),”. CERN-LHCC-99-04.
- [44] **ALICE** Collaboration, E. Abbas *et al.*, “Performance of the ALICE VZERO system,” *JINST* **8** (2013) P10016, [arXiv:1306.3130](#) [[nucl-ex](#)].
- [45] **ALICE** Collaboration, K. Aamodt *et al.*, “Alignment of the ALICE Inner Tracking System with cosmic-ray tracks,” *JINST* **5** (2010) P03003, [arXiv:1001.0502](#) [[physics.ins-det](#)].
- [46] X.-N. Wang and M. Gyulassy, “HIJING: A Monte Carlo model for multiple jet production in p p, p A and A A collisions,” *Phys. Rev.* **D44** (1991) 3501–3516.
- [47] T. Sjostrand, S. Mrenna, and P. Z. Skands, “PYTHIA 6.4 Physics and Manual,” *JHEP* **05** (2006) 026, [arXiv:hep-ph/0603175](#) [[hep-ph](#)].
- [48] T. Sjostrand, S. Ask, J. R. Christiansen, R. Corke, N. Desai, P. Ilten, S. Mrenna, S. Prestel, C. O. Rasmussen, and P. Z. Skands, “An Introduction to PYTHIA 8.2,” *Comput. Phys. Commun.* **191** (2015) 159–177, [arXiv:1410.3012](#) [[hep-ph](#)].

- [49] R. Brun, F. Bruyant, F. Carminati, S. Giani, M. Maire, A. McPherson, G. Patrick, and L. Urban, “GEANT Detector Description and Simulation Tool,”. CERN-W5013.
- [50] M. Cacciari, G. P. Salam, and G. Soyez, “The Anti-k(t) jet clustering algorithm,” *JHEP* **04** (2008) 063, arXiv:0802.1189 [hep-ph].
- [51] S. D. Ellis and D. E. Soper, “Successive combination jet algorithm for hadron collisions,” *Phys. Rev.* **D48** (1993) 3160–3166, arXiv:hep-ph/9305266 [hep-ph].
- [52] T. Auye, “Unfolding algorithms and tests using RooUnfold,” in *Proceedings, PHYSTAT 2011 Workshop on Statistical Issues Related to Discovery Claims in Search Experiments and Unfolding*, pp. 313–318. CERN, 2011. arXiv:1105.1160 [physics.data-an].
- [53] A. Hocker and V. Kartvelishvili, “SVD approach to data unfolding,” *Nucl. Instrum. Meth.* **A372** (1996) 469–481, arXiv:hep-ph/9509307 [hep-ph].
- [54] S. Alioli, K. Hamilton, P. Nason, C. Oleari, and E. Re, “Jet pair production in POWHEG,” *JHEP* **04** (2011) 081, arXiv:1012.3380 [hep-ph].
- [55] **ALICE** Collaboration, B. Abelev *et al.*, “Centrality Dependence of Charged Particle Production at Large Transverse Momentum in Pb–Pb Collisions at $\sqrt{s_{NN}} = 2.76$ TeV,” *Phys. Lett.* **B720** (2013) 52–62, arXiv:1208.2711 [hep-ex].
- [56] **ALICE** Collaboration, S. Acharya *et al.*, “Transverse momentum spectra and nuclear modification factors of charged particles in pp, p-Pb and Pb-Pb collisions at the LHC,” arXiv:1802.09145 [nucl-ex].
- [57] **ALICE** Collaboration, B. Abelev *et al.*, “Measurement of charged jet suppression in Pb-Pb collisions at $\sqrt{s_{NN}} = 2.76$ TeV,” *JHEP* **03** (2014) 013, arXiv:1311.0633 [nucl-ex].
- [58] **ATLAS** Collaboration, T. A. collaboration, “Study of inclusive jet yields in Pb+Pb collisions at $\sqrt{s_{NN}} = 5.02$ TeV,”.
- [59] J. Cleymans, “The Tsallis Distribution at the LHC,” *EPJ Web Conf.* **70** (2014) 00009, arXiv:1210.7464 [hep-ph].

- [60] **STAR** Collaboration, M. Ploskon, “Inclusive cross section and correlations of fully reconstructed jets in $\sqrt{s_{\text{NN}}} = 200$ GeV Au-Au and pp collisions,” *Nucl. Phys.* **A830** (2009) 255C–258C, [arXiv:0908.1799](#) [nucl-ex].
- [61] **ALICE** Collaboration, J. Adam *et al.*, “Centrality dependence of the charged-particle multiplicity density at midrapidity in Pb-Pb collisions at $\sqrt{s_{\text{NN}}} = 5.02$ TeV,” *Phys. Rev. Lett.* **116** no. 22, (2016) 222302, [arXiv:1512.06104](#) [nucl-ex].
- [62] **ALICE** Collaboration, K. Aamodt *et al.*, “Centrality dependence of the charged-particle multiplicity density at mid-rapidity in Pb-Pb collisions at $\sqrt{s_{\text{NN}}} = 2.76$ TeV,” *Phys. Rev. Lett.* **106** (2011) 032301, [arXiv:1012.1657](#) [nucl-ex].
- [63] **PHOBOS** Collaboration, B. B. Back *et al.*, “Centrality dependence of the charged particle multiplicity near mid-rapidity in Au + Au collisions at $\sqrt{s_{\text{NN}}} = 130$ GeV and 200 GeV,” *Phys. Rev.* **C65** (2002) 061901, [arXiv:nucl-ex/0201005](#) [nucl-ex].